Operando Characterisations of Lithium/Sodium Metal Batteries



Chen Gong

St Edmund Hall

Department of Materials

University of Oxford

A thesis submitted for the degree of

Doctor of Philosophy

Hilary 2023

Declaration of Originality

I, Chen Gong, hereby declare that this doctoral thesis, which is approximately 41,821 words in length, has been written by me and that it is the record of work carried out by me. This thesis has not been submitted in any previous application for a higher degree.

Chen Gong

Hilary

2023

Acknowledgments

First, I would like to thank Dr. Alex Robertson and Prof. Peter Bruce for their mentorship and for every scientific discussion we have had over the past four years. Working in such a world-leading group has been a great honor. Please allow me to express my thanks to all the group members for their help and company in the past four years. Thank Dr. Alex Robertson again for his warm help with my experiments and papers. Especially I will never forget the time when we did the in-situ liquid TEM experiments together in Oxford. In addition, I would like to thank Shengda Pu for being an excellent friend in science and for his help with my Li and Na projects. I would also like to thank Dr. Xiangwen Gao, Dr. Sixie Yang, Dr. Ziyang Ning, Dr. Junliang Liu, Dr. Paul Adamson, Dr. Jingyuan Liu, Dr. Boyang Liu, Dr. Jili Yue, Dr. Zhaoxin Yu, Dr. Sunyhik Ahn, Dr. Nadia Abdul-Karim, Dr. Robert House, Dr. Gareth Hartley, Dr. Gregory Rees, Dr. Isaac Capone, Dr. Xiaoyu Xu, Yi Yuan, Shengming Zhang, Liquan Pi, Bingkun Hu, Chloe Chau, Zixuan Li, and John- Joseph Marie for their helpful scientific advice on my road of research. Besides, I would like to thank my colleagues for their help and friendship during this work: Ceren Zor, Max Jenkins, Dominic Melvin, Varnika Agarwal, Dr. Dominic Spencer Jolly, Dr. Erez Cohen, Zsofia, Dr. Jitti Kasemchainan, Dr. James Summerville, Dr. Miguel Angel Perez, Dr. Edouard Boivin, Dr. Jun Chen, and Miki Bennett.

Secondly, I am highly appreciative of my college St Edmund Hall, for the generous graduate scholarship for funding part of my tuition fees. I also want to thank China Oxford Scholarship Funding (COSF) for funding part of my living cost in Oxford.

Finally, I sincerely thank my wife, parents, and brother. Without their unwavering love and sacrifices along the way, my achievements would have been impossible.

Abstract

This thesis explores the degradation mechanisms of lithium/sodium metal battery anodes by several operando characterization techniques, such as real-time liquid-cell scanning transmission electron microscopy, online mass spectrometry, and in-situ atomic force microscopy. These findings highlight the importance of appropriately designing electrolytes and tailoring the solid electrolyte interphase for achieving non-dendritic lithium/sodium deposition and dissolution.

In Chapter 4, the reason why fluoride-rich SEI benefits lithium metal anodes and how they alter the structural dynamics of lithium plating/stripping to promote efficiency were studied. The fluoride-rich SEI was directly observed to yield a flatter and finer deposited lithium structure that presented a better morphology for uniform stripping, thus resulting in a significant reduction in dead lithium. In addition, the dead lithium was quantificationally found to be the main degradation reason for lithium metal batteries, and the LiH was verified to be an important SEI component in lithium metal batteries.

In Chapter 5, the role of electrolyte solvents during sodium plating/stripping was systematically studied. Severe gas formation was observed in carbonate-based electrolytes during sodium plating/stripping while just a few bubbles in ether electrolytes. The SEI in ether electrolyte was found to be much stiffer and more elastic, and the plated sodium was more uniform. In addition, fewer dead sodium formations and less electrolyte decomposition were measured in the ether-based system compared to a carbonate-based electrolyte case.

Publication List

1. **Gong, C.**, Pu, S.D., Zhang, S., Yuan, Y., Ning, Z., Yang, S., Gao, X., Chau, C., Li, Z., Liu, J., et al. (2023). The role of an elastic interphase in suppressing gas evolution and promoting uniform electroplating in sodium metal anodes. Energy Environ. Sci. 16, 535–545. (Open Access)

2. **Gong, C.**, Pu, S.D., Gao, X., Yang, S., Liu, J., Ning, Z., Rees, G.J., Capone, I., Pi, L., Liu, B., et al. (2021). Revealing the Role of Fluoride-Rich Battery Electrode Interphases by Operando Transmission Electron Microscopy. Adv. Energy Mater. 11, 2003118. (Open Access)

3. **Gong, C.**, Pu, S., Robertson, A.W. (2021). In Situ Transmission Electron Microscopy for Studying Lithium-Ion Batteries. In: Gao, Yj., Song, W., Liu, J.L., Bashir, S. (eds) Advances in Sustainable Energy. Springer, Cham. https://doi.org/10.1007/978-3-030-74406-9_19.

4. Pu, S.D., **Gong, C.**, Tang, Y.T., Ning, Z., Liu, J., Zhang, S., Yuan, Y., Melvin, D., Yang, S., Pi, L., et al. (2022). Achieving Ultrahigh-Rate Planar and Dendrite-Free Zinc Electroplating for Aqueous Zinc Battery Anodes. Adv. Mater., 2202552. (**Co-first author**)

5. Pu, S.D., **Gong, C.**, Gao, X., Ning, Z., Yang, S., Marie, J.-J., Liu, B., House, R.A., Hartley, G.O., Luo, J., et al. (2020). Current-Density-Dependent Electroplating in Ca Electrolytes: From Globules to Dendrites. ACS Energy Lett. 5, 2283–2290. (**Co-first author**)

6. Zhang, Y., **Gong, C.**, Li, D., Wang, Z.W., Pu, S.D., Robertson, A.W., Yu, H., and Parrington, J. (2021). A prognostic dynamic model applicable to infectious diseases providing easily visualized guides: a case study of COVID-19 in the UK. Sci. Rep. 11, 1–12. (**Co-first author**)

7. Pu, S., **Gong, C.**, and Robertson, A.W. (2020). Liquid cell transmission electron microscopy and its applications. R. Soc. Open Sci. 7, 191204. (**Co-first author**)

8. Ning, Z., Li, G., Melvin, D.L.R., Chen, Y., Bu, J., Spencer-Jolly, D., Liu, J., Hu, B., Gao, X., Perera, J., **Gong, C.**, et al. (2023). Dendrite initiation and propagation in lithium metal solid-state batteries. Nature 618, 287–293.

9. Hua, X., Allan, P.K., **Gong, C.**, Chater, P.A., Schmidt, E.M., Geddes, H.S., Robertson, A.W., Bruce, P.G., and Goodwin, A.L. (2021). Non-equilibrium metal oxides via reconversion chemistry in lithium-ion batteries. Nat. Commun. 12, 561.

10. Ning, Z., Jolly, D.S., Li, G., De Meyere, R., Pu, S.D., Chen, Y., Kasemchainan, J., Ihli, J., **Gong, C.**, Liu, B., et al. (2021). Visualizing plating-induced cracking in lithium-anode solid-electrolyte cells. Nat. Mater. 20, 1121–1129.

11. Xu, X., Pi, L., Marie, J.-J., Rees, G.J., **Gong, C.**, Pu, S., House, R.A., Robertson, A.W., and Bruce, P.G. (2021). Li_2 NiO_2F a New Oxyfluoride Disordered Rocksalt Cathode Material. J. Electrochem. Soc. 168, 080521.

12. Liu, J., Gao, X., Hartley, G.O., Rees, G.J., **Gong, C.**, Richter, F.H., Janek, J., Xia, Y., Robertson, A.W., Johnson, L.R., et al. (2020). The Interface between Li6.5La3Zr1.5Ta0.5O12 and Liquid Electrolyte. Joule 4, 101–108.

List of Abbreviations

LIBs	- Lithium-ion Batteries
LMB	- Li Metal Battery
TEM	- Transmission Electron Microscopy
DEMS	- Differential Electrochemical Mass Spectrometry
AFM	- Atomic Force Microscopy
CV	- Cyclic Voltammetry
DMC	- Dimethyl Carbonate
EC	- Ethylene Carbonate
$LiPF_6$	- Lithium Hexafluorophosphate
SEI	- Solid Electrolyte Interphase
CEI	- Cathode Electrolyte Interphase
DME	- 1,2-Dimethoxyethane
LP30	- 1M $LiPF_6$ in EC: DMC (v:v) = 1:1
NP30	- 1M $NaPF_6$ in EC: DMC (v:v) = 1:1
CE	- Coulombic Efficiency
PC	- Propylene Carbonate
FEC	- Fluoroethylene Carbonate
VC	- Vinylene Carbonate
HOMO	- Highest Occupied Molecular Orbital
LOMO	- Lowest Occupied Molecular Orbital
kMC	- Kinetic Monte Carlo
LEDC	- Lithium Ethylene Dicarbonate
LEMC	- lithium Ethylene Monocarbonate
SIMS	- Secondary Ion Mass Spectrometry
SEM	- Scanning Electron Microscopy

NMR	- Nuclear Magnetic Resonance
MOF	- Metal-organic Framework
PAN	- Polyacrylonitrile
SSEs	- Solid-state Electrolytes
XPS	- X-ray Photoelectron Spectroscopy
AEM	- Analytical Electron Microscopy
STEM	- Scanning Transmission Electron Microscopy
LC-STEM	- Liquid Cell STEM
EELS	- Electron Energy Loss Spectra
EDS	- Energy-dispersive X-ray Spectroscopy

Table of Contents

Declaration of Originality ..... **ii**

Acknowledgments ..... **iii**

Abstract ..... **iv**

Publication List ..... **v**

List of Abbreviations ..... **vii**

Chapter 1. Introduction to Batteries **1**

1.1 Background **1**

1.2 Introduction of lithium metal batteries **3**

1.2.1 Lithium-ion batteries ***3***

1.2.2 Lithium metal batteries ***7***

1.3 Challenges for lithium metal batteries **9**

1.3.1 SEI formation on lithium metal anode ***9***

1.3.2 Dendrite growth on Li metal anode ***12***

1.3.3 Gas formation at the interface ***18***

1.4 Introduction and challenges of sodium metal batteries **19**

1.4.1 Sodium metal batteries ***19***

1.4.2 Challenges of sodium metal batteries ***21***

1.5 Aim of this work **24**

Chapter 2. In-situ Liquid TEM **26**

2.1 Introduction of in-situ liquid TEM **26**

2.1.1 The open-cell in-situ TEM ***27***

2.1.2 The closed-cell in-situ TEM ***28***

2.1.3 Discussion of the two kinds of in-situ TEM cells ***31***

2.2 Application of in-situ liquid TEM **32**

2.2.1 Degradation process at the electrode interface *32*

2.2.2 Electrode changes during lithiation/delithiation *35*

2.3 Beam effects of in-situ liquid TEM **36**

2.4 Summary of in-situ liquid TEM application in LIBs **37**

Chapter 3. Experimental Techniques **39**

3.1 Sample preparation **39**

3.2 Electrochemical methods **40**

3.2.1 Cyclic voltammetry (CV) *40*

3.2.2 Galvanostatic cycling *41*

3.2.3 Electrochemical impedance spectroscopy *42*

3.3 Characterization techniques **44**

3.3.1 Scanning electron microscopy (SEM) *44*

3.3.2 Focused ion beam (FIB) *46*

3.3.3 Secondary ion mass spectrometer (SIMS) *47*

3.3.4 Differential Electrochemical Mass Spectrometry (DEMS) *48*

3.3.5 Nuclear Magnetic Resonance (NMR) *51*

3.3.6 Atomic force microscopy (AFM) *52*

3.3.7 Transmission electron microscopy (TEM) *54*

3.3.8 Scanning transmission electron microscopy (STEM) *58*

3.3.9 In-situ sealed liquid S/TEM *59*

Chapter 4. Revealing the role of fluoride-rich battery electrode interphases by Operando Transmission Electron Microscopy **65**

4.1 Introduction **65**

4.2 Results **66**

4.2.1 In-situ liquid STEM characterization *66*

4.2.2 SEI chemical composition analysis by SIMS and NMR *80*

4.2.3 Online-MS analysis *83*

4.2.4 Electrochemical impedance spectroscopy (EIS) analysis *86*

4.3 Discussion **87**

4.3.1 The effects of fluoride-rich interphase *87*

4.3.2 The impacts of bubble on the electroplating and stripping of lithium on LC-STEM experiments *88*

4.4 Conclusion **92**

Chapter 5. Operando Study of the Role of Electrolyte Solvents for Sodium Metal Battery **94**

5.1 Introduction **94**

5.2 Results **95**

5.2.1 Electrochemical performance analysis *95*

5.2.2 Operando liquid TEM characterization *103*

5.2.3 Post-mortem SEM characterization *106*

5.2.4 Operando liquid STEM characterization *109*

5.2.5 Ex-situ AFM characterization *113*

5.2.6 In-situ AFM characterization *119*

5.2.7 DEMS analysis *123*

5.2.8 Coin cell studies with other anode and cathode materials *125*

5.3 Discussion **129**

5.4 Conclusion **131**

Chapter 6. Conclusions and Future Work **133**

6.1. Conclusions **133**

6.2. Future work **135**

Chapter 7. References **138**

Chapter 1. Introduction to Batteries

1.1 Background

With the development of human society, economy and technology, more and more energy is required and consumed. Large-scale use of non-renewable energy, such as oil and coal, brings convenience but also induces the greenhouse effect and pollution. Therefore, most countries have embraced the Paris climate agreement, and sustainability has become the mainstream social consensus. Renewable energy resources are required to control carbon emissions, and corresponding clean energy storage systems are also needed. Energy storage systems are widely used to realize the stable operation of electric power supply. The specific application scenarios include: (1) improving the stability and reliability of power grid operation, reducing the impact of significant instantaneous changes of new power generation systems on the power grid, and decreasing photovoltaic and wind electricity waste, (2) applying to electric tools, such as vehicles and consumer electronics. The requirement for high energy density and long cycling performance makes lithium-based batteries become the most attractive choice for the latter type of applications. Lithium presents low electrochemical potential (− 3.04 V versus standard hydrogen electrode) and has a small atomic radius to be the ideal charge carrier.

The study of Li-based batteries starts with lithium metal batteries (LMBs). It has a history going back to 1913 when lithium electrodes in LMBs were studied by Lewis and Keyes.[1] In the 1970s, LMBs aroused great interest because of the oil crisis. Most of the work focused on solving the battery systems problems, such as looking for suitable electrolytes and cathodes, but the battery system was still unstable.[2–5] Whittingham proposed using a material with a layered crystal structure as the lithium battery cathode, such as TiS_2, because

the intercalation mechanism for lithium ions during cycling can effectively protect the cathode crystal structure and guarantee long-life cycling.[6–8] However, TiS_2 only has a limited voltage range (about 2V *vs.* Li/Li^+), and it is easy to release H_2S gas by reaction with the trace of water in the electrolyte; these are significant application concerns for LMBs. John Goodenough's team studied a series of transition metal oxide cathodes with a formula $LiXO_2$ (where X= Co, Mn, and Fe) in Oxford in the 1980s.[9,10] The $LiCoO_2$ (LCO) intercalation cathode has a high potential (above 4V *vs.* Li/Li^+), so the capacity density is significantly increased. In addition, there is already a lithium source in the $LiCoO_2$ cathode itself, so no extra lithium is required on the anode side. Therefore, the $LiCoO_2$ cathode promoted the discovery of an anode without an intrinsic lithium source, which considerably improves battery safety. During the searching for an anode, a carbon-based anode such as graphite seemed the most suitable choice,[11,12] due to the highly stable lithiation/delithiation reactions and low lithiation voltage. Akira Yoshino assembled a battery using soft carbon as an anode and LCO as a cathode, which is believed to be the foundation of the modern lithium-ion battery (LIB).[13] Based on this progress, Sony commercialized their first lithium-ion batteries (LIBs) in 1991.[14] Then, the LIBs were widely used in portable electronic devices and transportation, becoming the most critical part in the energy storage field with their excellent cycling performance.

Over the thirty years of research and application for LIBs, people have always pursued higher energy density, longer cycling life, and better safety. For example, attempting improvement of the anode and cathode materials. The metallic lithium anode, with its high theoretical capacity (3,860 mAh g^{-1}) and low electrochemical potential (− 3.04 V versus standard hydrogen electrode), has aroused more and more interest recently.[15,16] However, many challenges are still not solved, and some degradation mechanisms are unclear. Therefore, some background introduction to alkali metal anode batteries and a recent study

of their degradation mechanisms will be introduced in this chapter below. In this thesis, I will focus on studying failure mechanisms for lithium/sodium metal batteries by cutting-edge operando techniques such as in-situ transmission electron microscopy (TEM), differential electrochemical mass spectrometry (DEMS), and in-situ atomic force microscopy (AFM).

1.2 Introduction of lithium metal batteries

1.2.1 Lithium-ion batteries

LIBs are rechargeable batteries mainly composed of an anode, cathode, separator, and electrolyte (as shown in Figure 1.1). In a standard LIB, cathode materials are usually lithium-containing transition metal oxides, such as $LiCoO_2$ and $LiFePO_4$, and the anode is made of graphite. The electrolyte is traditionally made by a mixture of lithium salts and organic solvents, such as the common electrolyte LP30 (1M $LiPF_6$ in ethylene carbonate (EC) and dimethyl carbonate (DMC), EC: DMC = 1:1).

In the LIB discharging process, lithium ions (Li^+) come out from the anode and go into the electrolyte, releasing electrons into the circuit. Meanwhile, the cathode material gets lithium ions from the electrolyte and the same number of electrons from the external circuit to form a new stable crystal structure. Hence, for the electrolyte, the quantity of lithium ions keeps constant. In the charging process, the chemical reaction inside the battery is reversed, with electrons now released from the cathode. It is clear that electrons are only transported in the external circuit, and lithium ions are only transported inside the cell during the whole reversible process. Therefore, the LIB is also called a “rocking-chair” cell, and this operating mechanism has improved battery safety.[17] For example, the detailed discharge reaction is like below:

Anode side: $Li_xC_6(s) \rightarrow 6C(s) + xLi^+ + xe^-$ (1.1)

Cathode side: $Li_{1-x}CoO_2(s) + xLi^+ + xe^- \rightarrow LiCoO_2(s)$ (1.2)

Overall reaction: $Li_xC_6(s) + Li_{1-x}CoO_2(s) \rightarrow 6C(s) + LiCoO_2(s)$ (1.3)

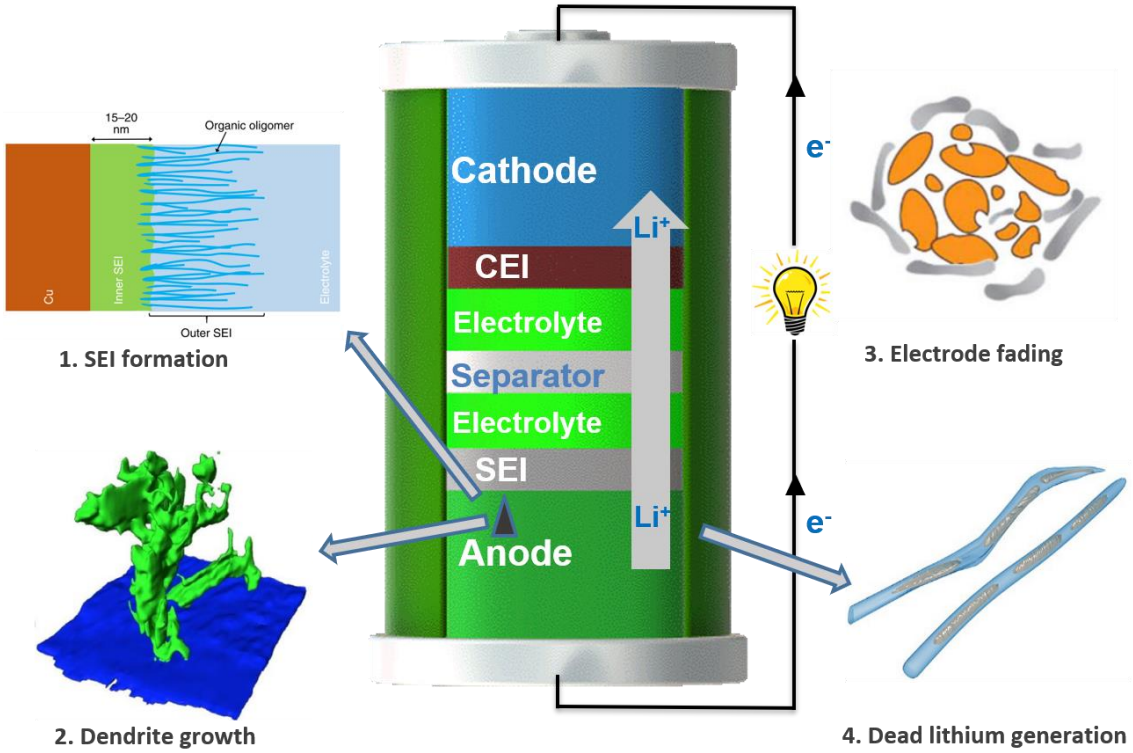


Figure 1.1. Schematic illustration of a lithium-ion battery and related failure process during cycling. The side reactions include but are not limited to solid electrolyte interphase (SEI) formation (Reprinted by permission from Springer Nature[18], copyright 2020), dendrite growth (Reprinted by permission from Springer Nature[19], copyright 2018), electrode fading (Reprinted by permission from Springer Nature[20], copyright 2017), and dead lithium generation (Reprinted by permission from Springer Nature[21], copyright 2019).

However, side reactions are inevitable, especially interphases growing at the interface. Usually, inside a LIB, the interphase is named the solid electrolyte interphase (SEI) on the anode side and the cathode electrolyte interphase (CEI) on the cathode side. The interphases are formed by electrolyte decomposition and side reactions with lithium, so the lithium source is consumed, and coulombic efficiency (CE) is decreased by this process.[22] In

addition, side reactions include electrolyte decomposition, dendrite growth, electrode fading, and dead lithium generation (as shown in Figure 1.1). All these side reactions can lead the battery cell failure. More degradation details will be discussed below.

Assembling a good-performance LIB is systematic work. High energy capacity, long-life cycling, high-rate capability, and safety are the improvement direction for battery commercialization. Exploring better battery materials and preventing side reactions are two effective methods. For the anode side, carbon plays the dominant role in existing batteries. Researchers found two types of carbon: graphitized and disordered carbon.[23,24] Graphitized carbons have organized layers, which can keep them stable during lithium intercalation/deintercalation. Based on whether graphitization occurs easily upon high temperature (3000 °C), the disordered carbon is divided into soft carbon (easy graphitization) and hard carbon (hard graphitization).[25] Through applying soft carbon (reversible capacity is about 200 mAh g^{-1}) as the anode, the most critical battery problem - safety, is greatly improved by the first-generation LIBs developed by Yoshino et al. and Sony in the early 1990s.[26] Before this, the lithium battery quickly caught fire and risked causing an explosion, hindering lithium batteries' application. However, soft carbon has exfoliation problems (like graphite) in propylene carbonate (PC) based electrolytes, inducing unstable cycling.[27,28] Hard carbon was then developed because it has better capacity than soft carbon and showed superior stability, even at high voltage (4.2V).[29,30] Then, hard carbon became the mainstream anode choice in the mid-1990s for the second generation LIBs and energy capacity was improved from 80 Wh kg^{-1} to 120 Wh kg^{-1}.[31] However, the first cycle of hard carbon has a large irreversible capacity which consumes many lithium ions from the cathode.[29] Thanks to the development of the EC solvent of LIBs electrolyte, graphite is back on the map as a viable anode. A protective SEI is formed during cycling when using a mixture of EC and PC electrolytes for graphite anode LIBs, and

exfoliation problems are effectively prevented.[32,33] As approaches to better electrolyte systems were developed, including employing fluoroethylene carbonate (FEC) and vinylene carbonate (VC) additives, the SEI over the anode surface became more stable, and side reactions were well controlled.[34,35] Thus, graphite has played a dominant role in the LIB anode market until now due to its high capacity (theoretical maximum of 372 mAh g^{-1}) and satisfying cycling performance.[26,36] This further suggests LIBs are a comprehensive electrochemical system, and overall performance improvement depends on each component's progress. LiC_6 was reported as the final crystalline phase after lithiation for graphite,[37] so the capacity is calculated roughly below:

$$Q_{graphite} = \frac{charge}{mass} = \frac{6.02214076 \times 10^{23} \times (1.602176634 \times 10^{-19}\ C) \times \frac{1mAh}{3.6C}}{6mol \times \frac{12.011g}{mol}}$$

$$= 372\ mAh\ g^{-1} \qquad (1.4)$$

In pursuit of the higher energy density of anode materials, group-IV elements-based anode materials have also been explored. For example, the silicon (Si) capacity reaches 3579 mAh g^{-1} and seems a promising anode candidate for the next generation of LIBs.[38] If we suppose $Li_{15}Si_4$ was the only final crystalline phase after lithiation,[39] the capacity is calculated roughly below:

$$Q_{silicon} = \frac{charge}{mass} = \frac{15 \times 6.02214076 \times 10^{23} \times (1.602176634 \times 10^{-19}\ C) \times \frac{1mAh}{3.6C}}{4mol \times \frac{28.0855g}{mol}}$$

$$= 3579 \text{ mAh g}^{-1} \quad (1.5)$$

However, the high-volume expansion during lithiation (around 300%) hinders its further application, which induces severe silicon anode cracking and poor capacity retention in the following cycles.[40,41] In addition, the continued growth of SEI at the newly exposed silicon surface causes uncontrolled electrolyte depletion, which further exacerbates the degradation of batteries.[42]

It seems that the quest for the ideal LIB anode material is persistent and never ends.

1.2.2 Lithium metal batteries

Lithium is the lightest metal with the smallest atomic radius in the whole alkali metal group. Together with extremely low electrochemical potential (− 3.04 V versus standard hydrogen electrode), making it seems like the best choice for anode material. The theoretical capacity reaches at least 3,860 mAh $g^{-1,}$ and the calculation method is presented below:[43]

$$Q_{Li} = \frac{\text{charge}}{\text{mass}} = \frac{6.02214076 \times 10^{23} \times (1.602176634 \times 10^{-19}\ \text{C}) \times \frac{1\text{mAh}}{3.6\text{C}}}{1\text{mol} \times \frac{6.94\text{g}}{\text{mol}}}$$

$$= 3862 \text{ mAh g}^{-1} \quad (1.6)$$

As you can see, the capacity calculated method of lithium metal is a little different from a regular anode material (such as graphite and silicon). Regular anode materials do not calculate the intercalation of lithium mass in an anode. If adding the lithium mass, the whole

silicon anode capacity should be:

$$Q_{Si+Li}=\frac{charge}{mass}=\frac{15\times6.02214076\times10^{23}\times(1.602176634\times10^{-19}\ C)\times\frac{1mAh}{3.6C}}{4mol\times\frac{28.0855g}{mol}+15mol\times\frac{6.94g}{mol}}$$

$$=1857\ mAh\ g^{-1} \qquad (1.7)$$

The gravimetric capacity density of the lithium metal anode is approximately two times that of the silicon anode. Thus, the lithium metal anode is considered the "Holy Grail" electrode and has aroused tremendous research interest.[44,45] However, this ideal capacity of lithium metal anode (around 3,860 mAh g^{-1}) which is calculated in Equation 1.6 is specific for the anode-free battery because it does not calculate the mass of the anode itself. In a real lithium metal battery, a lithium metal foil is usually the anode. When calculating the lithium metal anode capacity, the mass of the lithium metal foil should be considered. Therefore, the whole anode capacity will be discounted. The detailed capacity is related to the utilization rate of the lithium metal because the lithium source can also be supplied by cathode materials. In an ideal case, people wish to decrease the thickness of the lithium metal anode foil to improve the anode capacity in a lithium metal battery. However, if the lithium metal anode foil is thin enough, the active lithium consumption is fast and the expansion ratio of the anode is increased. Both of these factors can affect the cycling life of lithium metal batteries. Therefore, the amount of lithium metal anode in a lithium metal battery needs to be balanced and the corresponding capacity of lithium metal anode should be calculated in specific situations.

1.3 Challenges for lithium metal batteries

The degradation mechanisms must be clarified to employ the lithium anode in a genuine battery. The significant challenges include (1) uncontrolled SEI formation and corresponding electrolyte depletion, (2) dendrite growth, and (3) bubble formation. All these problems could seriously hinder its commercialization.[43,46]

1.3.1 SEI formation on lithium metal anode

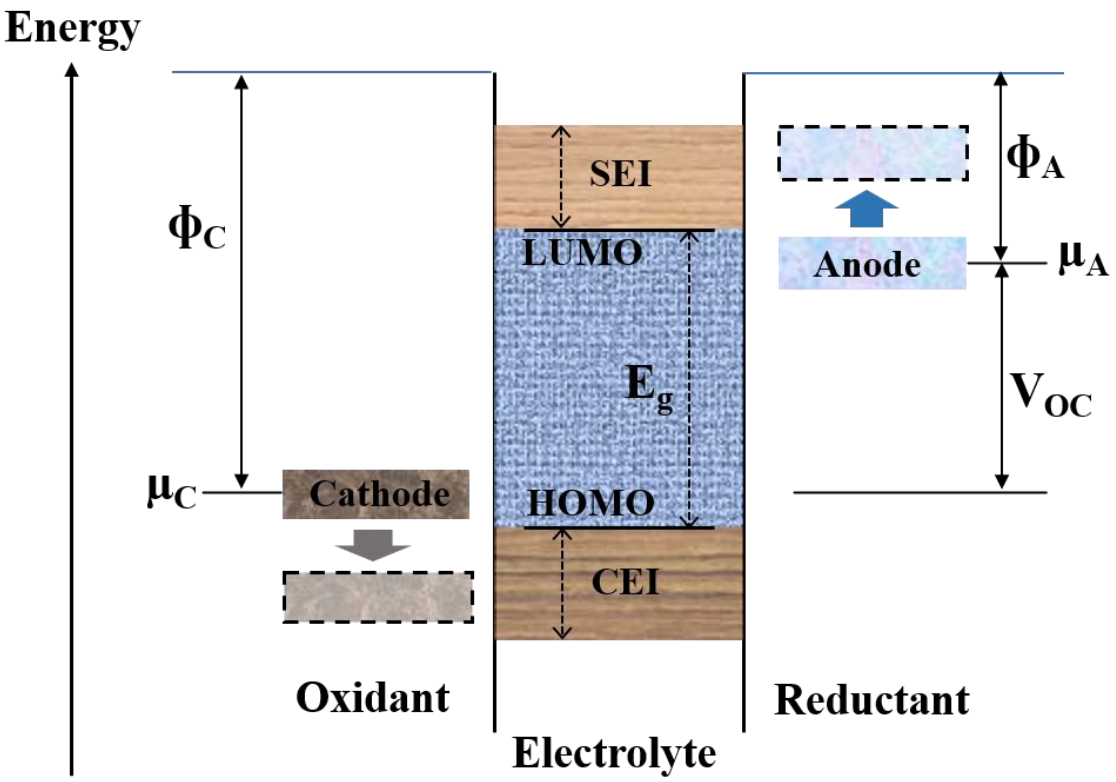


Figure 1.2. Schematic of an SEI formation principle in a liquid electrolyte battery. E_g is an electrolyte thermodynamic stability window. The Φ_A and Φ_C are the work functions of the anode and cathode, respectively. There will be SEI formation once μ_A > LUMO or CEI formation once μ_C < HOMO.

Peled coined the name "SEI", which describes the interphase formed at the interface between anode and electrolyte.[47] Due to a highly negative electrochemical voltage of lithium metal, the SEI can be generated on the lithium metal interface once exposed to the

organic electrolyte in batteries.[48] With voltage going down during lithium plating, the organic electrolyte further reacts with lithium, forming more SEI on the lithium metal anode. The SEI plays the role of passivation layer for lithium metal, which acts to prevent electrolytes from undergoing continual decomposition. Goodenough describes this SEI formation principle with a molecular orbital theory in a thermodynamic stability battery (as shown in Figure 1.2).[49]

The thermodynamic stability window of electrolytes (E_g) ranges between the lowest unoccupied molecular orbital (LUMO) and the highest occupied molecular orbital (HOMO). In this battery cell, the anode is the reductant and the cathode is the oxidant. The Φ_A and Φ_C are the work functions of the anode and cathode, respectively. The μ_A and μ_C are electrochemical potentials for anode and cathode (Fermi energies), respectively. If the μ_A of the anode is above the LUMO, the electrolyte will be reduced, forming a passivation layer (the SEI) to prevent further reaction. Similarly, if the μ_C of the cathode is below the HOMO, the electrolyte will be oxidized and form CEI to prevent electrons transferring from the electrolyte HOMO to the cathode. Therefore, the ideal SEI or CEI, once formed, is expected to protect the electrodes and stop electrolyte decomposition in the following cycles.

However, the SEI is usually unstable because of its complex structure and poor mechanical property. A mosaic-type SEI model was proposed by Peled et al. in 1997 based on studying SEI components on the carbon anode and the lithium metal anode.[50] The model illustrates that the SEI comprises a series of inorganic and organic materials, and the inorganic components are closer to the metal anode (Figure 1.3a). The whole structure decides the SEI impedance, and grain boundaries formed by different parts also contribute significantly to lithium-ion diffusion during cycling. Following the mosaic SEI model, Aurbach et al.

proposed a multilayer SEI model according to the sequential decomposition of electrolytes at the start of plating (Figure 1.3b).[51] As the molecular orbital theory shows in Figure 1.2, the reaction would be blocked once the SEI formed. So, the SEI formation is a step-by-step process, and the subsequent reaction has a higher selectivity once a layer of SEI is formed.

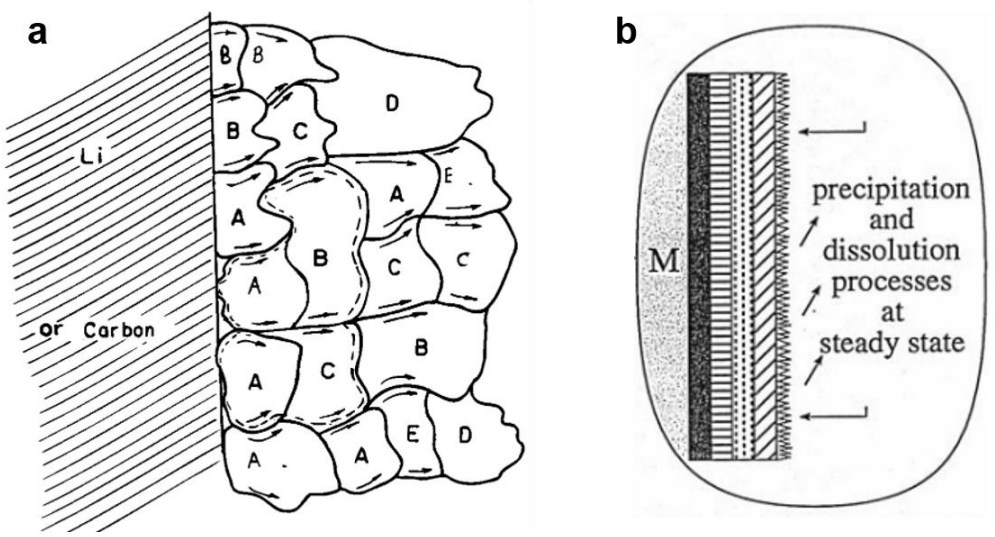


Figure 1.3. Schematic of the SEI structure model. (a) The Mosaic SEI model was proposed by Peled et al. in 1997. Reprinted with permission from the Electrochemical Society[50], copyright 1997. (b) The Multilayer SEI model was proposed by Aurbach et al. in 1999. Reprinted with permission from Elsevier,[51] copyright 1999.

By performing the first-principles kinetic Monte Carlo (kMC) simulations to explore SEI formation evolution in the electrochemical environment, it was found that EC was reduced first (roughly +0.7 V vs Li/Li^+) and formed inorganic carbonate species (most directly $LiCO_3^-$).[52] In the place close to the anode, the $LiCO_3^-$ prefers to coordinate with Li^+ and form inorganic Li_2CO_3. In a place far from the anode, the $LiCO_3^-$ usually reacts with Li^+EC to form the organic species lithium ethylene dicarbonate (LEDC). After this initial film has formed, the SEI continues growing with potential decreasing over time. A rapid two-electron reduction of EC happens and forms $Li^+OCH_2CH_2O_2^-$ and CO. The $Li^+OCH_2CH_2O_2^-$ can react with one CO_2 to form the organic species dilithium ethylene

monocarbonate (DLEMC). At the same time, the organic lithium ethylene monocarbonate (LEMC) could be formed by hydrolysis of Li^+EC, or nucleophilic addition of OH^- and MeO^- to EC.[53] However, both the LEDC and LEMC are unstable. The LEDC could decompose to form inorganic carbonates and release C_2H_4 at a low applied potential. Some of the LEMC could form DLEMC and H_2 through reductive decomposition. This SEI evolution process could finally result in the inorganic species dominant inner SEI (like Li_2CO_3) and organic species dominant outer SEI (like LEMC and DLEMC).[52] By using advanced characterization tools such as TEM[19,21,54] and secondary ion mass spectrometry (SIMS)[18], the anode SEI structure has concluded that consists of two layers. The inner layer is dense and compact and mainly composed of Li_2CO_3, LiF, and Li_2O.[21] The outer layer is permeable to liquid electrolytes and consists primarily of semi-carbonates and polymers.[55]

In conclusion, the SEI is a double-edged sword. On the one hand, the formation of SEI consumes lithium and electrolyte, causing irreversible loss of capacity. On the other hand, the SEI plays a critical role in passivating the anode and prevents further decomposition of the electrolyte. In addition, the SEI is also an important bridge to connect between anode and electrolyte, helping lithium ions pass through and blocking the electrons. Thus, the ideal SEI should have the following conditions: (1) high ionic conductivity while keeping poor electrical conductivity; (2) proper thickness, that is enough to passivate the anode but cannot hinder the lithium ions' diffusion; (3) suitable elastic mechanical property to adopt the significant volume expansion of the lithium anode; (4) proper stiffness, to make sure the SEI cannot be broken during cycling; (5) uniform distribution, leading the lithium uniform deposition on the anode.

1.3.2 Dendrite growth on Li metal anode

Lithium dendrites are a general term for irregular lithium deposits, which have been directly

seen in 1980.[56] Under certain dynamic conditions, the growth rate of lithium deposits tip is faster than that of the body, inducing a one-dimensional fibrous structure. Generally, there are three kinds of dendrite patterns: needlelike, mosslike, and treelike (Figure 1.4). Needle-like dendrites mainly grow in a length direction without branches, which could penetrate the separator and cause LMBs to short-circuit (Figure 1.4a). Mossy dendrites have smaller diameters with high surface area, consuming much more lithium to form SEI layers during lithium plating and quickly forming dead lithium due to fracture during lithium stripping (Figure 1.4b).[57] Treelike dendrites are classic and grow in all directions with evident branches like trees (Figure 1.4c).[58] The growth of dendrites can bring several adverse effects for batteries: (1) consuming lithium sources and leading to capacity loss; (2) breaking SEI and causing more side reactions; (3) forming dead lithium and increasing large polarization; (4) giving rise to battery safety issues such as short-circuiting.[43] Thus, it is essential to study the dendrite formation mechanisms and how to prevent dendrite growth.

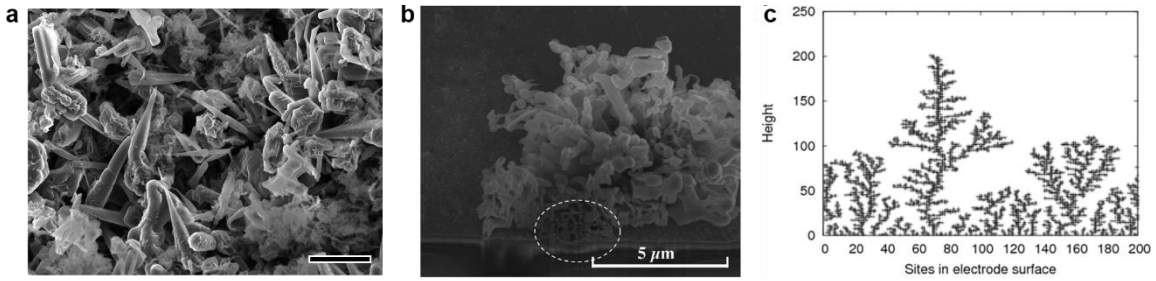


Figure 1.4. Schematic of three kinds of Li dendrites. (a) Needle-like dendrites, scale bar is 10 μm. (b) mossy-like dendrites, Reprinted with permission from Elsevier[57], copyright 2014. (c) tree-like dendrites. Reprinted by permission from Springer Nature[58], copyright 2015.

1.3.2.1 Lithium dendrites formation mechanisms

The lithium plating process is an electroplating behavior; inhomogeneities may lead to non-uniform deposition and generation of lithium dendrites. For example, the defects of substrates, second-phase impurities, and grain boundaries in the vicinity of SEI and lithium electrodes can all result in lithium dendrite nucleation.[59] In addition, the lithium ion

concentration near the anode is uneven due to inhomogeneous SEI or fast consumption of lithium ions in a dilute electrolyte.[60] The "Sand time" was widely recognized to measure the dendrite formation time in dilute electrolytes, which was first proposed by Henry J. S. Sand when studying the electroplating of copper.[61] During the lithium plating process in a dilute solution, lithium ions are consumed near the anode and continually diffuse from cathode to anode. If the current density is high enough, the speed of lithium ions diffusion is lower than the lithium ions being consumed. Eventually, the lithium-ion concentration near the anode reaches zero at a specific time. Then the electrodeposition is not uniform and becomes unstable.[62] This specific time is Sand's time τ_{sand} and the formula is shown below.

$$\tau_{sand} = \pi D \left(\frac{C_0 e z_c}{2J}\right)^2 \left(\frac{\mu_a + \mu_c}{\mu_a}\right)^2$$

With D is the ambipolar diffusion coefficient, C_0 is the cation (lithium salt) concentration of electrolyte, e is the electronic charge, z_c is the charge number of cation, J is the current density, μ_c and μ_a are cationic and anionic mobilities. From the formula, we can learn that the τ_{sand} is in direct proportion to ${C_0}^2$ and J^{-2}, the higher lithium salt concentration and lower current density could effectively prevent lithium dendrite formation. Several pieces of research further verify this deduction.[63–65] By visualizing lithium growth in a capillary cell (Figure 1.5a), Martin Z. Bazant et al. revealed that the mossy lithium grew first by a root-growth mechanism in a regular LP30 electrolyte system.[63] At this stage, the lithium salt near the electrode was enough for a reaction but decreased gradually (Figure 1.5b). When the lithium salt was depleted, a fractal structure grew from the tips (Figure 1.5 c-g). These two stages implied two different lithium growth mechanisms, from reaction-limited to diffusion-limited, consistent with the Sand's time theory. The diffusion-limited model is

a popular model for understanding lithium dendrite formation in liquid electrolytes nowadays.

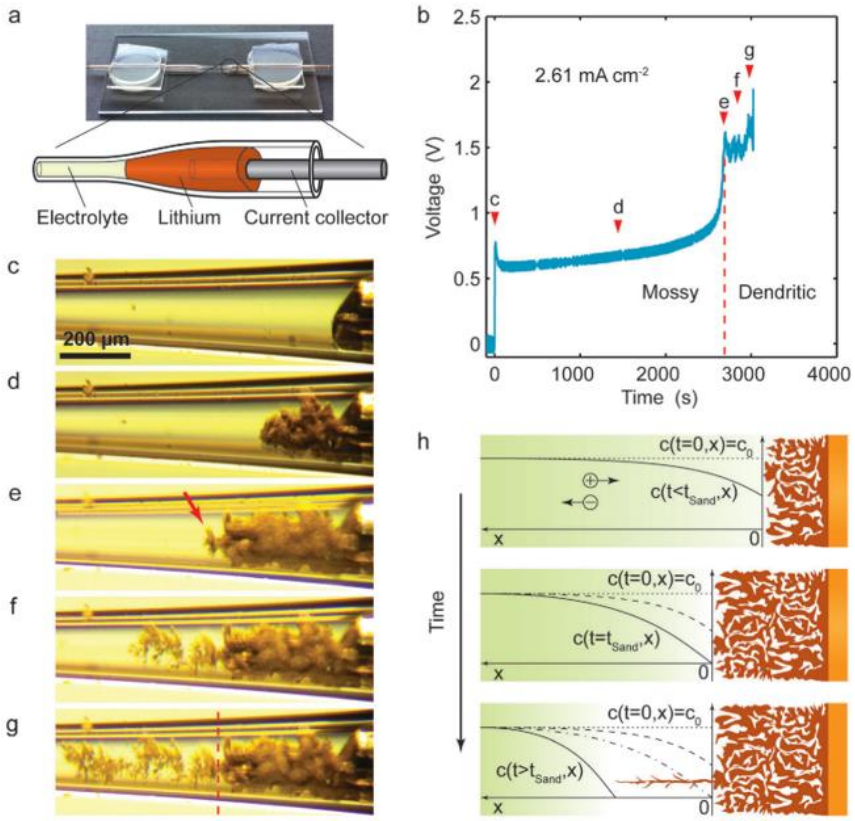


Figure 1.5. In situ observations of the lithium plating process in a capillary filled with LP30 electrolyte by optical microscope. (a) Schematic of the capillary cell. (b) Deposition of Li at a constant current density of 2.61 mA cm^{-2}. The voltage changes are shown simultaneously, and the voltage increase implies the electrolyte was being consumed. (c–g) The recorded dynamic process figures during Li plating. The red arrow in (e) illustrates the formation of fractal Li. The red dash line in (g) represents the two different plating mechanism stages. (h) The theoretical illustration of the lithium plating process in the electrolyte during concentration polarization. Reprinted with permission from the Royal Society of Chemistry[63], copyright 2016.

1.3.2.2 Strategies to suppress dendrite formation

However, no model can explain all the dendrite formation mechanisms in a battery system because many factors affect the lithium deposition process, such as SEI properties[66,67] and the current collector surface[68]. For instance, the SEI properties can influence lithium-ion concentration gradients near the anode, the current collector roughness can affect the

distribution of the electric field, and its surface alkali wettability can affect the lithium nucleation process. The electric field is the first driving force for lithium ions' migration and deposition. If the distribution of the electric field is non-uniform (for example, because of current collector surface roughness, etc.), the lithium deposition growth rate will be uneven, thus forming dendrites. Besides, the lithium-ion concentration gradients can be affected by current density, the SEI (ionic conduction and electronic conduction), and electrolyte properties (ionic mobility, viscosity, solvation/desolvation speed, etc), which all contribute to dendrite formation as well.

Thus, the best strategy to prevent dendrites formation in LMBs is to create a uniform deposition environment for lithium ions. The methods include but are not limited to:

(1) Electrolyte additives. Some additives are verified to form a stable and dense SEI on the anode, effectively suppressing lithium dendrite growth and preventing the decomposition of the electrolyte.[69–72] For example, the film-forming additive FEC can form a LiF-rich SEI, which is stable and conductive, thus being beneficial to achieving a dendrite-free morphology of lithium deposits.[73] The coulombic efficiency is increased simultaneously. Adding traditional additives is a simple way to suppress dendrites formation and increase battery performance by adjusting SEI components.[74] However, these additives are gradually consumed during cycling, which is usually a problem for long-term cycling.

(2) Artificial SEI. An ideal SEI requires a uniform distribution around the anode, which has excellent ionic conductivity, robust structure, and good elasticity. Many methods are explored to build an artificial SEI on an anode before cycling, including electrochemical pre-treatment[75,76], chemical pre-treatment[77–79], and physical pre-treatment[80–82]. These treatments significantly suppress dendrite growth and improve battery cycling performance. Archer’s group built an artificial SEI on an anode surface by sputtering a LiF layer, which

achieved smooth lithium plating at a current density of 1 mA cm^{-2}.[83] The reason why sputtering LiF is because the LiF was computed to have lower lithium ions diffusion barriers and higher surface energy than normal SEI components, such as Li_2CO_3, LiOH, and Li_2O. Galvanostatic cycling experiments were performed with LiF-coated Li anode and bare Li anode in several electrolyte systems, the LiF-coated Li anode always showed higher coulombic efficiency and stable cycling performance, suggesting the artificial SEI works during cycling.

(3) High-concentration electrolytes. A high-concentration electrolyte can provide enough Li-ions near the anode, effectively alleviating the diffusion-limited problem based on the "Sand time" theory. In addition, many research works found that the SEI formed by high-concentration electrolytes is thin and dense, which could effectively prevent dead lithium generation and achieve high coulombic efficiency.[21,84–86] By designing electrolyte of 4M lithium bis(fluorosulfonyl)imide in 1,2-dimethoxyethane, an anode free LMB achieved 1000 cycles at 4 mA cm^{-2} with coulombic efficiency of 98.4%.[87] The morphology of deposited lithium is compact and non-dendritic under the scanning electron microscopy (SEM) images, which can be attributed to improving electrolyte reductive stability and greatly decreasing Li^+ diffusion limited problems near the anode.

(4) Anode engineering. Inhomogeneous nucleation of lithium deposits on the current collector is the main reason for dendrite growth. Therefore, building a matrix electrode to regulate lithium growth is a good idea to suppress dendrite formation. Some lithiophilic materials, such as nitrogen (N) doped graphene[88], pyrolyzed N-doped polyacrylonitrile (PAN) binder[89], three-dimensional (3D) oxidized PAN nanofiber[90], and metal-organic frameworks (MOFs)[91], have been employed to guide lithium plating and achieve uniform deposition. The lithiophilic functional groups at the surface could decrease nucleation

overpotential more than copper foil and thus offer more even nucleation sites to form dendrite-free deposits. Designing the anode structure with appropriate micro/nanopores is also an effective method. For example, by employing 3D copper current collector[92–94], carbon nanotube (CNT) buffer architecture[95,96], 3D fibrous Li_7B_6 matrix[97,98] and carbon nanofibers framework[99100], etc., the local current density is reduced due to high surface area, thus preventing dendrite growth.

(5) Solid-state electrolytes. The high modulus of solid-state electrolytes (SSEs) can theoretically suppress dendrite growth and improve battery safety. There are mainly two types of SSEs, inorganic electrolyte (ceramics, like $Li_7La_3Zr_2O_{12}$) and organic electrolyte (polymer, like poly(ethylene oxide)).[101] However, there are still many challenges to the application of SSEs, such as poor ionic conductivity and bad interfacial contact.[102]

1.3.3 Gas formation at the interface

Gas generation is a significant problem affecting LMBs' cycling performance and safety. They are usually formed by side reactions, such as electrolyte decomposition, which could increase battery impedance, aggravate electrode fading, hinder lithium ion diffusion, and considerably raise the battery pressure in the sealed system.[103–105] The gases formed on LMBs anode are similar to that in LIBs because both are formed by reducing solvents and moisture, although more gases may be expected for the reactive LMBs. On-line electrochemical mass spectrometry (OEMS) is a powerful characterization tool to study gas evolution in batteries, and there are already many research works using it in LIBs.[106–108] The possible gas generation reactions are listed in Table 1.1, and the gases are mainly composed of H_2, CO_2, C_2H_4, and CO.

Lithium metal has high reactivity with organic electrolytes with low potential. These reactions are only a small part of gas generation mechanisms because gas formation inside

the battery is a series of complex processes and is hard to predict. The gas is formed along with SEI formation, so it is not practical to avoid the gas bubbles altogether. While still not ideal, some additives were employed to reduce bubble formation or change the formed gas species to improve battery performance.[112,113] How to better control the impact of bubbles on batteries still needs to be explored.

Reactions	References
$2EC + 2e^- + 2Li^+ \rightarrow (CH_2OCO_2Li)_2 + CH_2{=}CH_2\uparrow$	Ref[107,109]
$EC + 2e^- + 2Li^+ \rightarrow Li_2CO_3 + CH_2{=}CH_2\uparrow$	Ref[106,108]
$\text{Trace } 2H_2O + 2e^- + 2Li^+ \rightarrow 2LiOH + H_2\uparrow$	Ref[108]
$2LiOH + 2e^- + 2Li^+ \rightarrow 2Li_2O + H_2\uparrow$	Ref[104]
$H_2O + (CH_2OCO_2Li)_2 \rightarrow Li_2CO_3 + CO_2\uparrow + (CH_2OH)_2$	Ref[21,104]
$2CO_2 + 2e^- + 2Li^+ \rightarrow Li_2CO_3 + CO\uparrow$	Ref[104,106]
$LiPF_6 + H_2O \rightarrow LiF + 2HF + POF_3$	Ref[110,111]
$POF_3 + \text{EC/PC/DMC} \rightarrow \text{Organofluorine compound} + CO_2\uparrow$	Ref[110,111]

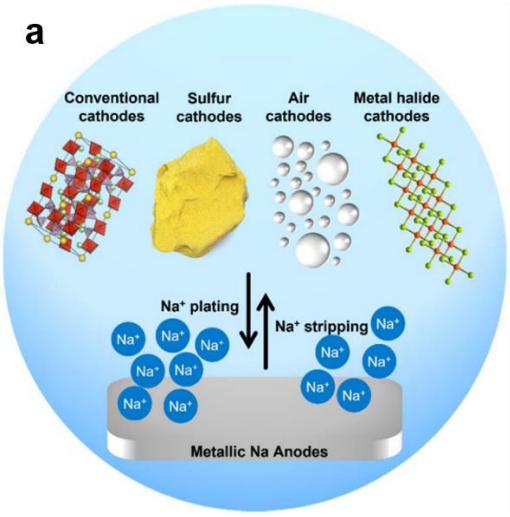
Table 1.1. Part of gas evolution mechanisms in LIBs.

1.4 Introduction and challenges of sodium metal batteries

1.4.1 Sodium metal batteries

Lithium-ion batteries are now widely used in electric vehicles (EV) and commercial energy storage systems. However, lithium resources are limited and are mainly distributed in Australia and South America.[114,115] The large-scale application of LIBs has potential

concerns for the geostrategic and geo-economic bottlenecks.[116] Sodium (Na) has similar properties to lithium, but abundant reserves and wide distribution on the Earth.[117] Thus, sodium batteries theoretically have a significant cost advantage over lithium batteries. With the demand for low-cost and high-capacity energy storage systems, sodium batteries have attracted considerable interest due to promising high energy density chemistries - including Na-sulfur[118–120], Na-oxygen[121–123], and Na-carbon dioxide[124] (Figure 1.6a). A sodium metal anode, with its high theoretical capacity (1,166 mAh g^{-1}) and low electrochemical potential (-2.71 V versus standard hydrogen electrode), is an ideal negative electrode for future sodium batteries. [125,126]



b

Atomic Properties	atomic radius (pm)	covalent radius (pm)	van der Waals radius (pm)	ionization energy (kJ mol^{-1})
Li	152	128 ± 7	182	520.2
Na	186	166 ± 9	227	495.8

Physical Properties	melting point (K)	boiling point (K)	critical point (K)	heat of vaporization (kJ mol^{-1})
Li	454	1603	3220	136
Na	371	1156	2573	97

Mechanical Properties	shear modulus (GPa)	bulk modulus (GPa)	Mosh hardness	Brinell hardness (MPa)
Li	4.2	11	0.6	5
Na	3.3	6.3	0.5	0.69

Bonding to Carbon, Metal Underpotential Deposition on Carbon Surfaces	
Li	strong, yes
Na	weaker, no, or maybe?

Figure 1.6. (a) In potential sodium metal battery systems, the anode is metallic Na, and the cathode has several choices, such as sulfur and conventional layered metal oxides. Reprinted with permission from the Elsevier[127], copyright 2019. (b) Comparison of Li and Na's various physical properties. Reprinted with permission from the American Chemical Society[125], copyright 2014.

Nevertheless, uncontrolled sodium dendrite growth, excessive SEI buildup, and electrolyte depletion during sodium plating/stripping contribute to cell fading.[128–130] There have been many studies into similar failure processes in the lithium metal anode,[44,131]. As sodium is a fellow monovalent alkali metal, it is tempting to conclude that it will exhibit consistent

behaviors with lithium. This is not always the case.[125,132] Sodium has higher reactivity and a larger radius than Li (Figure 1.6b), making the sodium plating/stripping process more complex.[133] Important differences include sodium being more reactive to carbonate solvents[134], not showing the same degree of enhanced performance as known lithium electrolyte additives,[135,136,] and the differing mechanical properties of the sodium metal dendrites[137]. Thus, a dedicated study of the failure mechanisms of the sodium metal anode is necessary.

1.4.2 Challenges of sodium metal batteries

1.4.2.1 The SEI is less stable for sodium metal anode

The components of SEI in the sodium metal anode are similar to that in the lithium metal anode; it is mainly composed of inorganic particles such as Na_2CO_3, NaF, Na_2O, and organic polymers.[134] Researchers found that the SEI components of the sodium metal anode have a higher solubility than the lithium metal anode, which results in a less durable SEI.[138,139] In addition, the sodium metal anode prefers not to polymerize species, forming an unstable organic SEI. The unstable organic SEI results in the non-polymerized SEI parts continuously dissolving.[140] Thus, the SEI does not prevent continuous electrolyte consumption. Electrolyte depletion and excessive SEI formation are one of major failure modes for sodium metal batteries (NMBs).[141] Building a stable SEI is the priority for achieving the application of NMBs.

1.4.2.2 The dendrite growth is more complex in sodium metal anode

As introduced above, there are many studies to learn about lithium dendrite nucleation and growth. However, these theories cannot be directly used to describe sodium dendrites because sodium has many different properties (such as radius, mechanical, and ion transport,

as shown in Figure 1.6b) from lithium.[125] For example, the deposited sodium was observed to dissolve into NP30 (1 M $NaPF_6$ in EC: DMC (v:v) = 1:1) electrolyte gradually during settling (without any electrochemical field). In contrast, lithium deposits were stable in LP30 electrolytes even after left settling for six hours (Figure 1.7).[137] It illustrates that the sodium dendrites have a higher solubility and are unstable in EC: DMC electrolyte, suggesting the interface of sodium metal anode is different than lithium.

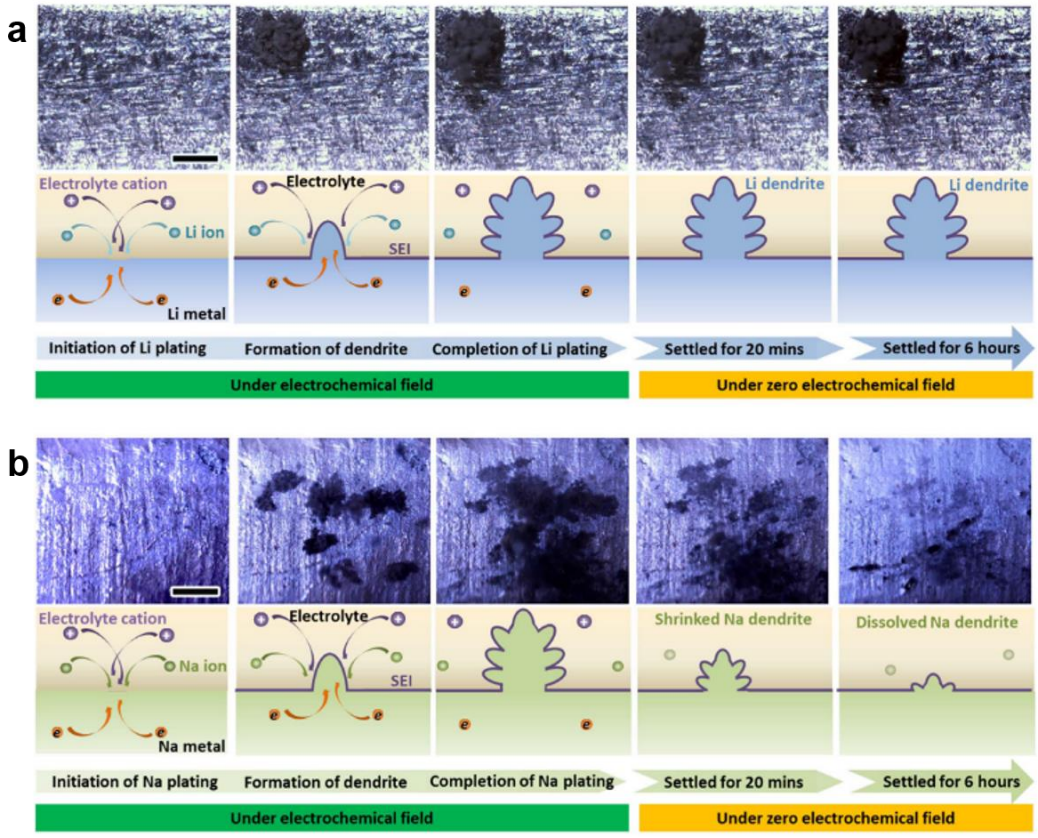


Figure 1.7. In-situ observation of (a) Li and (b) Na deposition and settling process in the normal organic electrolyte at a current density of 0.4 mA cm^{-2}. The electrolytes are 1 M $LiPF_6$ and 1 M $NaPF_6$ in EC: DMC ((v/v) =1:1), respectively. (a) The Li deposits keep stable after a long time, and (b) The Na deposits dissolve into electrolytes gradually during settling. The scale bars are 1 mm in optical microscopic images. Reprinted with permission from the Elsevier,[137] copyright 2018.

The morphology of sodium deposits is usually "needle-like" and mossy, which prefers to gather together and shows a dense distribution, as shown in Figure 1.8.[141,142]. In contrast,

lithium deposits are more likely to be isolated, as shown in Figure 1.4a. The difference may be attributed to the various SEI heterogeneities of the sodium metal anode, promoting the non-isotropic growth of sodium deposits.[125] However, many other influencing factors can result in these differences, such as melting point, ionic diffusion rate, etc. The dendrites' formation mechanisms for sodium, like the nucleation model, still need more studies compared with lithium.

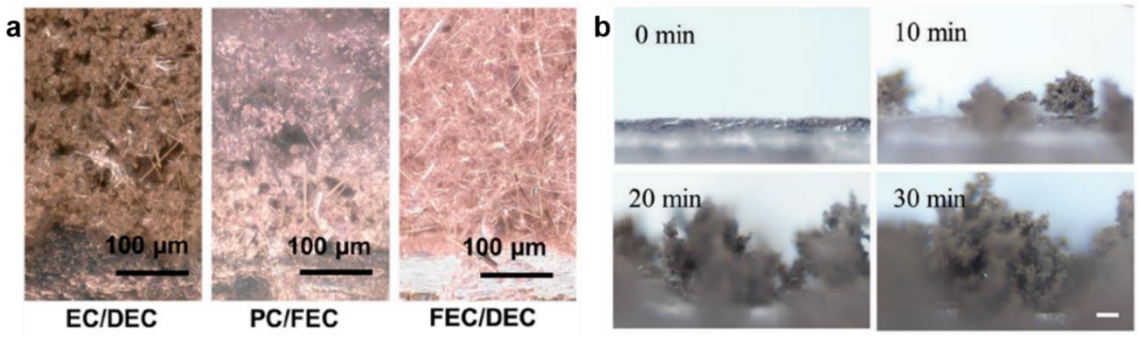


Figure 1.8 Optical microscopy characterization of Na deposits at a current density of 1 mA cm^{-2}. (a) Na deposits from 1 M $NaPF_6$ in EC/DEC, PC/FEC, and FEC/DEC, respectively. The scale bar is 100 μm. Reprinted with permission from the American Chemical Society[142], copyright 2017. (b) Na deposits from 1 M $NaClO_4$ in EC/PC. The scale bar is 50 μm. Reprinted with permission from the John Wiley and Sons[141], copyright 2017.

1.4.2.3 The gas evolution is more severe for the sodium metal anode

Due to sodium metal having higher reactivity than lithium, there are more side reactions during sodium plating, including SEI formation and gas generation. Even when the battery is not applying any voltage, the H_2, CO_2, and C_2H_4 can be produced the moment the sodium metal comes into contact with the NP30 electrolyte, showing severe electrolyte decomposition on the sodium metal anode.[143] By using optical microscopy to observe sodium plating/stripping processes directly, the researchers found that the gas formation was too problematic, seriously affecting the electrical contact of sodium deposits and leading to dead sodium formation.[142,144] The SEI was broken by bubble formation thus

arousing more side reactions, and this decreases the CE. Severe gas formation could be the main degradation factor for NMBs.

1.5 Aim of this work

As discussed in this chapter, there are still many challenges in understanding the metallic anode failure mechanisms. Therefore, my research on operando characterization of lithium/sodium metal batteries aims to understand the fundamental process taking place on the anode side, which leads to the failure of the liquid batteries. By using cutting-edge battery characterization tools, such as operando liquid-cell scanning transmission electron microscopy (LC-STEM), online-mass spectrometry (online-MS), and in-situ atomic force microscopy (AFM), etc., the interfacial degradation on the anode side, like SEI formation and the fatal dendrite growth will be well investigated.

The first part aims to reveal the role of fluoride-rich SEI effects in lithium metal anodes. The fluoride-rich SEI is well known to promote lithium metal battery efficiency, while the mechanism is unclear. By using operando liquid-cell transmission electron microscopy, the nanoscale structural evolution of lithium electrodeposition and dissolution at the electrode surface across fluoride-poor and fluoride-rich interphases could be investigated. By employing the quantitative composition analysis via mass spectrometry, the lithium source consumed by forming SEI and dead lithium could be quantified. Thus, we can learn precisely why the fluoride-rich SEI benefits lithium metal anodes and how they alter the structural dynamics of lithium plating and stripping.

In the second part, this work aims to figure out the role of electrolyte solvents in sodium metal battery anode by comparing it with the sodium cycling performance of carbonate-based and ether-based electrolytes. Sodium presents much poorer cycling performance in a carbonate-based electrolyte, which is different from lithium. Thus, there must be some

unique properties of sodium, an understanding of which will be helpful for future SMBs design references. Using operando TEM and in-situ AFM, the dynamic sodium plating/stripping processes will be carefully studied. Combined with online-MS and DEMS, the gas evolution will be quantitatively measured. Therefore, these two electrolyte systems' SEI composition and mechanical properties will be systematically characterized and compared to determine why the solvents have such significant effects on the sodium metal anode. Through this, we can better understand the sodium metal anode.

Chapter 2. In-situ Liquid TEM

2.1 Introduction of in-situ liquid TEM

As shown in Figure 1.1, the failure processes inside batteries mainly occur at the interface between electrode and electrolyte, such as SEI formation, dendrite growth, and dead lithium generation. These failure states are dynamic and are continually changing along with the battery cycling. However, most characterization methods are post-mortem. For example, many ex-situ tools employed to study the degradation mechanisms of LMBs, including X-ray photoelectron spectroscopy (XPS)[145,146], SEM[147,148], TEM[149], cryo-scanning transmission electron microscopy (cryo-STEM)[21,150], and nuclear magnetic resonance (NMR) spectroscopy[151]. These ex-situ methods are straightforward and can provide helpful information such as electrode and SEI structure component changes. The degradation conclusions are usually obtained by comparing the pristine and cycled states of materials.

Unfortunately, cell disassembly can cause confounding changes to the materials, prompting misleading conclusions. Furthermore, a simple comparison of the before and after states is insufficient to reveal a comprehensive mechanism. Capturing the dynamic changes as they occur is desirable for a more accurate picture. Thus, it is necessary to develop in-situ, real-time characterization methods to characterize the reactions in more representative conditions.

In-situ TEM has been applied to study material degradation mechanisms for years[152–156] because of its extremely high resolution (less than 0.5 Å[157]) and the ability to correlate elemental distribution spatially. As a result, some studies have used the technique to probe anode/cathode material degradation, dendrite growth, and SEI formation. Two strategies for building the in-situ TEM are open-cell and closed-cell configurations. By creating the

small battery cell inside a TEM, the in-situ TEM allows us to study the dynamic evolution of materials' fading in actual battery working conditions and better understand the battery failure.

2.1.1 The open-cell in-situ TEM

The open-cell configuration leaves all battery materials exposed to the TEM vacuum. All the open-cell battery component materials must be vacuum compatible with maintaining the TEM vacuum. Therefore, such open-cell configurations are currently limited to using low vapor-pressure liquid electrolytes or solid electrolytes when studying battery systems.[158–160] There have been a few in-situ TEM research works on the liquid electrolyte lithium battery with an open-cell set-up using ionic liquid electrolytes (ILEs).[161,162] ILEs have negligible vapor pressure at room temperature and make an ideal battery electrolyte to connect a solid cathode and anode in open-cell in-situ TEM. Huang and co-workers[161] first set up the open cell in situ TEM using an ILE in 2010. The nano-battery was composed of a lithium cobalt dioxide ($LiCoO_2$) cathode, an ionic-liquid-based electrolyte, and a single tin dioxide (SnO_2) nanowire as an anode. The SnO_2 nanowire diameter was less than 200 nanometres and was used to observe the lithiation and delithiation process under in-situ TEM. The setup consisted of two gold (Au) rods through which the bias was applied. The ILE was dropped on the $LiCoO_2$ cathode, which was then glued to an Au rod. The SnO_2 nanowires were affixed to the opposite side. This nanoscale electrochemical device represents a LIB system and allows proper real-time characterization under TEM. The main advantages of the ILE liquid configuration are relative ease of sample preparation, with no enclosed cell assembly required. However, the beam-sensitive nature of the ILE is an issue, as it tends to degrade and transform into a jelly state, with reduced ionic conductivity and increased interface impedance. In addition, ILEs are not necessarily comparable to the

carbonate-based electrolytes widely used in practical/commercial LIBs, thus limiting the relevance of insights achieved with this technique.

2.1.2 The closed-cell in-situ TEM

Liquid closed-cell in-situ TEM has recently become widely commercialized; however, it existed for some years before that in the form of lab-built versions. All are fundamentally based on safely encapsulating the liquid between two ultrathin but robust membrane windows so that the cell contents can be safely imaged inside the TEM without being directly exposed to the high vacuum. The early investigations with these systems were used to characterize aqueous-based liquid samples with no biasing, such as studying nanoparticle growth and the solid-liquid interface[163–165]. Battery electrolytes are more viscous than water and typically air-sensitive, so it causes significant additional challenges for in-situ TEM studies. Wang[166] created the first sealed electrochemical liquid cell for in-situ TEM characterization, where the user can operate the electrochemical test synchronously. As is shown in Figure 2.1a, the setup consists of two silicon chips arranged like a sandwich but sealed by O-rings. Each silicon chip contains a silicon nitride window (around 30 nanometres thick) to allow the electron beam to transmit. The electrochemical device uses a silicon nanowire as a working electrode connected to platinum contacts. Then the biasing can be applied from the patterned platinum electrodes in the top chip, as illustrated in Figure 2.1b. Because the whole cell is perfectly sealed, a standard electrolyte used in commercial lithium-ion batteries such as lithium perchlorate, $LiClO_4$-containing mixed EC, and DMC can be employed. As a result, the lithiation and delithiation electrochemistry cycle can be studied, and the entire dynamic process can be recorded. This setup is an excellent example of studying battery chemistry mechanisms with practical battery electrolytes in in-situ TEM.

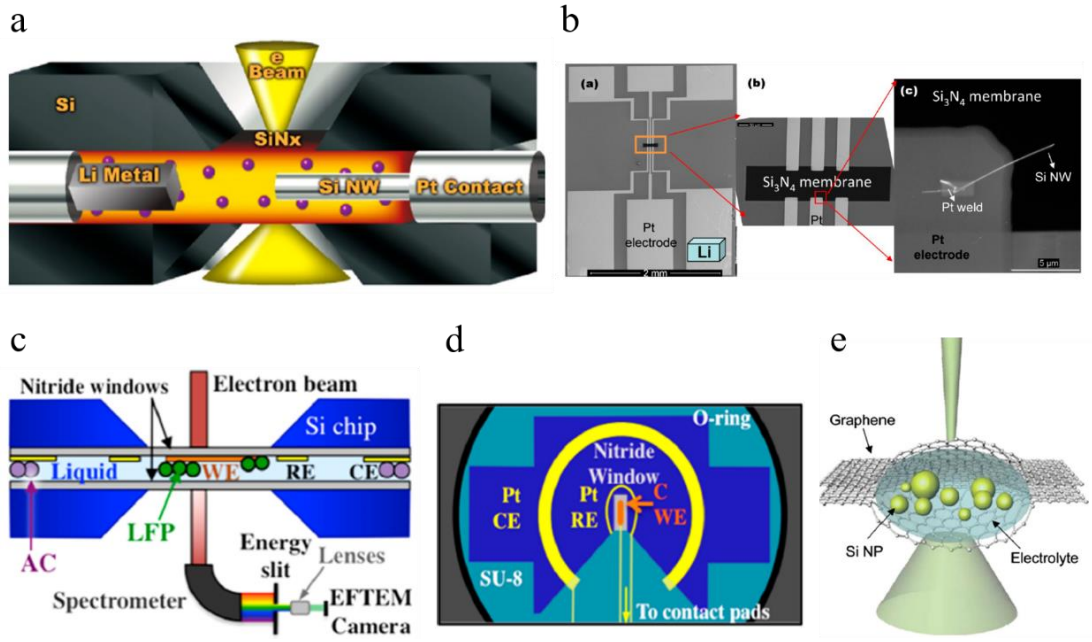


Figure 2.1. Schematic drawings of sealed liquid cells. (a) The electrolyte is sealed between two silicon chips in this liquid cell setup. The electron beam can go through the two-silicon nitride membranes. Reprinted with permission from American Chemical Society[166], copyright 2013. (b) In The SEM image of the silicon chip electrode system of liquid cell in (a), there are six electrodes patterned on the silicon nitride membrane, which supplies the bias. Silicon nanowires as a working electrode are attached to the top window electrode. Reprinted with permission from American Chemical Society[166], copyright 2013. (c) In the cross-section view of the improved liquid cell holder, the system has three electrodes made from glassy carbon or platinum. Only the working electrode is on the viewing window, and the active material is deposited on it. Reprinted with permission from American Chemical Society[167], copyright 2014. (d) The top chip is patterned with three electrodes. The working electrode is on the membrane, and the reference and counter electrodes are outside. Reprinted with permission from American Chemical Society[167], copyright 2014. (e) Making a graphene "bubble" closed cell can get higher resolutions due to being a thinner window material and allowing for a thinner liquid layer. However, it cannot qualify for liquid flow or electrical biasing. Reprinted with permission from American Chemical Society[168], copyright 2014.

Muller's team[167] developed a new TEM liquid flow cell with an improved electrode design, as displayed in Figure 2.1c-d. The electrochemistry is based on a three-electrode system with all electrodes fabricated on the silicon chip. The working electrode is carbon and patterned on a silicon nitride membrane. Both the reference and counter electrodes are made of platinum and will not affect the electrochemical activity. The cathode material $LiFePO_4$ is printed on the working electrode in advance, and the charge/discharge process is studied in a 0.5 M Li_2SO_4 aqueous electrolyte. Also, they implemented the idea of using valence

energy-filtered TEM (EFTEM) to observe the lithiation process within the cathode material and achieve nanoscale imaging and analysis.

The flow cell included microfluidic lines, connecting the in-situ closed cell to the outside of the TEM, where a pump can cycle and replenish the liquid electrolyte sample. Being able to continuously flow and replenish the liquid inside the cell from outside the TEM is crucially important, as the closed-cell contains a tiny volume of liquid. As a result, the reactants contained in the liquid may be rapidly depleted during a reaction. This can distort the interpretation of any system studied, as the corresponding ex-situ system will likely not be reactant limited in the same way. With batteries, parameters such as the diffusion concentration gradient at the electrode interface are essential in controlling SEI formation and lithium cycling; thus, a rapidly depleting electrolyte would not represent a practical cell. Continuous liquid flow can mitigate this problem in the closed-cell system and is a significant advantage over other in-situ liquid TEM approaches.

However, with closed liquid cells, the relatively large overall thickness of the cell significantly impedes the resolution that can be achieved. This is made worse by window bowing arising from the substantial difference in pressure between the two sides of the membrane windows, with the TEM vacuum on one side and the standard atmospheric pressure of the liquid inside. Thus, the membrane windows bow outward significantly, expanding into the TEM vacuum and increasing the thickness of the liquid layer. For higher resolution, Lee's team members[168] used graphene to replace the silicon nitride membranes. They were able to get real-time high-resolution in-situ TEM analysis of nanoparticle dynamics (Figure 2.1e). However, as seen from the figure schematic, these closed cells are fully sealed "bubble" cells, which means they cannot include electrical contacts. Thus, they cannot allow for electrochemical studies nor continuous liquid replacement by liquid flow,

suggesting a minimal reactant supply for any study of chemical reactions.

2.1.3 Discussion of the two kinds of in-situ TEM cells

Developing in-situ TEM techniques discussed above has made the high-resolution characterization of lithium-ion battery electrochemical dynamics viable. The open-cell configuration and closed-liquid cell have merits and defects. In general, the advantages of open-cell include: (1) A relatively large space for the sample, making it easier to mount electrode material and manipulate it within the TEM. (2) The atomic-scale resolution, due to the imaging of the electrode material directly without any impeding liquid and window. (3) The ability to easily use other high-resolution compositional analysis tools such as electron energy loss spectra (EELS) and energy-dispersive X-ray spectroscopy (EDS). However, there are also distinct disadvantages (1) The contact of the interface is usually bad, causing higher overpotential due to being assembled *in-situ* by the piezo-probe. (2) It does not support using suitable LIB electrolytes, as they will evaporate in the vacuum. (3) The ILE electrolyte is highly beam-sensitive, and its morphology and ionic conductivity undergo significant degradation upon exposure to the beam.

The sealed liquid cell is more complicated and arguably more like a miniaturized battery cell. Its main advantages are: (1) it is compatible with almost any liquid electrolyte, with the only limitations being if the sample has any reactivity with the cell components. (2) The complete interface between the electrode and electrolyte, and the changes to the SEI, can be observed. (3) The electrochemical measurement is more reliable, with better interfacial contact. (4) The electrolyte quantity and quality are maintained by continuous flow replenishment from outside, as by-products made by the electron beam are flushed away, and its concentration is maintained. Alongside this, the technique has some limitations: (1) The system is complex; it is difficult to use and expensive to operate. (2) There is a risk of

liquid leaking into the TEM column due to membrane rupture. (3) The spatial resolution is relatively poor due to observation through the membranes and the thick liquid layer. (4) Limited space (a few hundred nanometres thick) causes a large overpotential and somewhat different CV cycles[169] compared with a conventional battery cell, so it is not completely representative of a real battery system. (5) Most scattered electron signals and characteristic X-rays are blocked by membranes and silicon chips, so it is hard to use EELS or EDS to analyze elements. (6) The delicate nature of the suspended membrane windows, where the working electrode is located, combined with the small electrode size, makes it challenging to mount different battery electrode sample materials.

2.2 Application of in-situ liquid TEM

The relationship between electrode structural changes and electrochemical reactions can be established by recording the battery failure evolution process in real-time. Therefore, the most significant advantage of in-situ liquid TEM is studying the dynamic reactions on the electrode during cycling. This section will briefly review the application of in-situ liquid TEM to study the LIBs failure mechanisms.

2.2.1 Degradation process at the electrode interface

Most degradation processes occur at the interface between electrode and electrolyte, such as the SEI formation, dendrite growth, dead Li generation, and bubble formation. These side reactions greatly influence the battery performance, so in-situ TEM is usually one of the primary study objects.

Zeng *et al.*[170] characterized the electrochemical lithium plating/stripping process on an Au electrode with improved electrochemical liquid TEM closed-cells. The evolution of

lithiation/delithiation, dendrite growth, the Li-Au alloying, and SEI formation processes were captured under applied CV signals. They used LP30 as the electrolyte, which is a representative commercial battery electrolyte. During the cyclic voltammetry from 0 V to -3 V, some tiny bubbles from side reactions were generated at -2.75 V first, and lithium reacted with the gold electrode and formed a Li-Au alloy layer almost at the same time (Figure 2.2). After applying the negative voltage further, a giant bubble formed, and dendrites grew on the Li-Au alloy layer. During the stripping process, the dendrites disappeared gradually, and the alloy layer decreased to 339 nm. Also, they observed a uniform SEI layer formation from the reduction of the organic electrolyte. The thickness of this SEI film was approximately 200 nm, and some more bubbles were generated in this process. From their experiment, two conclusions can be obtained; the SEI formed is poor at conducting electrons, and the SEI is produced by both reduction of electrolyte and oxidizing of the electrode surface. Overall, although the system did not control the effects of the electron beam, their in-situ study shows valuable insight into understanding the interface mechanisms during the charge cycling processes in actual batteries.

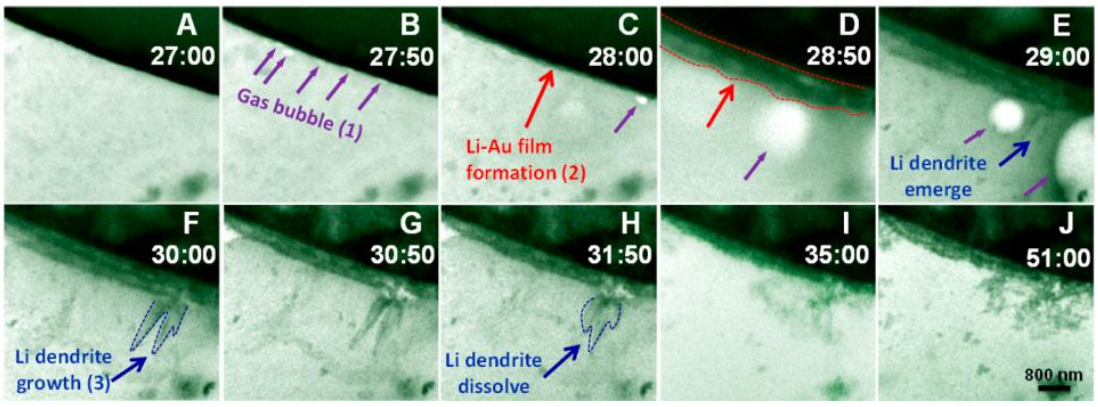


Figure 2.2. The dynamic process of electrode interface during cycling. (A-D) The gas bubble and Li-Au layer formed gradually; (E-G) lithium dendrite appears and grows during planting; (H-J) lithium dendrite dissolves gradually in the stripping process. Reprinted with permission from American Chemical Society[170], copyright 2014.

With the help of a commercial liquid-cell TEM holder, Mehdi et al. [169] studied the lithium charging/discharging evolution on platinum electrodes with a low electron dose in STEM mode (≤ 0.3 electrons/Å^2/s). The plating/stripping process at the interface of the Pt electrode in the $LiPF_6$ in PC electrolyte was recorded, and the SEI formation, dendrite growth, and "dead Li" generation were observed (Figure 2.3). Besides, they proposed a "mass-thickness contrast" method to identify the composition of the products (for example, Li is a light metal and less dense than the surrounding electrolyte, so it should be the darkest in STEM). In terms of the method, they found that; (1) there were some "dead Li," which had lost contact with the electrode and could not be stripped away; (2) the SEI layer formed at the interface, and its thickness was related to the electric field distribution over the electrode; (3) the Li-Pt alloying and dealloying process also happened at the outer layer of the Pt electrode. Furthermore, they combined the structural evolution with CV analysis so that the electrochemical dynamics of lithium plating/stripping could be better understood.

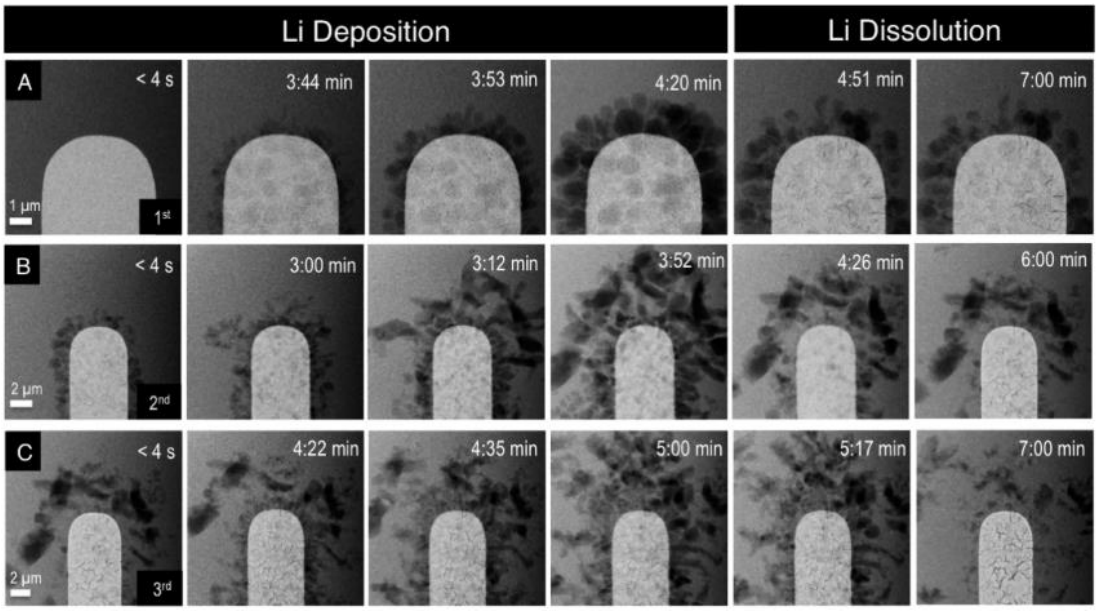


Figure 2.3. The evolution process of lithium deposition/dissolution at a Pt electrode over the first three cycles in HAADF STEM. Some lithium (most black objects) deposited and dissolved at the Pt electrode under CV bias. (a) First cycle; (b) second cycle; (c) third cycle. Reprinted with permission from American Chemical Society[169], copyright 2015.

In addition, Unocic and his co-workers performed many in-situ TEM studies on the battery SEI formation with different anode materials, such as gold[171], graphite[172], and glassy carbon[173]. All studies illustrated that the SEI was formed before lithium deposition and could remain at the interface after lithium plating and stripping, which helps us dynamically understand the electrochemical processes of the electrode interface reactions.

2.2.2 Electrode changes during lithiation/delithiation

There are three main mechanisms for Li-ions to be stored in battery electrode materials; intercalation, alloying, and conversion, depending on if the Li-ion incorporation leads to a structural change of the host or if it leads to the formation of a new compound. To improve electrode cycling performance, the first step is to identify the lithiation/delithiation mechanisms of the electrode. In-situ TEM is one of the ideal characterization tools to study the electrode dynamics during cycling because it can study the electrode lithiation/delithiation process at the nanoscale.

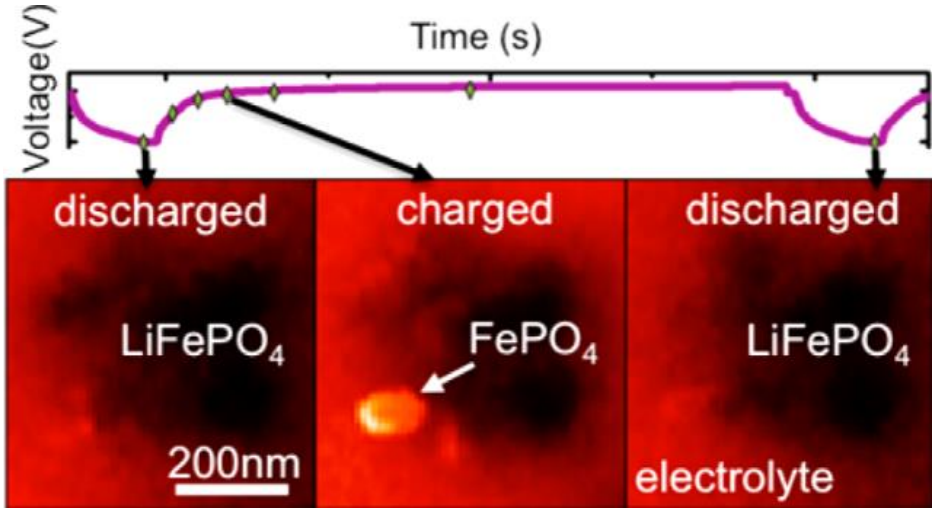


Figure 2.4. In-situ study of $LiFePO_4$ behavior during cycling in the electrolyte under EFTEM. The bright part is charged $FePO_4$ and the dark part is the discharged $LiFePO_4$. Reprinted with permission from American Chemical Society[167], copyright 2014.

For example, $LiFePO_4$ is a typical cathode material that stores lithium ions by an intercalation mechanism. It is a promising cathode material to use as energy storage for LIBs because of its stable orthorhombic crystal structure, enabling excellent cycling performance. However, the particle combination process with lithium ions is usually uneven, and the material's ionic and electronic conductivities are poor, making its performance unexpectedly bad. Many models explain its failures, such as the mosaic model[174], shrinking-core model[175], and core-shell model[176]. Holtz et al.[167] utilized EFTEM on an in-situ liquid cell to track the ions' valence state during $LiFePO_4$ charging/discharging in 0.5 M Li_2SO_4 aqueous electrolyte. They found clear evidence of a core-shell type structure during the charging process, and the particles appeared to be fractured, which was related to the mass loss (Figure 2.4). In addition, the particle-by-particle delithiation process was observed, and anisotropic nucleation was demonstrated.

2.3 Beam effects of in-situ liquid TEM

From Egerton[177], the beam damage interactions in TEM are mainly four types. (1) Atomic displacement, or knock-on damage, is caused by elastic scattering from the high energy transmitted beam. The damage is related to the electron energy, so it can be avoided by reducing incident beam energy. (2) Heating, is due to inelastic scattering such as electron collision, and the primary cause is high incident electron flux. (3) Charging, due to charge build-up is ubiquitous in some semiconductors and insulators. (4) Radiolysis, where the electron beam causes degradation by secondary electrons breaking bonds. A cool environment can dramatically decrease the radiolysis, achievable by cryo-TEM. A high incident beam energy can also reduce radiolysis as a longer electron mean free path will reduce the sample damage cross-section. In general, the alkali halides and organic materials

are very radiation-sensitive, so radiolysis is usually the primary damage effect during the characterization of battery materials.

In in-situ TEM, the electron is generated by a high energy (hundreds KeV) electron gun, which causes many side reactions and radiolysis products in samples. Hence, to improve the reliability of research, the beam effects have to be understood. In general, the influences are variable in different materials and environments. The side reactions in a liquid cell caused by the electron beam are more complex than in an open cell, such as the liquid decomposing[178], bubble formation[179], and nanoparticle cluster/precipitation[180]. Leenheer et al.[181] discovered that the beam could induce SEI formation during the first cycle in liquid in-situ TEM, and the SEI could change the lithium growth morphology even in low-dose mode. Abellan et al.[178] compared a series of general battery electrolytes and found that lithium salts had different stability under in-situ TEM. For instance, $LiAsF_6$ was easily reduced by solvated electrons from liquid and following formed AsF_3 and LiF. On the other hand, $LiPF_6$ in the same solvent (EC/DMC) was more stable under the same beam condition, while lithium triflat (LiTf) was the most stable.

As a result, it is essential to minimize beam effects during the in-situ TEM study, for example, by reducing beam dose or increasing the electron energy. However, beam damage factors such as radiolysis, heating, and solvated electrons play different roles in different systems, so the specific actions should depend on the given conditions. For example, Grogan and co-workers[182] found that radiolysis has distinct effects during electron beam irradiation of pure water, while heating has little impact.

2.4 Summary of in-situ liquid TEM application in LIBs

In conclusion, in-situ TEM has been an indispensable advanced characterization method to help understand the fundamental mechanisms inside batteries. Based on its high resolution and powerful spectroscopy capability, it makes a real-time study of electrochemical dynamics at the nanoscale possible. Taking advantage of in-situ TEM, SEI formation, dendrite growth, and electrode degradation mechanisms have been widely studied, and the results have helped inform the development of LIBs.

However, there are also directions for potential improvement: (1) Making the in-situ system a better representation of the actual battery. (2) Improving imaging resolution with the liquid cell. (3) Improve our understanding of electron beam effects and reduce them. (4) Develop fast detection techniques to capture dynamic changes better. The first two will require improvements to the in-situ techniques, such as limiting window bowing in the closed liquid cell and thus reducing the liquid thickness and improving resolution. The latter two depend on developing new TEM methods, including employing high-efficiency direct electron detectors, allowing for reduced beam currents to be used.

Chapter 3. Experimental Techniques

This chapter will introduce the experimental techniques used in this work, including sample preparation, electrochemical methods, and characterization tools.

3.1 Sample preparation

The samples in this project are mainly used to make lithium/sodium metal batteries or lithium/sodium ion batteries, which mainly include anodes, separators, electrolytes, and cathodes. The anodes of lithium and sodium metal were bought from Sigma-Aldrich and saved properly in the glovebox. The hard carbon anode and $Na_3V_2(PO_4)_3$ cathode were both purchased from MTI Kejing Corporation (Shenzhen, China) and were used without any further processing. The electrolytes for LMBs were 1 M $LiPF_6$ in EC/DMC = 50/50 (v/v) (battery grade, Sigma-Aldrich) with and without 5wt.% FEC (anhydrous, ≥ 99%, Sigma-Aldrich). The electrolytes for SMBs were 1 M $NaPF_6$ in EC/DMC = 50/50 (v/v) (battery grade, Kishida Chemical) with and without 10 wt.% FEC and VC (anhydrous, ≥ 99%, Sigma-Aldrich), and 1 M $NaPF_6$ in DME (anhydrous, ≥ 99.5%, Sigma-Aldrich). All the electrolytes were dried with 4 Å molecular sieves (Aldrich) for more than a week before using in experiments. The separators used include glass microfiber (Whatman GF/D) and Celgard 3501.

Two kinds of coin cell batteries are distinguished by the separator that is used in this project. To do quantification work of the cycled coin cell, there are two pieces of glass microfiber separators (Whatman GF/D, dried under a vacuum oven) used in Li||Cu CR2032 coin cells for online MS experiments. The glass fiber near the anode could help to protect dead lithium/sodium and SEI structures, to make sure the quantification experiment is accurate.

However, the glass fibers easily stick to the sample and contaminate the sample surface, they usually do not use for the surface morphology and elemental characterization. In this case, the separators used Celgard 3501 to make coin cells for the SEM, SIMS, and AFM characterizations.

For sample preparation processes, all the electrolyte preparation and cell assembly/disassembly were performed in an argon-filled glove box (H_2O < 0.1ppm, O_2 < 0.1ppm). The water content of prepared electrolytes was measured by Karl Fischer titration (C30S Coulometric KF Titrator, Mettler Toledo) with methanol-free reagents three times, each showing a water content value of <5 ppm. During the electrolyte preparation process, all the tools we used (which include syringes, vials, tweezers, etc.) are dried in a vacuum oven for over 12 hours before bringing into the glove box. The Cu current collectors were first immersed in diluted hydrochloric acid for twenty minutes and washed with deionized water twice, then transferred to an antechamber of the glove box quickly, making it dry in a vacuum state.

3.2 Electrochemical methods

3.2.1 Cyclic voltammetry (CV)

CV is a powerful method for studying materials' reduction and electrochemical oxidation processes. When the electrode is applied with potential, a corresponding current will occur. Like Figure 3.1, when a potential is scanned from high potentials to low potentials (low enough to make sample reduction), the sample gets electrons and occurs reduction reaction to make corresponding current; then the potential is scanned from low potentials to high potentials, the sample loses electrons and occurs oxidation reaction.[183] If setting the potential scanning range that enables reduction and oxidation reactions to occur alternately

on the electrode, this method is called cyclic voltammetry. Scan rate is an important factor for a CV. For example, a scan rate of 20mV s^{-1} means the potential varied 20mV linearly per second. In this work, the CV was employed to study the Li plating/stripping behavior in in-situ liquid TEM by a Gamry workstation. The voltage range was from 0V to -4V and then came back to 0V, and the scan rate is 20mV s^{-1}. During this scanning process, the corresponding current was recorded. The more extensive current at the specific voltage point, the more reactions happened. Additionally, the reversibility can also be measured from the ratio of oxidation area and reduction area.

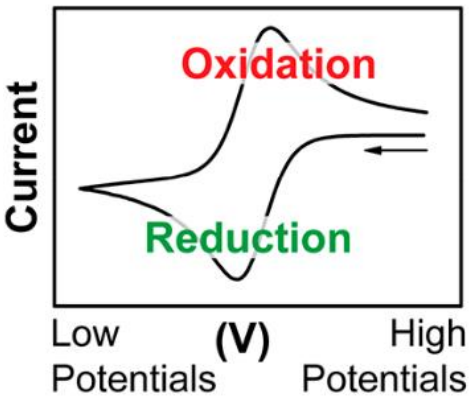


Figure 3.1. The IUPAC convention of CV. A potential scan from high potentials to low potentials (reduction process of the sample) first, and then a scan from low potentials to high potentials (oxidation process of the sample). Reprinted with permission from American Chemical Society[183], copyright 2020.

3.2.2 Galvanostatic cycling

Galvanostatic cycling uses constant current to charge/discharge the battery, and it is one of the most popular ways to study battery cycling capacity. In this project, galvanostatic cycling is mainly used for testing the Li||Cu and Na||Cu coin-cells. During galvanostatic cycling, the first thing is to calculate the surface area of the electrode thus controlling the current density of the experiment. The cell is applied a specific minus current to enable Li/Na plating firstly and then applied a positive current to enable Li/Na stripping. For

experiment details, the current density is controlled by the specific current over the electrode surface area; the plating capacity is controlled by current density multiplying deposition time, and the stripping is stopped at a high cut-off potential. Therefore, coulombic efficiency can be calculated by stripping time over plating time. In addition, the rate test can also be performed by controlling a series of current densities. The galvanostatic cycling measurements were performed on a Biologic VMP3 system in this project.

3.2.3 Electrochemical impedance spectroscopy

Electrochemical impedance spectroscopy (EIS) is widely used to measure systems' capacitance, resistance, and ionic conductivity. By applying a small alternating current (AC) excitation signal according to the sinusoidal law in the battery, a corresponding sinusoidal AC with the same frequency and a phase shift will respond. Then the impedance can be calculated by Ohm's law below[184]:

$$Z = \frac{V_t}{I_t} = \frac{V_0 \sin(\omega t)}{I_0 \sin(\omega t+\varphi)} = Z_0 \frac{\sin(\omega t)}{\sin(\omega t+\varphi)} \qquad (3.1)$$

In the equation, Z is the impedance, t is the time, V_t is the voltage at time t, I_t is current at time t, V_0 and I_0 are voltage and current at time zero. ω is the angular frequency expressed by the formula: $\omega = 2\pi f$.

By employing the Euler relationship:

$$e^{i\varphi} = cos\varphi + isin\varphi \qquad (3.2)$$

The impedance formula can be represented in the complex form:

$$Z(\omega) = \frac{V_t}{I_t} = Z_0 e^{i\varphi} = Z_0(cos\varphi + isin\varphi) \qquad (3.3)$$

Nyquist plots are the most popular way during battery research for expressing the impedance, using $isin\varphi$ as the imaginary part for the y-axis and the $cos\varphi$ as the actual part for the x-axis (as shown in Figure 3.2).

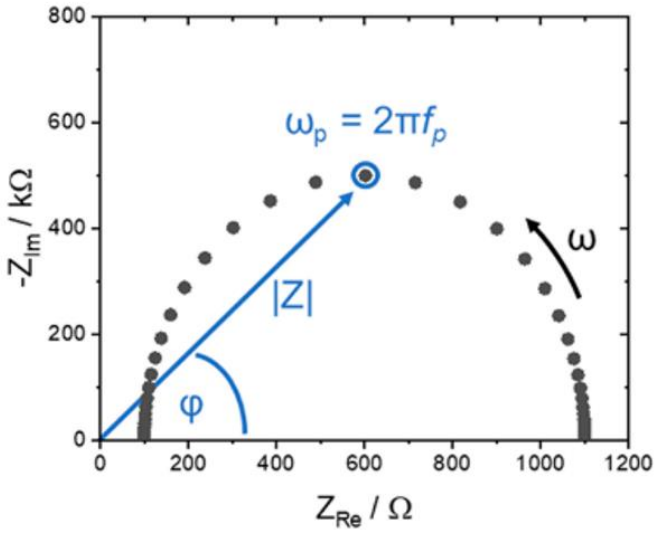


Figure 3.2. Nyquist plots of the EIS. The frequency ω decreases from left to right, and the impedance which is defined by a vector (modulus |Z| and phase angle φ) corresponds to every point of frequency. Reprinted with permission from American Chemical Society[184], copyright 2020.

In this project, the EIS was used to compare the ionic conductivity of the SEI for different coin cell systems. In a lithium/sodium metal battery system, there are usually several resistance and capacitance contributions for charge transfer. Thus, the individual impedance contributions of the coin cell can be well understood by fitting with an equivalent circuit model (including resistors, inductors, capacitors, diffusion elements, and constant phase elements).[184] In a cycled Li||Cu coin cell, the lithium is deposited on Cu current collector, and the lithium was covered by the SEI layer. The EIS was measured from 1 MHz to 1 mHz using Bio-Logic VMP3 Potentiostat at room temperature (20℃). According to the EIS model in simple Li||Cu half-cell,[184] at the high frequencies (around or above 1 KHz), the impedance is mainly contributed by lithium ions migration in the electrolyte (electrolyte resistance R_Ω); at low frequencies (below 1 Hz), the impedance is contributed by lithium

ions diffusion within the electrodes (diffusion resistance); at middle frequencies, the impedance is primarily contributed by charge transfer at the interface (charge transfer resistance R_{ct}). The R_{ct} is the ability of charge conductivity (including ionic conductivity and electron conductivity) at the interface, and researchers usually use this number to approximately express the ionic conductivity of SEI. As shown in Figure 3.3, the Nyquist plot of the Li||Cu half-cell at room temperature usually performs a semicircle arc and a tail. The chord length of the semicircle arc could roughly present R_{ct}, therefore, the chord length could use to compare the impedance of lithium ions diffusion in SEI film. The shorter the chord length presents the better lithium ions conductivity.

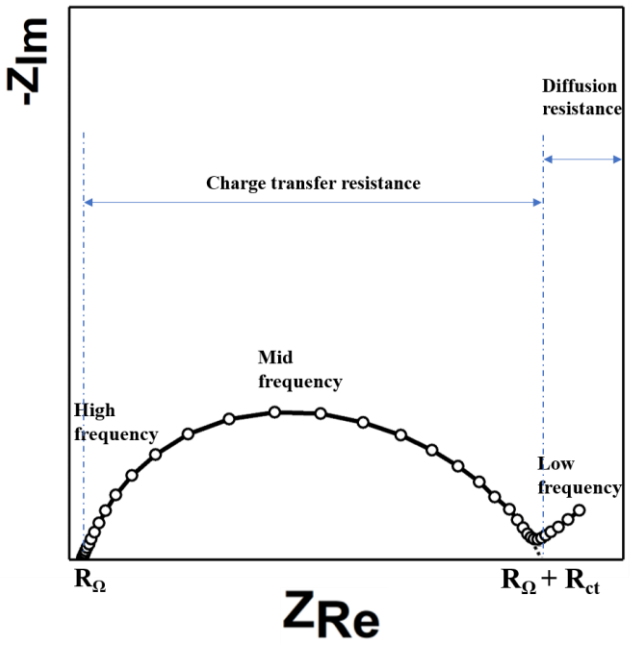


Figure 3.3. Illustration of EIS Nyquist plot for a Li||Cu half-cell used in this project.

3.3 Characterization techniques

3.3.1 Scanning electron microscopy (SEM)

Scanning electron microscopy (SEM) plays an essential role in the research field of materials and is widely used in studying the morphology of various materials. During SEM

characterization, the electron gun emitted an electron beam under an accelerating voltage, converged through the electromagnetic lens system to form a small electron beam, and focused on the sample surface. Due to the interaction of the high-energy electron beam with the specimen material, various information is generated as a result: secondary electrons, backscattering electrons, X-rays and Auger electrons, etc (shown in Figure 3.4). These signals are picked up by the appropriate receiver, amplified, and sent to form the morphology information of materials.

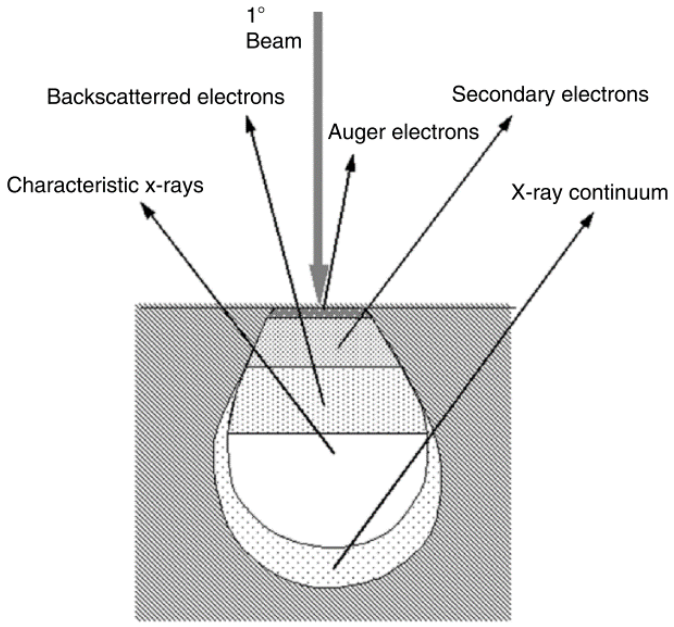


Figure 3.4. The diagram of generated signals and the regions where can collect them. These characteristic X-rays, Auger electrons, secondary electrons, and backscattered electrons are all generated by the interaction of electron beams and samples. Reprinted with permission from Springer Nature[185], copyright 2006.

Due to the short wavelength of electron beams, the SEM could have wonderful characterization resolution, according to Abbe's equation:[185]

$$d = 0.612\lambda/nsin\alpha \qquad (3.4)$$

In this equation, d is resolution, λ is the wavelength of imaging radiation, n is the index of

refraction of medium between point source and lens, relative to free space, α is half the angle of the cone of light from specimen plane accepted by the objective (half aperture angle in radians).

The secondary electrons are formed by the incident electron beam that strikes the sample surface, and they are used to supply topographic information about the surface. Therefore, SEM is widely used to characterize the morphology of nano-sized battery materials. In this project, SEM (Carl Zeiss Merlin SEM) is used to look at the morphology of lithium and sodium deposit structures. Because both of the materials are air-sensitive, the air-tight holder is employed during the transfer process to protect the specimen.

EDX (energy-dispersive X-ray) is also another powerful function based on SEM. When the incident electron beam hits the specimen atoms and knocks off an electron from the inner shell, another outer shell electron is attracted to fill this vacancy. Due to the outer shell electron moving from a high energy to a low energy position, it will release in a form of an X-ray. This is the characteristic X-ray and it can be used to study the chemical composition of materials. In this project, the EDX is used to characterize the deposited sodium after battery cycling, and the elements distribution of the specimen can be well studied. However, the EDX is hard to get the signals from light elements, such as lithium.

3.3.2 Focused ion beam (FIB)

A focused ion beam (FIB) is usually used to mill and make microfabrication of samples by using larger ion sources such as Ga^+ and Xe^+. The ions are focused and accelerated, which can sputter the sample surface. The material can be milled by carefully controlling energy and sputtering. In this project, the FIB is used to mill Li/Na deposits, and thus is convenient to get the cross-section images by SEM

3.3.3 Secondary ion mass spectrometer (SIMS)

A secondary ion mass spectrometer (SIMS) is a surface analysis technique based on the interaction of primary ions on the surface of a sample. The principle is that a primary ion beam with high energy hits the sample surface. Then many particles are formed in this sputtering area, including secondary electrons, neutral particles, secondary ions, etc. Collecting secondary ions through a mass spectrometer can obtain the material's surface composition information.

SIMS is a sensitive analytical method that can provide information on the distribution of light elements like lithium,[186] which are challenging to analyze by other characterization techniques. Thus, the SIMS is specially used to analyze the light elements such as lithium ions and fluorine ions of deposited lithium/sodium to investigate the compositional differences of SEI formed in lithium/sodium metal batteries. In this project, a Thermo Scientific Helios G4 Plasma FIB DualBeam (or PFIB) system combined with a Hiden Analytical EQS quadrupole SIMS detector was employed to compare the fluorine contents in different SEI structures. The detailed distribution of fluorine in the deposited lithium was investigated by the SIMS depth profiling technique. Through the identification of signals of $^{7}Li^{-}$, $^{16}O^{-}$, and $^{19}F^{-}$ from the sample and controlling the same experimental parameters, the levels of fluorine enrichment in the systems could be semi-quantitatively compared using the $^{19}F/^{7}Li^{-}$ ratios.

In this experiment, an area of 15 μm × 15 μm (100 × 100 pixels) from the deposited lithium sample was sputtered using a focussed beam of Xe^{+} at 30 kV and 4 nA and a dwell time of 0.2 ms per pixel. For both samples these scans were repeated for several cycles (each cycle includes three frames corresponding to the three signals) from the same area, giving three stacks of images showing the distributions of each element through the thickness of the

plated Li layers. ImageJ was used to create elemental depth profiles. To minimize edge-related effects during SIMS analysis, only the pixels more than 2.5 μm away from the edge of the raster regions were selected for in-depth profiling.

3.3.4 Differential Electrochemical Mass Spectrometry (DEMS)

Differential Electrochemical Mass Spectrometry (DEMS) is a technique that combines electrochemical measurement and mass spectrometer. The setup is shown in Figure 3.5. First of all, the whole setup is based on a mass spectrometer and which is used to analyze the gas blowing in. There is an in-situ large-sized coin cell before the mass spectrometer and it is connected to a BioLogic workstation to supply electrochemical signals. The coin cell is specially designed and it has a gas inlet and a gas outlet, thus the generated gas during electrochemical reactions could be blown into the mass spectrometer. To protect the mass spectrometer, a cold trap system is added between the in-situ coin cell and the mass spectrometer. The cold trap could effectively prevent electrolytes from entering the mass spectrometer, without affecting the gas. An argon (Ar) source is always supplied in the whole gas circuit and the flow rate is well controlled by a digital flow meter (Bronkhorst).

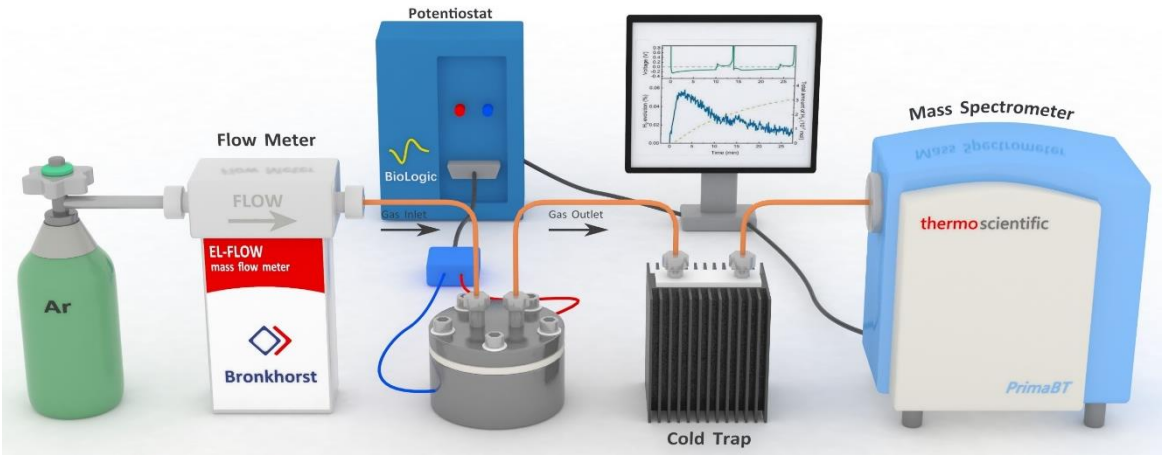


Figure 3.5. The illustration of the DEMS system used in this project. The Ar is the carrier gas, and the cold trap is designed to prevent electrolytes from flowing into a mass spectrometer.

During DEMS measurement, the in-situ coin cell is connected to this gas circuit first and the gas tightness of the whole setup is then checked. If all works well, then corresponding electrochemical signals such as galvanostatic charge/discharge are supplied to the coin cell. The formed gas from the in-situ coin cell can be flowed into the mass spectrometer with carrier gas Ar and characterized by the mass spectrometer. Depending on the mass of gas, the species and quantity of gas such as H_2, O_2, and CO_2 could be measured. Therefore, we can know well about the gas emission of the battery cycling, without damage to batteries.

In this project, the specially designed large in-situ coin cells (Li||Cu and Na||Cu) are assembled in the glovebox first and then connected to the DEMS. The battery materials used in the large cells such as electrolytes, lithium/sodium metal, separators, and Cu foils are all consistent with the normal coin cells, so the results are representative. A normal battery system is a sealed system and it is hard to detect the gas formation during reactions. By using the DEMS method, the species and quantity of generated gas during side reactions of the battery could be well in-situ studied. Therefore, DEMS is widely used to characterize the emitted gas during an electrochemical process in real time.

Based on the DEMS system introduced above, an online mass spectrometer (online-MS) setup was designed to study the dead lithium/sodium and SEI components of cycled batteries. The details of online-MS setup (built in-lab) are illustrated in Figure 3.6. This is an ex-situ method and the in-situ coin cell in DEMS is replaced with a rubber sealed vial. The setup idea is from isotopic analytical methods, which use hydrogen isotopes (hydrogen and deuterium) to distinguish dead lithium and LiH in SEI. Thus, the amount of dead lithium and LiH in cycled Li||Cu battery could be measured quantitatively. The details are introduced below. The quantitative study is quite helpful to understand the degradation mechanisms of lithium/sodium metal batteries.

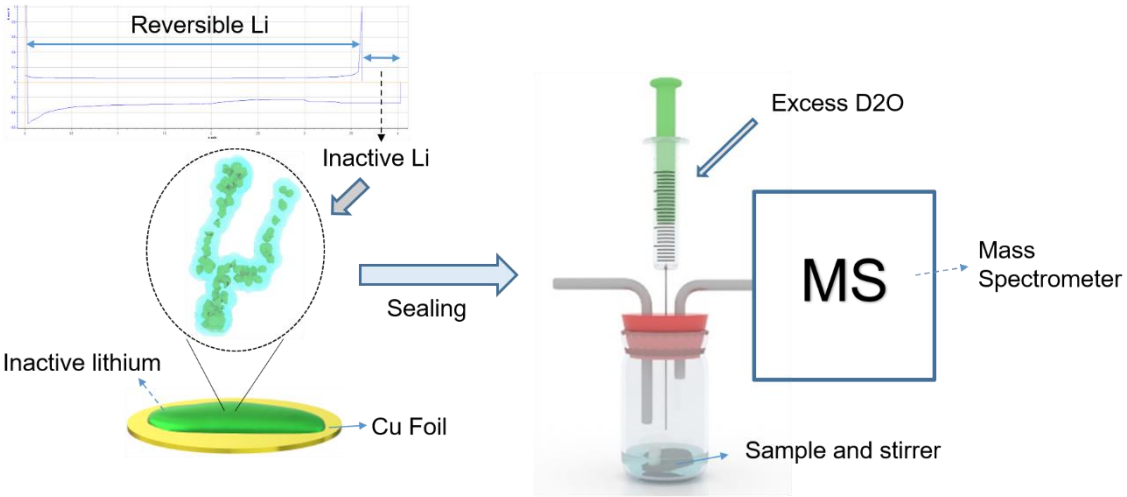


Figure 3.6. The illustration of a lab-made online mass spectrometer setup. This method is based on the DEMS system but uses a sealed titration setup instead of the in-situ coin cell.

Taking lithium metal battery titration analysis as an example. First, the cycled Li||Cu coin cell was disassembled in an argon glovebox. Then the copper foil and the glass fiber separators on the Cu side were transferred into a well-sealed vial (along with a magnetic stirrer) without further treatment. After the vial was connected to the MS, the gas composition inside the vial was analyzed and recorded. When the gas content was stable (checking no D_2, O_2, CO_2, and almost 100% Ar carrier gas), excess degassed D_2O (⩾99.96 atom % D, Sigma-Aldrich) was injected into the vial. Then the released D_2, HD, and CO_2 were detected by MS (Prima BT, Thermo Fisher Scientific). Finally, the quantity of metallic Li, LiH, and some organic SEI species from the cycling was calculated from the amount of D_2, HD, and CO_2 gas detected by MS, according to the following chemical reactions[21]:

$$(1)\ 2Li + 2D_2O = 2LiOD + D_2\uparrow$$

$$(2)\ LiH + D_2O = LiOD + HD\uparrow;$$

$$(3)\ 2LiOCO_2R + D_2O = Li_2CO_3 + 2ROD + CO_2\uparrow$$

(4) $(CH_2OCO_2Li)_2 + D_2O = Li_2CO_3 + (CH_2OD)_2 + CO_2 \uparrow$

The carrier gas flow rate (r) is controlled at 1 mL min^{-1} by a digital flow meter (Bronkhorst), so the total amount n in moles of the target gas (e.g., D_2, HD) can be calculated by the following equation:

$$n = \int \frac{r \times P}{V_m} dt$$

Here, V_m is the molar volume of gas (24.79 L mol^{-1} at 25 °C), and P is the percentage of the target gas in the carrier gas stream.

The reason why used the isotopic labeling method in this project is to distinguish between dead lithium and LiH. There has been a previous report on the quantitative titration method to measure dead lithium with titration H_2O.[21] However, if there is LiH formation in SEI, the method of titration of H_2O cannot get the accurate amount of dead lithium, because both lithium and LiH could react with H_2O and generate H_2. What is innovative about this isotopic labeling is that the LiH is quantificationally confirmed to exist in SEI components by measuring the formation of HD in the online-MS setup, with the help of titration of D_2O. Previously, the existence of LiH in SEI of lithium metal batteries was disputed. In addition, the amount of LiH could be also quantificationally measured in a series of cycled batteries using this online-MS method.

3.3.5 Nuclear Magnetic Resonance (NMR)

Nuclear Magnetic Resonance (NMR) is one of the most powerful tools for qualitative and quantitative analysis of the composition and structure of various organic and inorganic materials. Under an applied external magnetic field, the magnetic moments of the nucleus, which with a spin quantum number (I), can have $2(I)+1$ orientations. Each of these

orientations represents an energy state of the nucleus in the magnetic field. If a low energy state needs to transition to a high energy state, it has to absorb the energy of ΔE. In an external magnetic field, when the energy of radiation is precisely equal to the energy difference between the two spin nuclei in different orientations (corresponding to the resonance frequency), the spin nucleus in the low energy state absorbs electromagnetic radiation energy and transitions to the high energy state. At the same time, electrons can rotate and form a local magnetic field opposite the external magnetic field, thus reducing the resonance frequencies. In practical use, the nuclei have different chemical environments, leading to the difference in resonance frequencies used to characterize the composition of materials.

In this project, all-solid-state ^{7}Li magic angle spinning (MAS, υ_R = 10 kHz) nuclear magnetic resonance (NMR, υ_R = 155.5 MHz) experiments were completed at 9.45 T using a Bruker Avance III HD spectrometer and a 4 mm double air bearing probe. Due to the volatility of the samples, they were packed in dry HRMAS inserts inside an argon glovebox and spun using dry-nitrogen gas. The spectra were referenced to 1 M $LiCl_{(aq)}$ at δ_{iso} = 0 ppm.[187] The NMR is used to characterize the chemical environment of plated lithium in coin cells and the NMR-specific resonance peak shift verified the formation of LiH and LiF during Li plating.

3.3.6 Atomic force microscopy (AFM)

Atomic force microscopy (AFM) not only has a high resolution (lateral resolution up to 1nm, vertical resolution up to 0.01nm) but also has very low requirements on the working environment, sample properties, and other aspects. Therefore, AFM provides an effective method for researchers to learn about their materials. AFM has a sharp probe mounted on a cantilever sensitive to weak forces. When the tip is very close to the sample surface, a

weak force (attraction or repulsion) is generated between the tip and the sample, causing the microcantilever to deflect. The microcantilever can detect any force changes. During scanning, by controlling the constant force between tip and sample, the inter-atomic forces information can be represented by the microcantilever tip deflection. Through the photoelectric measuring system of microcantilever deflection scanning, the measured signal is amplified and converted to obtain atomic-level three-dimensional morphologies of the sample surface.

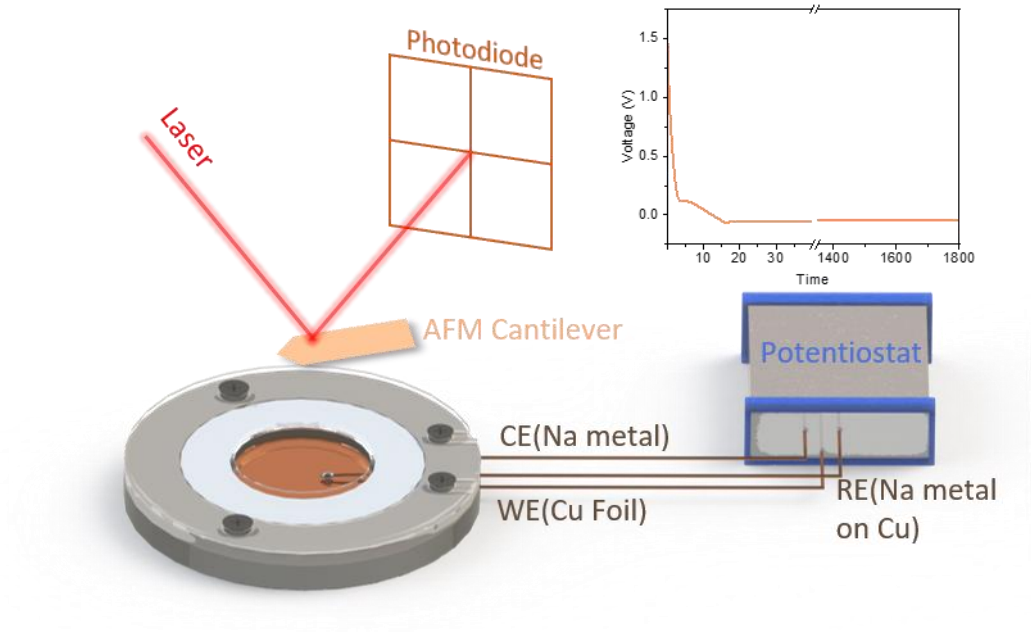


Figure 3.7. The illustration of the in-situ AFM setup used in this project. The working electrode is Cu foil, and the counter electrode and reference electrode are sodium metal. The whole setup is performed in the glovebox.

In this project, the AFM was used to characterize the surface morphology of deposited sodium and measure the SEI's mechanical properties. The Bruker Dimension Icon AFM was used to characterize both ex-situ and in-situ samples in the glovebox filled with argon (<0.1 ppm H_20, <0.1 ppm O_2). All AFM probes used were calibrated according to the

standard samples (Sapphire and Ti roughness sample from Bruker), interpolating the actual spring constant and the tip radius. The PeakForce QNM model was conducted to capture the topography of cycled electrodes corresponding to mechanical data. The 3D topography was reconstructed by NanoScope Analysis 2.0 software with calculated root-mean-square roughness values from at least three different regions. To get the real-time deposited sodium morphology to study the dynamic process of sodium deposition, the in-situ AFM setup is designed and it is shown in Figure 3.7. There is an open cell with three electrodes, which can hold electrolytes. The whole setup is in an Ar-filled glovebox, so the battery materials are well protected. The working electrode of the cell is Cu foil. Both the counter electrode and reference electrode are sodium metal. To obtain representative results, the battery materials used are consistent with the Na||Cu coin cell. During measurement, the morphology of the deposited specimen could be gotten in real-time with the corresponding electrochemical signals (such as galvanostatic plating/stripping or CV). Due to the AFM being very sensitive to surface topography changes of a specimen, thus the in-situ AFM setup is quite helpful to study the sodium growth process, such as the deposition order and dendrite growth.

3.3.7 Transmission electron microscopy (TEM)

TEM is a microscopy technique that characterizes the sample by analyzing transmitted electron beams of the thin specimen. According to Abbe's equation (Formula 3.4) in Chapter 3.3.1, the smaller the wavelength, the better the resolution. The wavelength of the electron beam has a relationship with acceleration voltage, which is shown below in Formula 3.5:[188]

$$\lambda = \frac{h}{\left[2m_0 eV\left(1+\frac{eV}{2m_0c^2}\right)\right]^{1/2}} \qquad (3.5)$$

Where λ is the wavelength, h is Planck's constant, m_0 is electron mass, e is the electron charge, V is acceleration voltage, and c is the speed of light in a vacuum. For example, the TEM used in this project is 300 kV, and the λ is approximately 1.97 pm. The acceleration voltage of SEM is around 30 kV. Therefore, the TEM could get much better resolution images (atomic level) compared to SEM. As shown in Figure 3.8, the construction of TEM is also more complex.

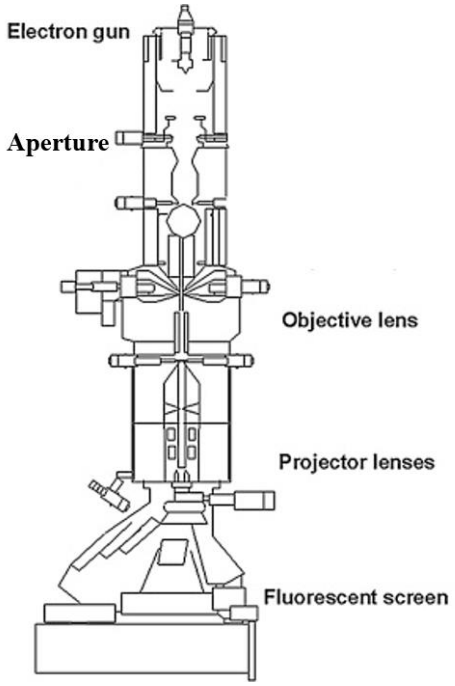


Figure 3.8. Illustration of the normal TEM structure. Reprinted with permission from Elsevier.[189] copyright 2017.

The electron beam is generated by an electron gun and is focused by apertures and an electromagnetic lens in the TEM vacuum column. The specimen is usually put between the objective lens and it has to be thin enough (within 100 nm) to make sure the electron beam is transmitted. After passing through the specimen, the transmitted electron beam is refocused and magnified by the objective lens, intermediate lens, and projector lens. Finally, the electron signals are converted into a visible form and form an image with information

about the specimen.

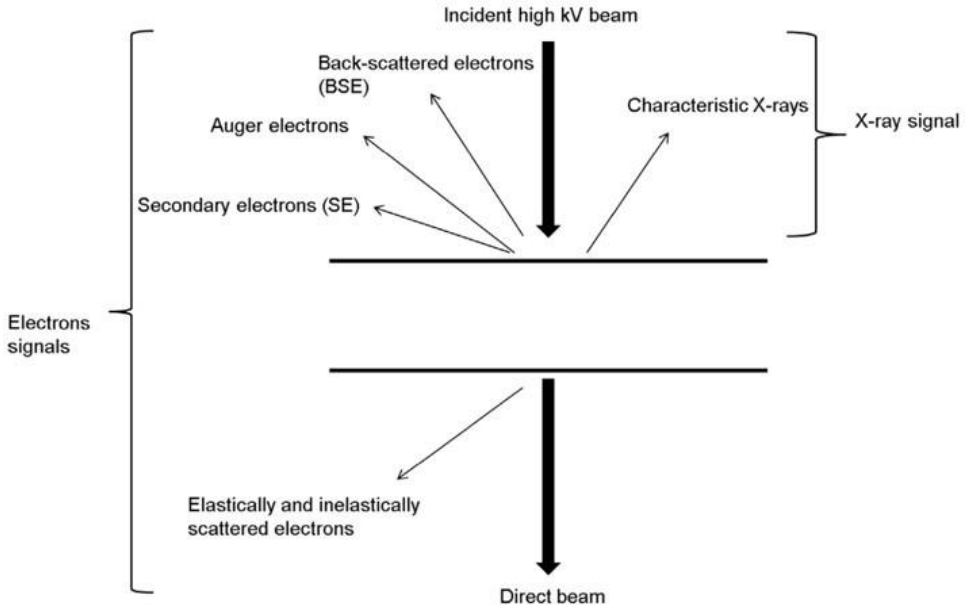


Figure 3.9. The sample is hit by a high energy electron beam and then produces several signals. Reprinted with permission from Elsevier.[189] copyright 2017.

The electrons have both wave and particle characteristics. For the particle property, the electrons can be controlled by Coulomb forces and scattered at a specific angle after collision with the specimen. As shown in Figure 3.9, when a thin specimen is transmitted through by a high energy electron beam (incident beam), several signals are then produced. The transmitted beam includes directly transmitted electrons, and elastically and inelastically scattered electrons, these are the main signals that form TEM images. For wave property, the scattered electrons could be diffracted and interfered. Based on these electrons' properties and corresponding microscopy control, the TEM can be effectively used to form high-resolution images and diffraction patterns of specimens.

TEM techniques usually include conventional transmission electron microscopy (CTEM), analytical electron microscopy (AEM), and scanning transmission electron microscopy

(STEM). The AEM is used to obtain composition information from a sample, which further includes energy-dispersive X-ray spectroscopy (EDS) and electron energy loss spectroscopy (EELS).

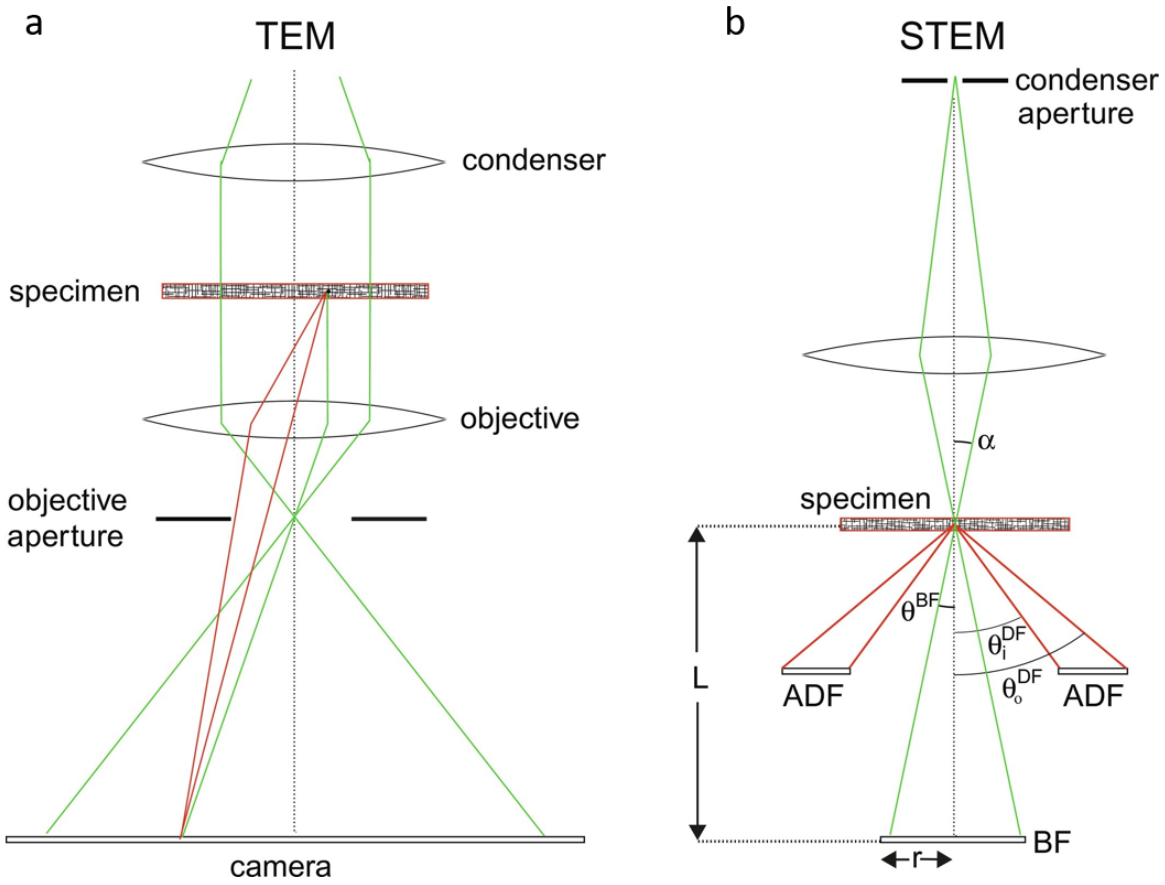


Figure 3.10. Schematics of TEM and STEM imaging modes. ADF is the annular dark field, BF is the bright field. L is camera length. Reprinted with permission from Elsevier,[190] copyright 2019.

In TEM mode, the specimen is usually transmitted by a parallel beam as shown in Figure 3.10a. The transmitted beam is then dispersed by an objective lens, magnified by the intermediate lens and projector lens, and forms an image on the camera. Therefore, TEM is widely used to directly look at the morphology and structures of a specimen. Especially, high-resolution transmission electron microscopy (HRTEM) can be used to characterize the crystal lattice structure of specimens on a nanometer scale. In this project, only the low-

mag TEM was used in in-situ liquid cell experiments because we focused on studying the dynamic evolution of the lithium/sodium plating and stripping process, while not the detailed lithium lattice structure. The large field of view in low-mag could observe several lithium dendrites simultaneously, which helps get representative data. A JEOL 3000F was performed in the TEM experiments.

3.3.8 Scanning transmission electron microscopy (STEM)

In STEM mode, the electron beam is focused to a sub-Angstrom probe and raster-scanned across the specimen as shown in Figure 3.10b. The magnification of STEM is controlled by the scan dimensions of the probe. Based on collecting different angular ranges of scattering electrons, the STEM images further include bright field (BF) STEM, annular bright field (ABF) STEM, annular dark field (ADF) STEM, and high-angle annular dark field (HAADF) STEM. In HAADF STEM mode, the high-angle annular detector collects fully incoherent electrons and avoids coherent signals. Due to the higher charge numbers of nuclei the more deflection of incoherent electrons, the HAADF STEM is Z-contrast and the intensity of the image is highly related to the atomic number.[191] The Z-contrast helps distinguish between generated objects. Therefore, the HAADF STEM mode is usually the first choice in liquid cell experiments to characterize the interface evolution during lithium/sodium plating and stripping.

In this project, the HAADF STEM imaging was performed with a JEOL 3000F (300 kV) using a 50-micron condenser aperture. The reason why 300 kV is chosen over 200 kV is that there are more interactions between the electron beam and specimen atoms at low electron accelerating voltage, which forms more secondary electrons. According to Chapter 2.3, radiolysis is the main beam effect in in-situ liquid cell TEM experiments, so 300 kV is a good choice. That's also why SEM is rarely used in in-situ liquid cell experiments. The

STEM beam current was calibrated by a Faraday cup (10 pA). All of the images in this STEM experiment were recorded with a pixel dwell time of 3 μs/pixel and at 512×512 pixels (calculated pixel size of 1.2×10^4 Å^2). These imaging conditions correspond to a radiation dose of $\sim 1.6 \times 10^{-2}$ e$^-$ Å^{-2}.

As discussed above, the HAADF STEM is Z-contrast which could supply better contrast to distinguish the generated objects during reactions compared to low-mag TEM (thickness contrast). In addition, the STEM could get better electron dose control, while TEM is shining everywhere, and hard to control the electron dose. The electron beam damage is dependent on electron dose, so the HAADF STEM is usually more useful in liquid cell experiments for battery study. In the lithium project, all the liquid cell experiments were studied in HAADF STEM mode. However, the JEOL 3000F TEM machine is broken during the sodium project and the HAADF STEM does not work anymore. Therefore, some liquid cell experiments of the sodium project in Chapter 5 are studied based on the TEM mode.

3.3.9 In-situ sealed liquid S/TEM

The in-situ sealed liquid S/TEM allows us to make a micro-sized battery inside the TEM by using a specially designed sealed liquid cell holder. During the experiment, the liquid electrolyte can flow into the battery, and a Gamry potentiostat can apply electrochemical signals. The two microchips have two thin windows to ensure the electrons pass through. Therefore, the operando electrochemical reactions can be observed by TEM. In this project, the in-situ TEM is performed by a Protochips Poseidon 510 holder, and the operando lithium/sodium plating/stripping process along with side reactions are studied under TEM and STEM mode.

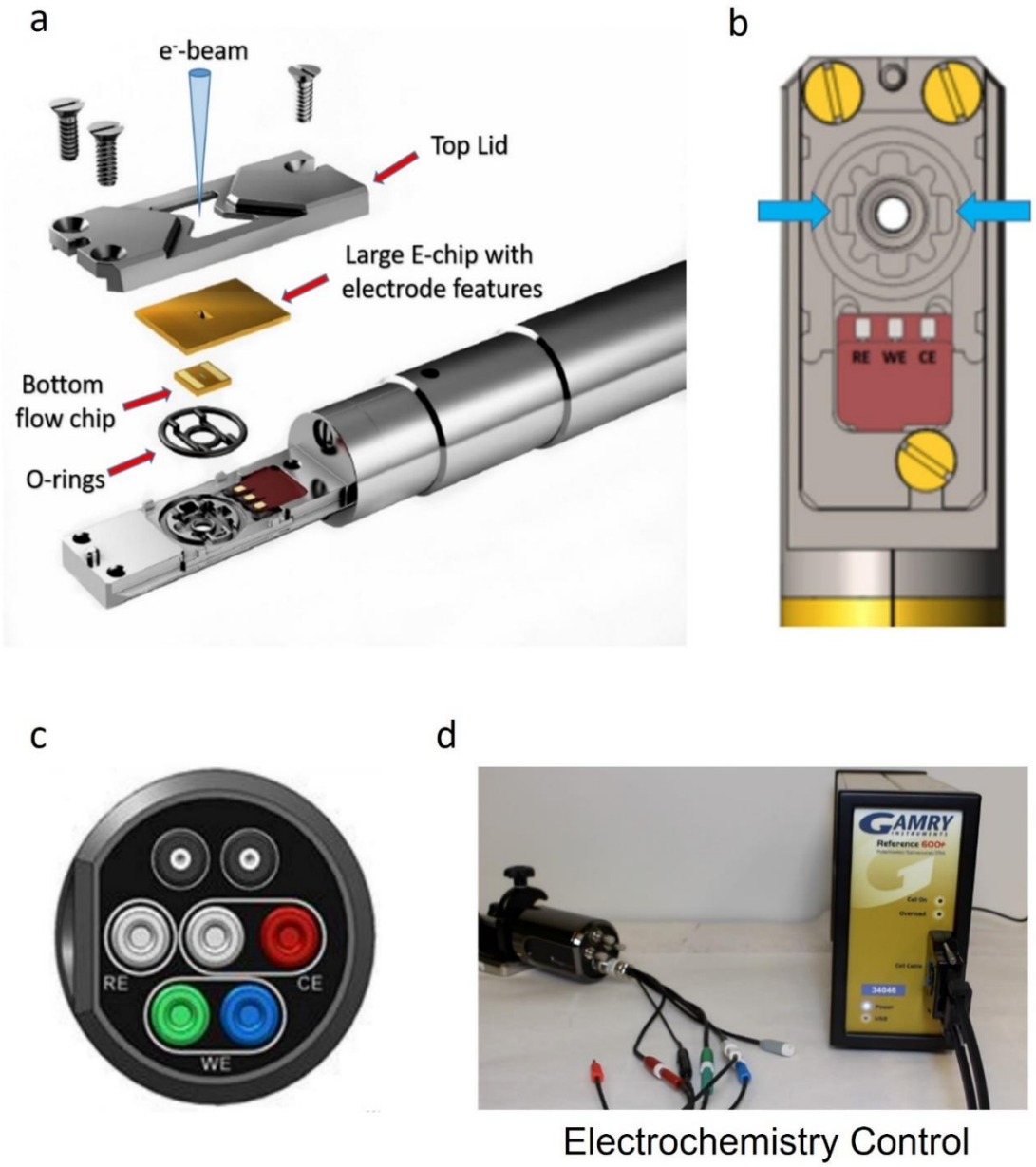


Figure 3.11. Schematics of in-situ sealed liquid TEM holder (from Protochips Poseidon). The TEM holder provides a sealed capacity for liquid electrolytes, and the windows in microchips ensure the electrons pass through. (a) the structure of a micron-sized battery at the tip of the holder. Reprinted by permission from Springer Nature[192], copyright 2020. (b) Blue arrows point at the liquid inlet and outlet. (c) the channels of the holder. The two black channels are where liquid flows in and out. The white, red, blue, and green channels are for the working electrode, counter electrode, and reference electrode. (d) The electrode channels of the holder are connected with a Gamry to apply electrochemical signals.

As shown in Figure 3.11a, the micro-sized battery comprises two microchips (bottom flow chip and large E-chip with electrode features), a gasket seal (O-rings), and electrical biasing

contacts on the holder. During the experiment, the electrolyte could be flown into the encapsulated liquid-cell TEM set-up from the two black channels of the holder (as shown in Figure 3.11c), with the help of a syringe pump.[193] Then, a fresh thin layer of electrolyte could be confined between the two chips inside the TEM vacuum column. A Gamry (as shown in Figure 3.11d) can connect with the electrode channels of the holder (as shown in Figure 3.11c) and apply with electrochemical signals.

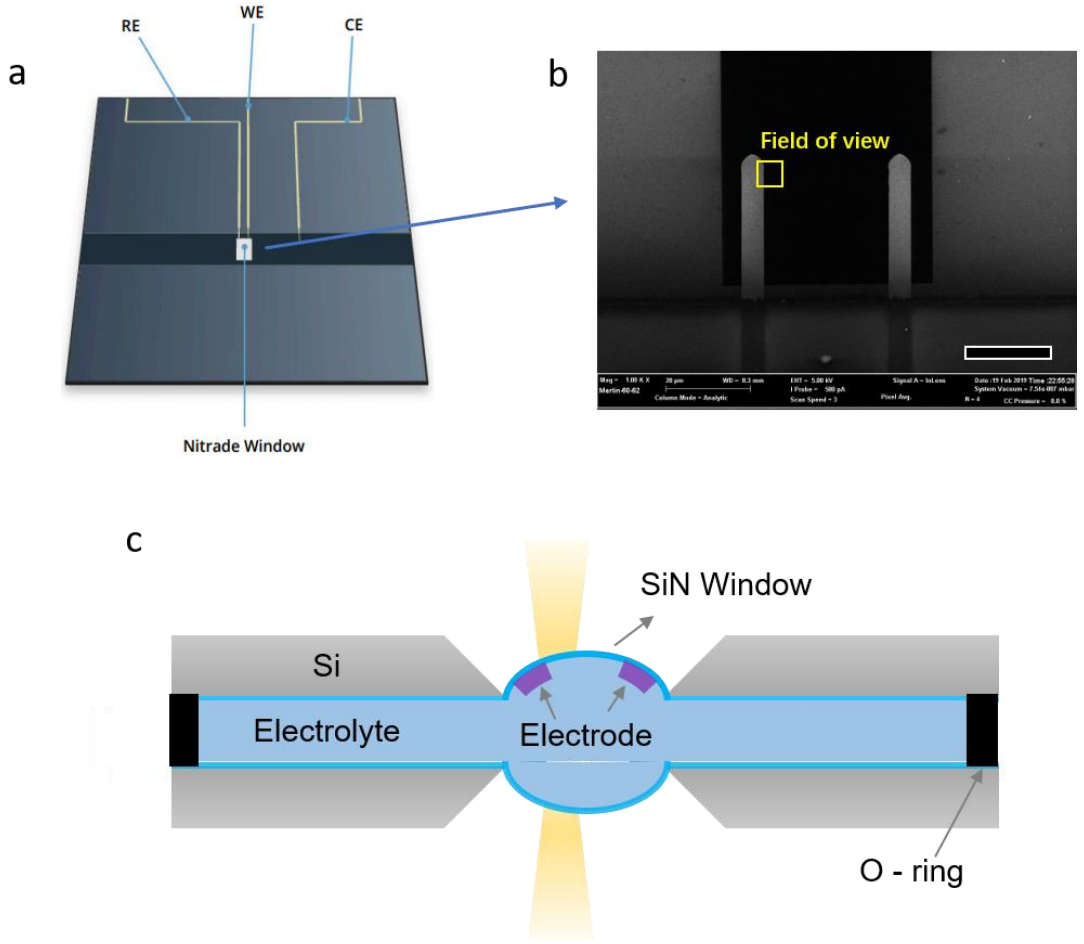


Figure 3.12. Schematics of liquid TEM cell. (a) The large chip, has a working electrode (WE), reference electrode (RE), and counter electrode (CE) on it. (b) SEM image of SiN window in the large chip, which has WE and RE on the window. The electrodes are made of platinum (Pt). Scale bars are 20 µm. (c) Schematic of micro-sized battery (side view). The structure of two chips and O-rings provides a sealed capacity for liquid electrolytes. The thickness of electrolyte between two SiN membranes is around a few micrometers, which is required to be thin enough to allow an electron beam to penetrate through.

The large chip has a working electrode (WE), reference electrode (RE), and counter electrode (CE) on it, and the electrodes are made of platinum (as shown in Figure 3.12a). There is a SiN membrane in the large chip and it is around 50 nm thick. The WE and RE could be observed from the window. In liquid cell experiments, the field of view is usually at the side of WE to study the lithium plating/stripping process. The side-view schematic of liquid cell TEM is illustrated in Figure 3.12c, the WE and RE electrodes are immersed in electrolyte. The spacer thickness between the two silicon chips is around 510 nm in this project. The electrolyte thickness between the two SiN membranes is usually a few micrometers due to the outward bowing of the SiN membranes, which is also thin enough to allow an electron beam to penetrate through. The outward bowing of SiN membranes is because of the external vacuum environment of the TEM column. The window bowing level is relative to the width of the window. According to the Poseidon 510 holder user manual, the window bowing of the 50 nm thick thin SiN membrane with a width of 50 microns should be around 2 μm. Thus, the outward bowing of the membrane effectively increases the thickness of the liquid layer and degrades resolution.

It is important to note that there is continuous electrolyte flow in the liquid-cell system, which would not be present in a real battery. For example, in a real lithium metal battery, the lithium ions are supplied from the lithium metal anode, and the concentration gradient of lithium ions in the electrolyte always keeps stable. However, in the closed liquid-cell system in this project, all of the WE, RE, and CE are made of platinum. There is no other source of lithium ions other than electrolytes. The lithium ions in the electrolyte are continuously consumed during lithium plating/stripping. Therefore, to continuously supply lithium ions to maintain the lithium-ion balance in the electrolyte, continuous fresh electrolyte flow is required. In addition, continuous electrolyte flow has several advantages.

The liquid flow can decrease the electron beam heating effects and mitigate the beam damage byproducts in an electrolyte. The continuous electrolyte flow helps the liquid cell to approximate the static concentration gradient of lithium ions in the electrolyte that getting in a normal battery, as the depleted electrolyte is continually replenished with fresh electrolyte. Also, because of the continuous electrolyte flow, there is no need to worry about the electrolyte leaking or evaporating and leaving behind salts to clog the fine tubes during experiments. The diameter of the peek tubes is around 100 μm, so it is easy to be clogged by salts or byproducts. Thus, it is necessary to keep the electrolyte flow during studying the battery cycling process. As shown in Figure 3.11b, the blue arrows point at the liquid inlet and outlet. Combined with the side-view of the liquid cell in Figure 3.12b and Figure 3.12c, we can learn that the direction of liquid flow is perpendicular to the direction of electrodes and all the three electrodes are immersed in electrolyte. To minimize the window bowing during the experiment by lowering the pressure inside the liquid cell (as discussed above, the lower window bowing means the cell is not as thick, and so the resolution should be higher), a slow flow rate (120 μl h^{-1}) is chosen during lithium plating/stripping, which is consistent with the previous study.[169] The direction of liquid flow should not affect the morphology of deposited lithium because we got the same results in different flow directions (either from the WE to the CE or from the CE to the WE). Although the in-situ experiments cannot simulate a hundred percent of real situations, the real-time study still has significant values.

In the lithium project, when the entire liquid cell holder is assembled and inserted into the TEM column, dried DMC would flow for 40 minutes first with a 240 μl h^{-1} flow rate before introducing electrolyte. This action is to expel air because the holder is assembled in an atmospheric environment. Then, the electrolyte is flowed into the holder for 40 minutes with a 240 μl h^{-1} flow rate to ensure the electrolyte fills the holder. A Gamry Reference 600

was used to provide and measure the cyclic voltammogram signal between the reference, working and counter Pt electrodes patterned on the chip. During in-situ experiments, the electrolyte flow rate is changed to 120 µl h^{-1} to minimize the impact on the plating/stripping process. Between each cycle, the electrolyte has flowed for 30 minutes with a 240 µl h^{-1} flow rate to refresh the electrolyte, and the beam is blanked to prevent beam damage. All the electrolyte preparation was performed in an argon glovebox or sealed system. Cyclic voltammetry was performed at a scan rate of 20 mV s^{-1}, between 0 V, and -4 V, and returning to 0 V. In the sodium project, the dried DME solvent is flowed into the holder instead of DMC.

Chapter 4. Revealing the role of fluoride-rich battery electrode interphases by Operando Transmission Electron Microscopy

4.1 Introduction

The lithium anode is believed to be the ideal negative electrode for lithium-based rechargeable batteries.[15,194] However, the relationship between SEI and the dynamic processes of lithium dendrite growth and dissolution is required to better understand.

Multiple methods of SEI modification have demonstrated improved lithium battery performance, such as employing a fluoride-rich electrolyte,[149,195,196] increasing the electrolyte salt concentration,[197,198] pre-constructing an artificial SEI,[199–201] and tailoring the electrolyte with additives[69,73,202]. Across these different approaches, it has been shown that the generation of a fluoride-rich SEI is a consistent factor in achieving improvements to coulombic efficiency.[203] This fluoride-rich interphase drastically reduces the formation of detached, electrically isolated 'dead lithium' and thus inhibits a major cause of efficiency loss.[21,204]

To build a clearer understanding of the link between the morphology of deposited lithium, its preference for forming dead lithium on dissolution, and the overarching role of SEI composition, here operando liquid-cell STEM (LC-STEM) is used to directly image lithium plating and stripping across fluoride-poor and fluoride-rich interphases. The direct observations reveal that the fluoride-rich SEI promotes a uniform lithium deposition. These uniform structures are more easily stripped than the dendritic morphologies deposited across the fluoride-poor SEI and leave behind significantly less dead lithium. In addition, online-MS, NMR, and SIMS are also performed and they provide additional insights into the composition of the SEI and the sources of lithium loss in the two systems. These

findings on the relationship between SEI composition, lithium structural evolution, and the loss of lithium, give a comprehensive understanding of the degradation mechanisms of lithium metal batteries.

4.2 Results

4.2.1 In-situ liquid STEM characterization

To reveal the role of fluoride-rich electrode interphases in lithium metal batteries, the LP30 with and without FEC additive electrolytes were chosen as my model system.[205] Due to FEC is widely believed to promote the formation of fluoride-rich interphase with carbonate solvent lithium electrolytes.[73] More sample details are introduced in Chapter 3.1. The real-time investigation of lithium plating/stripping was carried out under CV electrochemical signals in an electrochemical closed liquid-cell (Protochips Poseidon 510 holder). The HAADF-STEM mode was used to image the structural dynamics. In HAADF-STEM images, the lightest/least dense/thinnest materials appear dark. The density of lithium is 0.53 g $cm^{-3,}$ which is the only solid material more lightweight than the electrolyte. The density of a gas, such as air, is much lower than lithium metal. Therefore, the bubble is expected to be darker than lithium.[169] All LC-STEM experiments were performed at low dose rates and under a high accelerating voltage (300 kV), minimizing beam damage by radiolysis.[206,207]

The beam was blanked between experiments. A control experiment monitoring the effect of a comparable electron beam dose was performed on the electrolyte (as shown in Figure 4.1), showing no observable breakdown products from the electron beam in 400s. This indicated that the effects of electron beam were acceptable here because all the in-situ liquid cell experiments in this project were finished within 400s.

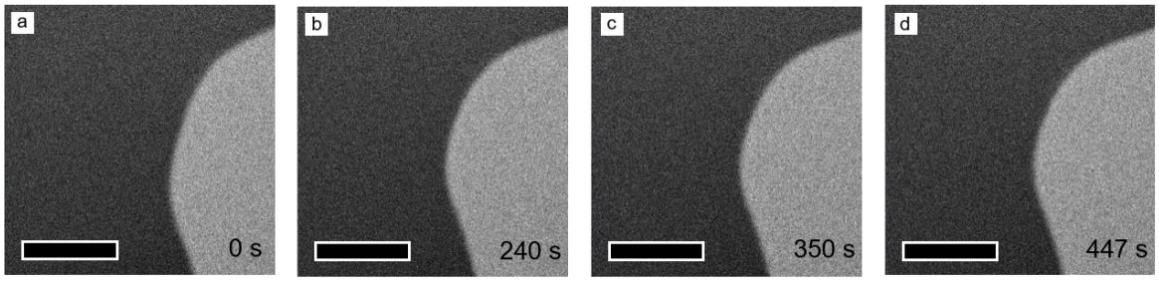


Figure 4.1. A control experiment testing the beam effect in HAADF STEM experiments. This is performed under the same conditions as the cycling experiments, except with no external bias applied to the working electrode. STEM imaging an area of LP30 electrolyte for 0s (a), 240s (b), 350s (c), 447s (d). There is no clear observable difference within 447s, suggesting the electron beam dose should be acceptable within our experiment duration (within 400s). Scale bars are 2 μm.

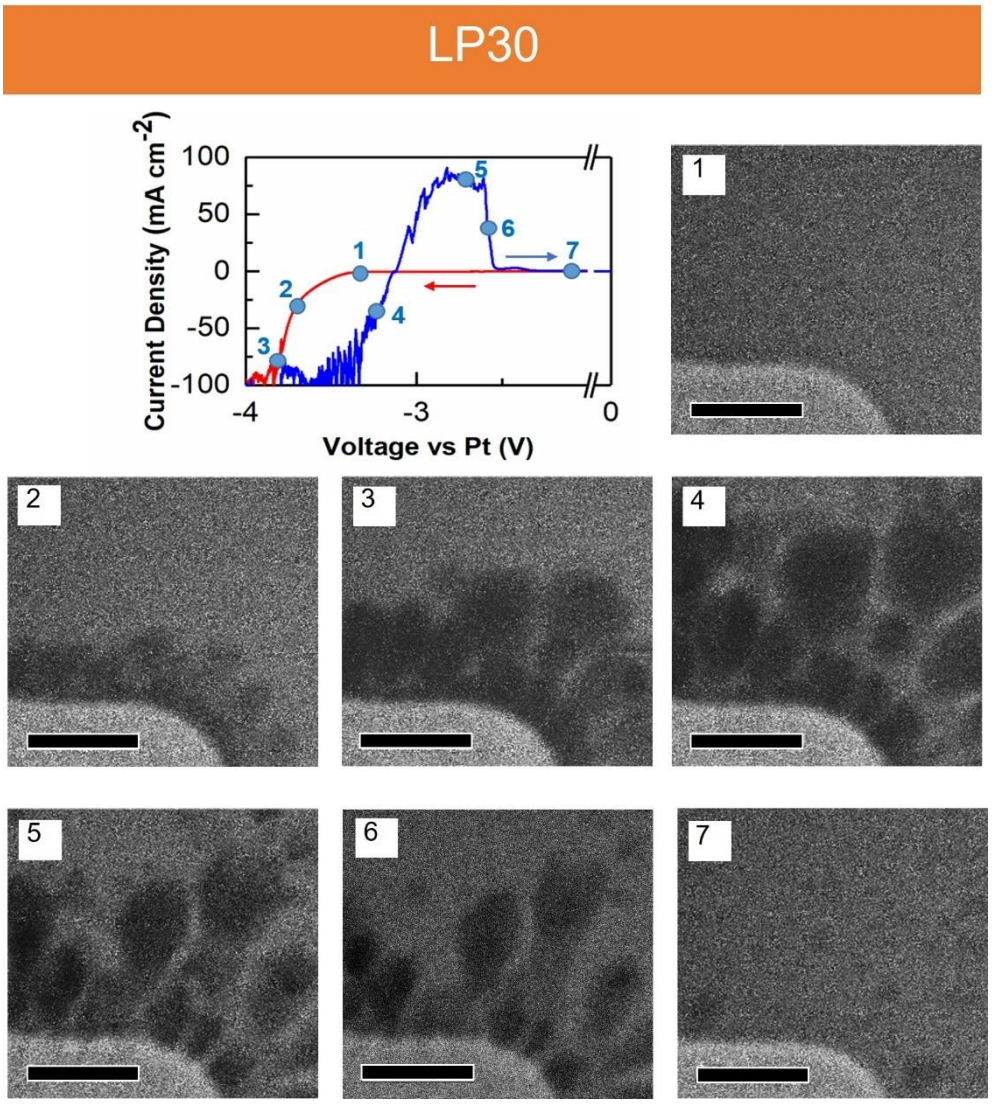


Figure 4.2. In-situ liquid-cell HAADF-STEM images showing the first cycle of lithium plating/stripping in LP30 electrolyte with the corresponding CV. Image panel numbers correspond to their respective positions on the CV plots. Scale bars are 2 μm.

As illustrated in Figure 4.2, the lithium plating/stripping process in standard LP30 electrolyte was captured by HAADF-STEM images with the corresponding CV. In the CV, the plating process is shown by the red line, and the stripping process is shown by the blue line. At first, no lithium was observed from 0 V to -3.4 V vs Pt (Figure 4.2, panel 1). As the voltage gradually decreases, lithium deposits (black particles) initially nucleated at the edge of the platinum working electrode (WE). They then grew rapidly, forming micron-sized lithium grains with poor inter-grain connectivity (Figure 4.2, panels 2-4). As the plating process continued, the focus of lithium deposition moved to the tips, forming larger separated grains (Figure 4.2, panels 3-4). Further increasing the potential from -3.1 V led to stripping (Figure 4.2, panels 5-7), and the plated lithium grains steadily reduced in size, dissolving from the roots and tips. Finally, a small number of lithium particles detached from the Pt electrode and thus became electrically insulated. These lithium particles were no longer involved in the cell electrochemistry, leading to an overall efficiency loss. In this project, these electrically insulated lithium particles were called dead lithium.

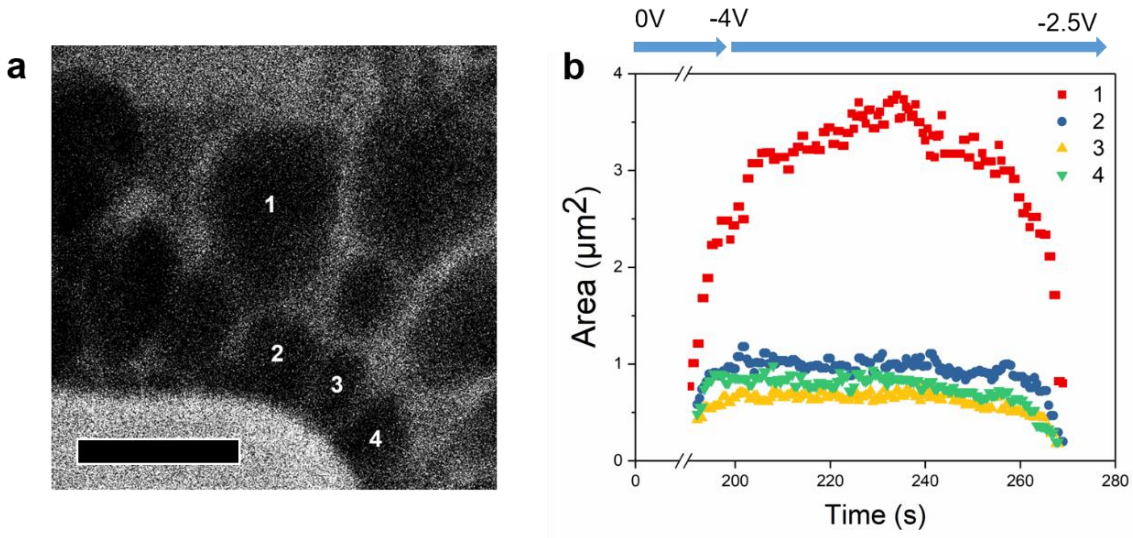


Figure 4.3. Analysing lithium grains size evolution during lithium plating/stripping in LP30 electrolyte. (a) The grains were analyzed. (b) The corresponding size evolution across the plating/stripping process. It shows that lithium grows more from the tip as the plating continues. The scale bar is 2 μm.

To analyze the growth rate of lithium grains during lithium plating/stripping, the size of four specific lithium particles was measured (as shown in Figure 4.3a). The corresponding evolution size of these four lithium particles were shown in Figure 4.3b, and it illustrated that denser root growth dominates the initial stages, while then the lithium was mainly deposited at the tip. This may attribute to the result of the redistribution of the electric field after lithium is deposited.[208] During the stripping process, the size changes of lithium particles at the tip were also more pronounced. It also indicated that although the deposited lithium particles seemed a little bit scattered, they were still pretty well connected.

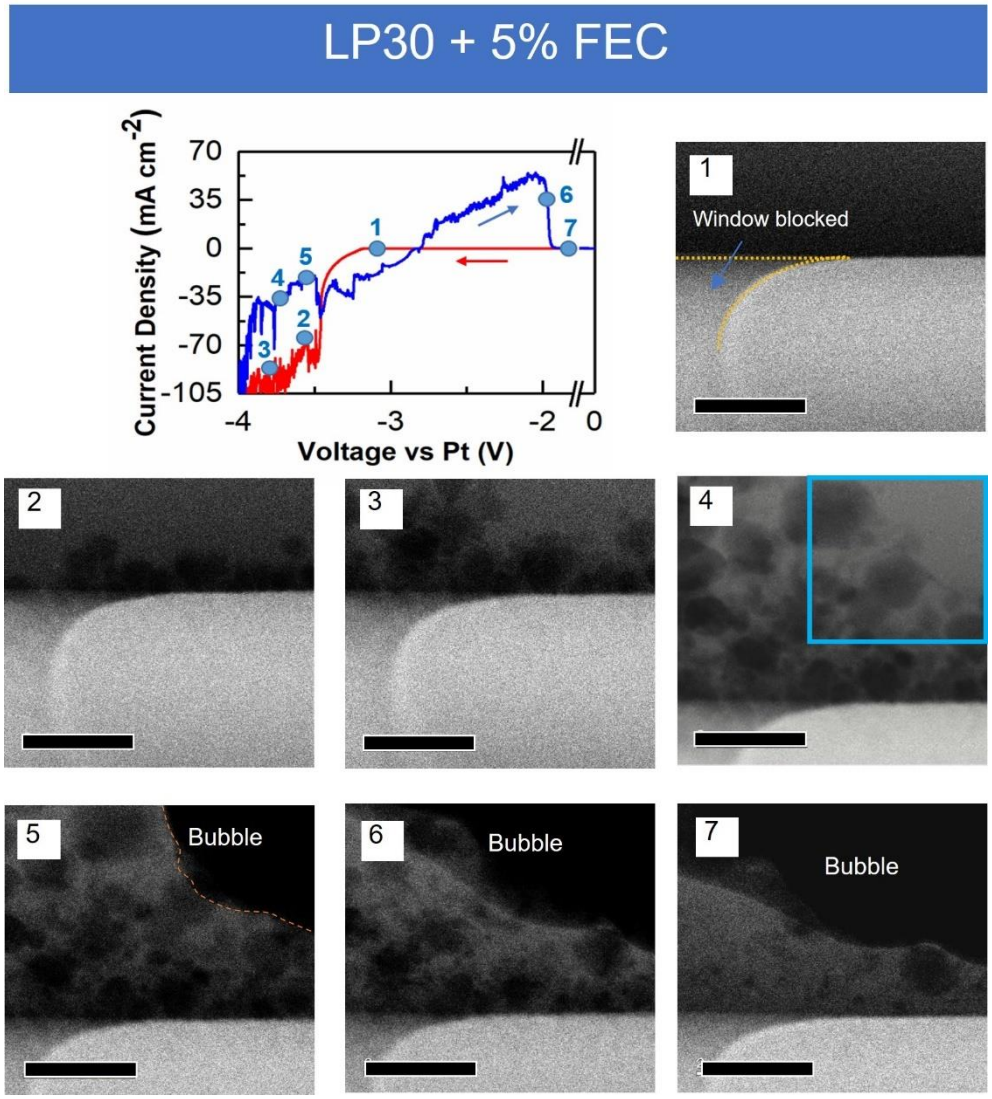


Figure 4.4. In-situ liquid-cell HAADF-STEM images showing the first cycle of lithium plating/stripping in LP30 with 5% FEC additive with corresponding CV. Image panel numbers correspond to their respective positions on the CV plots. Scale bars are 2 µm.

Identical experimental parameters were carried out to compare the LP30 with 5% FEC additive electrolyte on the first lithium plating/stripping cycle. Its plating process was shown in Figure 4.4, panels 2-5 and its stripping process was shown in Figure 4.4, panels 6-7. Both processes resembled the ones we observed within the LP30 system without the additive, in terms of both lithium morphology and electrochemistry (CV curves). The deposited lithium were coarse micron-sized grains with poor interconnectivity, and subsequent stripping similarly left behind a few dead lithium deposits. The coulombic efficiency in these two electrolyte systems under LC-STEM experiments was also similar. The Pt electrode in Figure 4.4 was partly obscured by the liquid-cell Si chip edge and the schematics were illustrated in Figure 4.5.

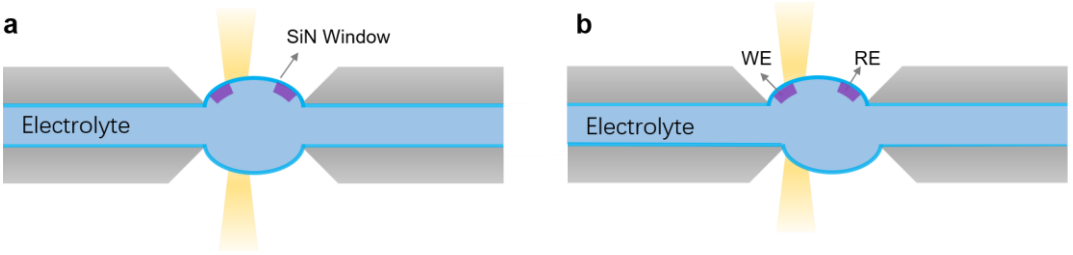


Figure 4.5. Schematics of the liquid cell in STEM. (a) In a normal situation, the SiN windows bend due to the vacuum of the TEM chamber. (b) The bottom Si chip is not perfectly aligned with the top Si chip, so a part of the upper Si blocks the observation of some of the working electrodes (WE). While this misalignment of chips can reduce the thickness of the liquid through which the electron beam penetrates, and improve the resolution.

This difference arose from the misalignment during the cell assembly process. As shown in Figure 4.5a, the two SiN chips should be aligned in a normal situation, and the entire electrodes were exposed to view. When the two SiN chips were misaligned, the view of part of the electrode would be blocked as shown in Figure 4.5b. However, this misalignment also could bring a surprise in certain situations. As discussed in Chapter 3.3.9, the outward

window bowing of the membrane could effectively increase the thickness of the liquid layer and degrade the resolution. To some extent, the misalignment of chips could reduce the thickness of the liquid through which the electron beam penetrates. Thus, it offered the opportunity to see the structure dynamics more clearly. In this project, the working electrode was partly obscured by the Si chip accidentally, while all of the electrodes were still immersed in electrolyte, it would not affect the normal plating/stripping behavior of lithium. By contrast, this unexpected misalignment gave us a chance to study the electrode interphase in a higher resolution.

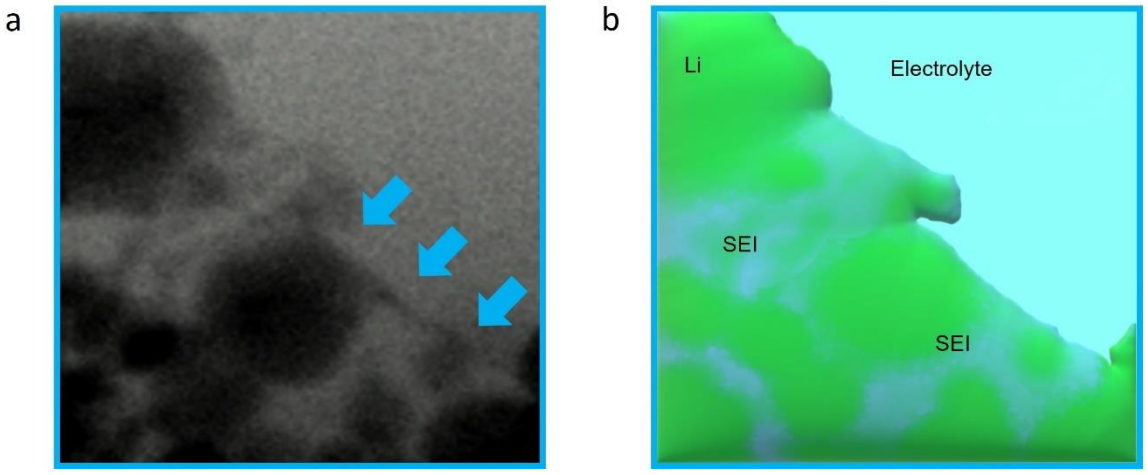


Figure 4.6. The interphase of deposited lithium in LP30 with 5% FEC additive electrolyte. (a) The magnified blue box from Figure 4.4, panel 4, shows the interphase morphology of deposition lithium. (b) An accompanying graphic to aid interpretation.

The interphase of deposited lithium was specially studied in Figure 4.6, which was a magnified blue box from Figure 4.4, panel 4. As introduced above, the black particles were deposited lithium in HAADF-STEM images and the blank space in the upper right corner was electrolyte. Unlike the interface images of deposited lithium in the LP30 experiment, there is a clear line between lithium and electrolyte, which is pointed out by the blue arrows

in Figure 4.6a. As we know, once the lithium meets the electrolyte, there will be SEI formed immediately which surrounded the lithium.[22] Thus, a reasonable guess was that the lower-contrast layer which surrounded black lithium grains was SEI, and the line was the boundary of the SEI. In order to better illustrate the boundary interphase structure of the deposited lithium, a corresponding cartoon was shown in Figure 4.6b.

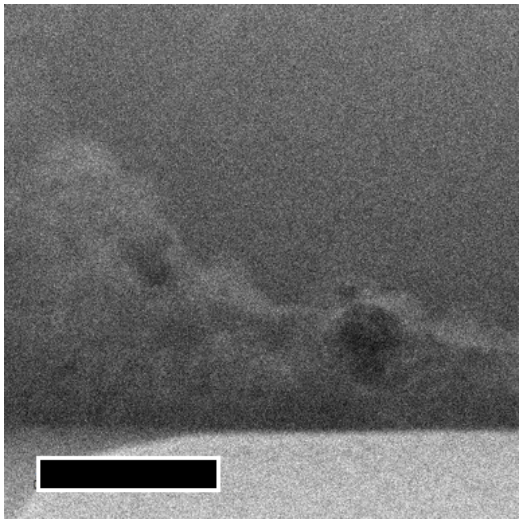


Figure 4.7. The working electrode image after the first cycle in LP30 with 5% FEC additive electrolyte experiment. There is fresh electrolyte flowing for 20 minutes to refresh the cell without any electrochemical signals and electron beam. Finally, it still ends up with a film between the electrode and the electrolyte.

After the first cycle, the electrolyte continuously flowed for 20 minutes to refresh the liquid cell. There is an obvious stable film left between the electrode and the electrolyte, which has to be the SEI film (as shown in Figure 4.7). The boundary is similar to the line in Figure 4.6a, which further verification that the boundary is formed by SEI. Most of the film has brighter contrast compared to the electrolyte, which illustrates the SEI has a higher density than the electrolyte. The black particles covered in SEI are dead lithium. To see the detail of the SEI layer, the averaging frames of STEM images, which were captured from the in-situ STEM video, were performed in Figure 4.8. The averaging method improved the

signal-to-noise ratio (SNR) significantly and showed the SEI layer edge clearly (as shown in Figure 4.8c). Capturing any SEI layer is challenging by conventional ex-situ or post-mortem techniques, as cell dismantling and sample preparation can remove it.[19,209] Through high-resolution observation and direct video recording, direct imaging of the SEI becomes a reality through real-time STEM.

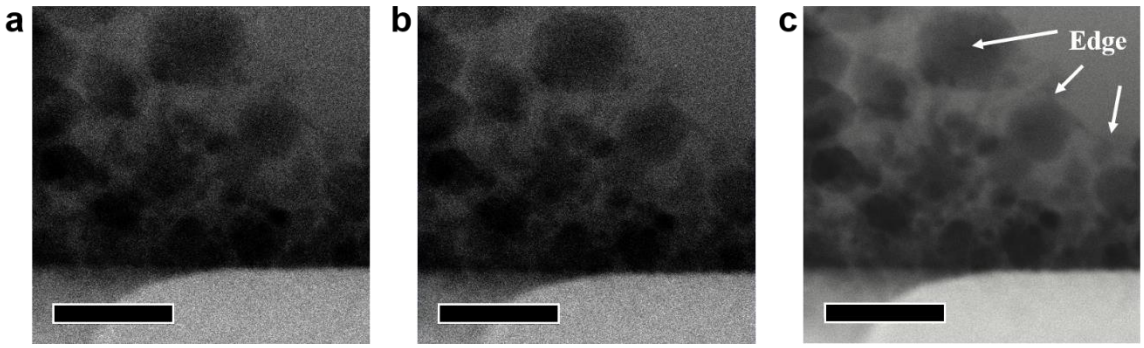


Figure 4.8. Averaging frames (394-418) from the 5% FEC plating/stripping video. As all the edges are from the end of the plating process, the dynamics are pretty static, so we can average the frames together to improve the signal-to-noise ratio (SNR). (a) the 394th frame, (b) the 418th frame, showing almost no drift compared to the 394th frame, and (c) stacking frames from 394-418. Scale bars are 2 μm.

Another marked difference between the two systems is the formation of a gas bubble in the 5% FEC experiment (Figure 4.4, panels 5-7). To rule out the electron beam effects, a control experiment is performed (as shown in Figure 4.9). A HAADF STEM image was acquired before applying any electrochemical signals in LP30 + 5% FEC electrolyte. It showed no bubbles (as shown in Figure 4.9a). Then, the electron beam is blocked and the CV signal is applied in the experiment (as shown in Figure 4.9b). After the CV scanning and opening electron beam, a bubble was observed like in the previous experiment (as shown in Figure 4.9c). This control experiment clearly shows that the observed bubble formation from FEC-containing electrolyte is not the result of the STEM electron beam but due to electrochemical side reactions, as it does not otherwise form. Therefore, this bubble

formation was not a result of beam-induced radiolysis gas products. Instead, it only occurred when a sufficient potential was applied, indicating that it was due to a gas-producing side-reaction. Side reactions are challenging to diagnose in any experiment, as they are complicated. However, significant works of literature have attempted this; the surface reactions of FEC on the anode could form gases, such as CO_2 and H_2[210,211].

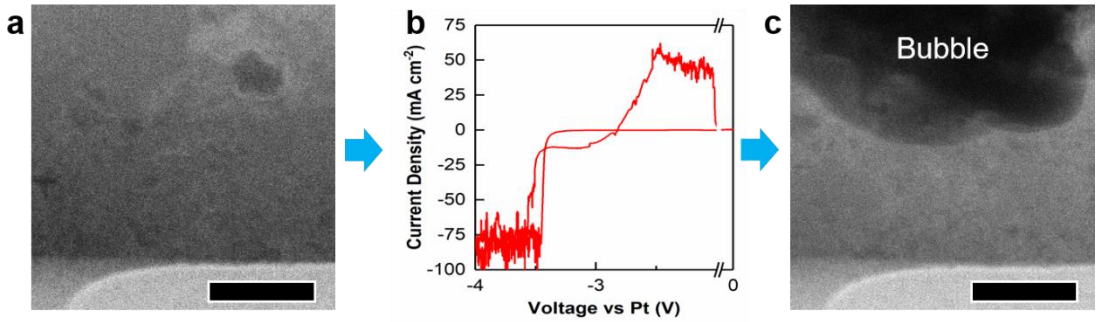


Figure 4.9. The control experiment shows that the STEM electron beam does not form the gas bubble. The whole CV cycle was performed while blocking the beam, using an LP30 + 5% FEC electrolyte. (a) Image acquired before applying a potential, showing no bubble. (b) Blocking the beam and scanning the same CV signal used in the experiment. (c) After finishing the CV signal, we opened the beam valve and acquired an image. The bubble was still observed, demonstrating it is independent of any beam effect. Scale bars are 2 µm.

As gas bubbles may affect the lithium plating/stripping behavior, it is essential to address the relevance and any potential impact of the presence a bubble may have on the electroplating and stripping of lithium in our LC-STEM experiments. Thus, a detailed discussion is made in the discussion part. The conclusion we draw from the analysis and discussion is that while the bubble can have an effect, based on the direct observation of a bubble's influence and by comparison of cycles with a bubble present, the dominant mechanism behind lithium plating and stripping morphology is the SEI.

To distinguish SEI, metallic Li, and bubbles in the STEM images, a method of combination of measuring the contrast/HAADF intensity of the structure and monitoring its behavior over time over the movie capture was used. In the liquid-cell set-up, all the electrodes,

plated Li, SEI, and bubbles are all immersed in the electrolyte. Combined with the contrast in the HAADF-STEM images and spatial distribution, we can distinguish the large bubble and the Li metal.

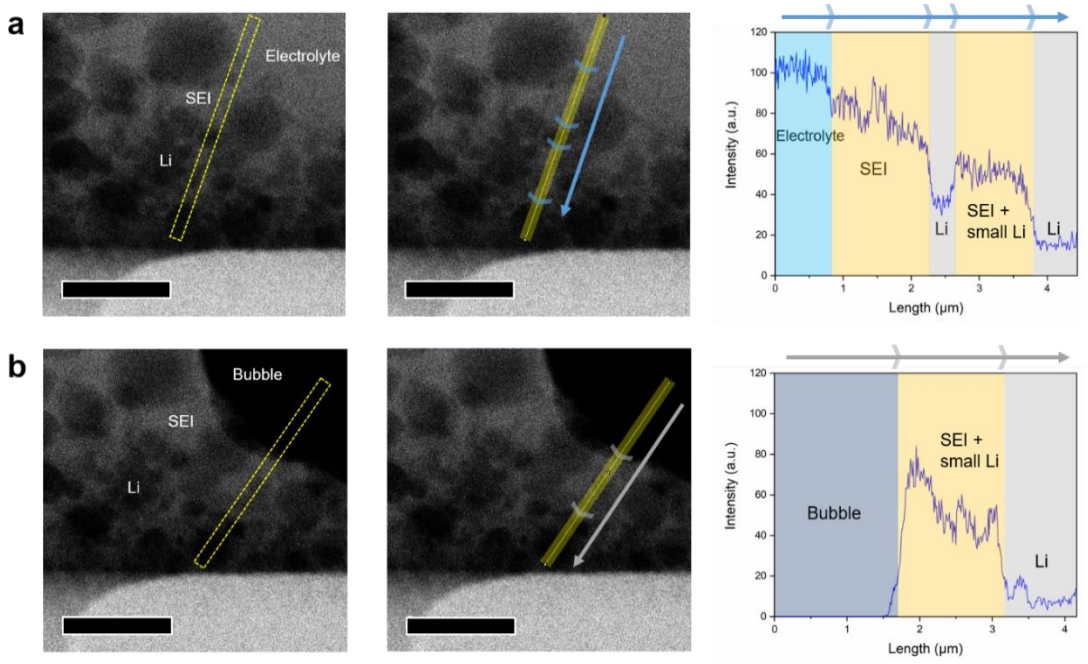


Figure 4.10. Box-averaged intensity line profiles extracted from the STEM-HAADF frames of Figure 4.4, panel 4, showing the relative contrast of various features. Line profile comparisons of the electrode tip (a) before and (b) after a gas bubble enters the field of view. The box-averaged profiles were extracted from the indicated areas, with chevrons denoting matching locations to aid comparison between the plots and images. The HAADF intensity is distinct for the various morphologies, with the SEI regions exhibiting a range of contrast dependent on the number of small lithium crystals dispersed within it. The extent of the dark contrast of the gas bubble is not fully captured by the contrast range set on the HAADF detector. Scale bars are 2 μm.

In order to clearly explain it, the contrast normalized work and illustration details were shown in Figure 4.10. In Figure 4.10a, the bubble is not appearing in the view of the window yet, the plated Li is covered by the SEI, and the outside is the electrolyte. From the normalized HAADF contrast, we can know that the SEI part shows lower intensity than electrolyte but higher than deposited Li. Some part of the SEI appears lower contrast because there is some small particle of Li distributed in it. In Figure 4.10b, the bubble

appears, and it presents the darkest, even the thickest plated Li has a clear higher contrast than the bubble. The intensity of the bubble shows zero just because it is the minimum contrast level to read, it reaches the contrast window of the HAADF detector. Thus, the HAADF-STEM images are able to distinguish the SEI, metallic lithium, and bubbles. However, the SEI layer in the LP30 experiment was not directly seen under the HAADF-STEM images in Figure 4.2. That is probably because the misalignment of Si chips in the FEC case reduces the thickness of the liquid and improves the resolution.

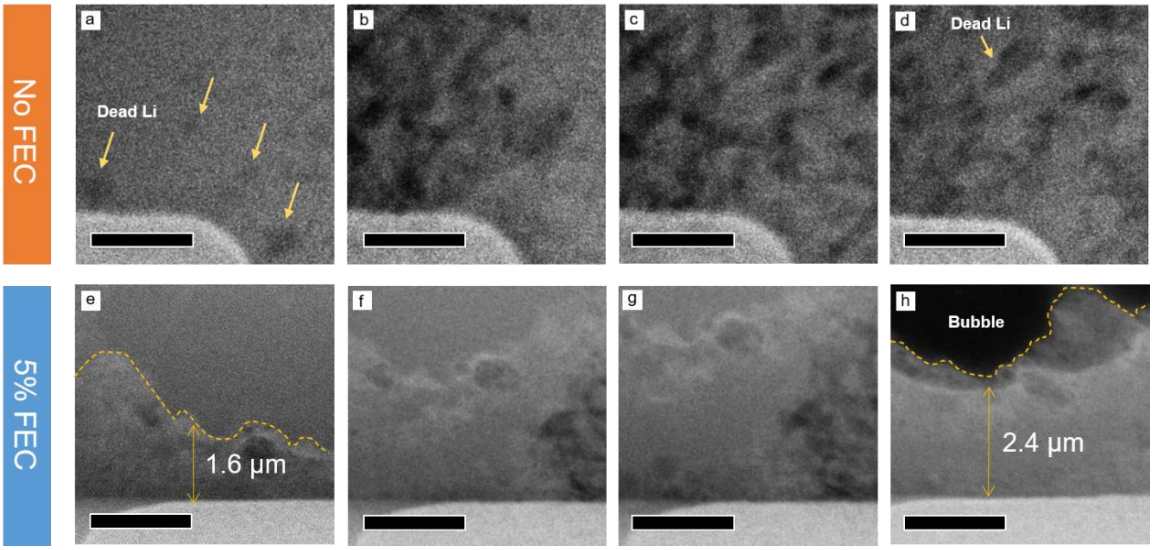


Figure 4.11. In-situ liquid-cell HAADF-STEM images showing the second lithium plating/stripping cycle from LP30 and LP30 + 5% FEC electrolytes. (a) Before plating, there is some dead lithium left in the previous cycle; (b) lithium starts plating; (c) more lithium is deposited; (d) at the end, some lithium loses contact with the Pt working electrode and forms dead lithium. (e) There is an SEI layer formed from the first cycle with a thickness of about 1.6 µm; (f) the lithium starts plating; (g) lithium continually plating; (h) finally, a small amount of dead lithium is formed, and the SEI layer becomes thicker. Potential vs. Pt reference electrode. Scale bars are 2 µm in all cases.

The first cycle of LP30 with and without FEC showed broadly similar Li plating and stripping behavior, likely due to the first cycle being associated with the formation of the initial SEI. As the FEC additive affects the SEI composition we would expect to see differences manifest in subsequent cycles. Figure 4.11 presents in-situ STEM image series

for the second plating and stripping cycle. With LP30 with no additive, before the second cycle plating, some residual ‘dead Li’ left from the first cycle can be seen, as marked by the yellow arrows in Figure 4.11a. The lithium plating process is shown in Figure 4.11b-c and the final state is shown in Figure 4.11d. For the LP30 with 5% FEC experiment, a SEI layer whose thickness was around 1.6 µm, was seen before the second cycling (as shown in Figure 4.11e). Similarly, the lithium plating process is shown in Figure 4.11f-g and the final state is shown in Figure 4.11h. It is clear to see, the lithium plating/stripping evolution in the second cycle indeed showed different behaviors to that observed for the first cycle for both no FEC and the 5% FEC electrolytes.

As illustrated in Figure 4.11a-d, rather than exhibiting the granular structure seen in the first cycle, the plated lithium in LP30 has a loosely packed needle-shaped morphology. These deposits also protruded much further out from the working electrode. Finally, there is a lot of dead lithium formation after the second cycle, which is shown in Figure 4.11d. By contrast, all the lithium plating/stripping happens inside the SEI layer for the FEC case. The SEI is lifted with lithium deposition. And during stripping, as these lithium deposits got stripped away, the SEI layer retracted back toward the Pt electrode surface. The SEI’s thickness also increased substantially after the second cycle, as compared in Figure 4.11e & h, from 1.6 µm to 2.4 µm. This indicates that the SEI grows with increasing plating and stripping cycles rather than staying at a constant level.

To better understand this difference, the lithium morphology evolution during the stripping process in the second cycle was especially investigated, which is illustrated in Figure 4.12. During the stripping process in LP30 electrolyte, the lithium from this loosely packed dendrite (as shown in Figure 4.12a) is not necessarily removed exclusively from the dendrite tip; other parts may be stripped first, cutting off the conductive path to the dendrite

tips and areas further away from the electrode surface (as shown in Figure 4.12b-c). These isolated particles become dead lithium and no longer grow or shrink with cycling (as shown in Figure 4.12d). This uneven stripping can be attributed to the sparse dendritic morphology, which leads to the electron channel easily being severed from the electrode. By contrast, the fluorinated system shows a finer lithium deposition, where all the lithium plating happens inside an obvious SEI layer. The plated lithium pieces are well connected and appear to form a more uniform deposition structure (as shown in Figure 4.12e), compared to the non-additive case. This relatively dense and uniform lithium deposit morphology allows most lithium to maintain electric contact with the working electrode during the stripping process. As a result, the stripping proceeds smoothly from the tips to the base (as shown in Figure 4.12f-g), which minimizes dead lithium formation (as shown in Figure 4.12h). The contrast signal of the lithium deposits was also seen to constantly decrease during stripping, further indicating a uniform stripping process.

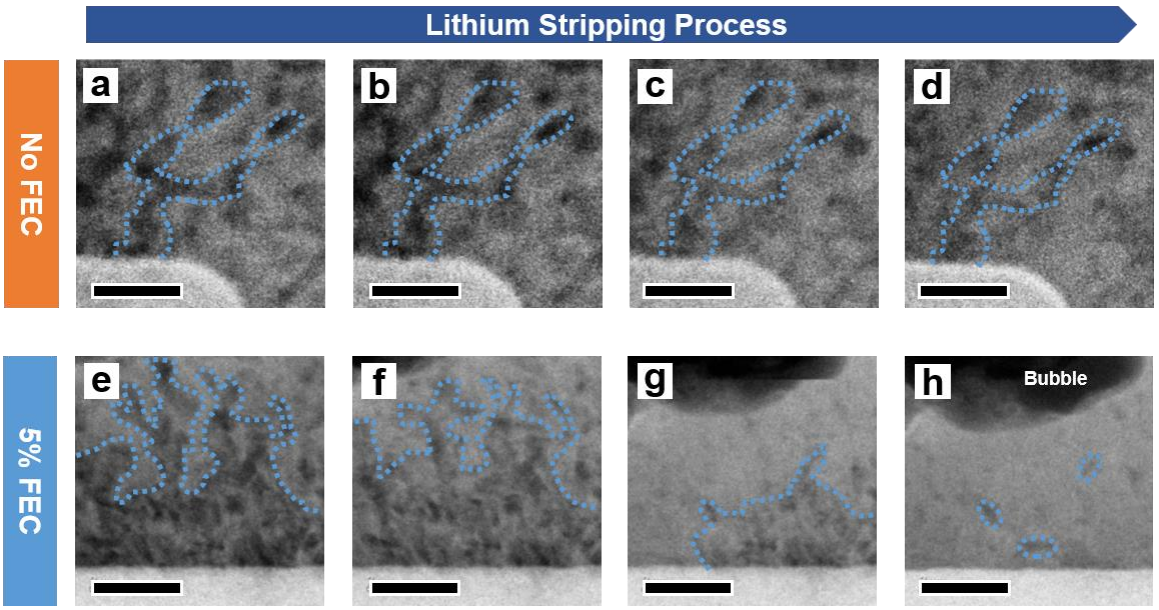


Figure 4.12. LC-STEM of the lithium structural evolution in the second cycle. (a-j) Stripping process in the second cycle, showing the influence of FEC on lithium morphology and dead lithium generation. (a-d) and (e-h) are frames captured from the real-time stripping process. The scale bar is 2 μm.

So far, the dynamic plating and stripping processes for the first two cycles of both the LP30 without and with 5% FEC additive were studied. What is particularly fascinating is that the first-cycle plating and stripping processes are more or less the same between the two systems, but the second-cycle plating and stripping processes are significantly different. We believe this difference is a result of the SEI formed from the first cycle. For the first cycle, there is little pre-existing SEI for both systems, therefore there is no significant difference in their plating morphology. After the first cycle, each of the two systems formed their type of SEI layer. However, it is difficult to analyze this layer in detail under LC-STEM, some observations can be made, particularly regarding the thicker SEI.[18,35,212] In the FEC system, the SEI layer grows thicker over the course of cycling (Figure 4.11e-h), while no SEI layer is directly seen in the additive-free study. However, we can infer its presence by observing the movement of dead lithium pieces left from the previous cycles, which were pushed away from the electrode during the following plating cycle (Figure 4.11). Their coordinated movement indicates the existence of an underlying SEI matrix that acts as a scaffold, moving the encapsulated dead lithium pieces with it during cycling, as studied in prior work.[213]

Therefore, some of the properties of SEI can be studied through analysis of the dead lithium movement in the two electrolyte systems. The dead lithium movement in the third cycle in both LP30 with and without 5% FEC electrolytes was studied in Figure 4.13. For the no additive case, the dead lithium (marked with a dotted white box) was pushed away during plating but did not return on after stripping (as shown in Figure 4.13). Similarly, the dead lithium has been pushed away during plating in the FEC case (marked with a dotted white circle). Yet, it can be seen to partially return during the stripping cycle, indicating that the SEI may be more elastic, as suggested in previous studies.[69,214] This process can be seen more clearly in the real-time recording.

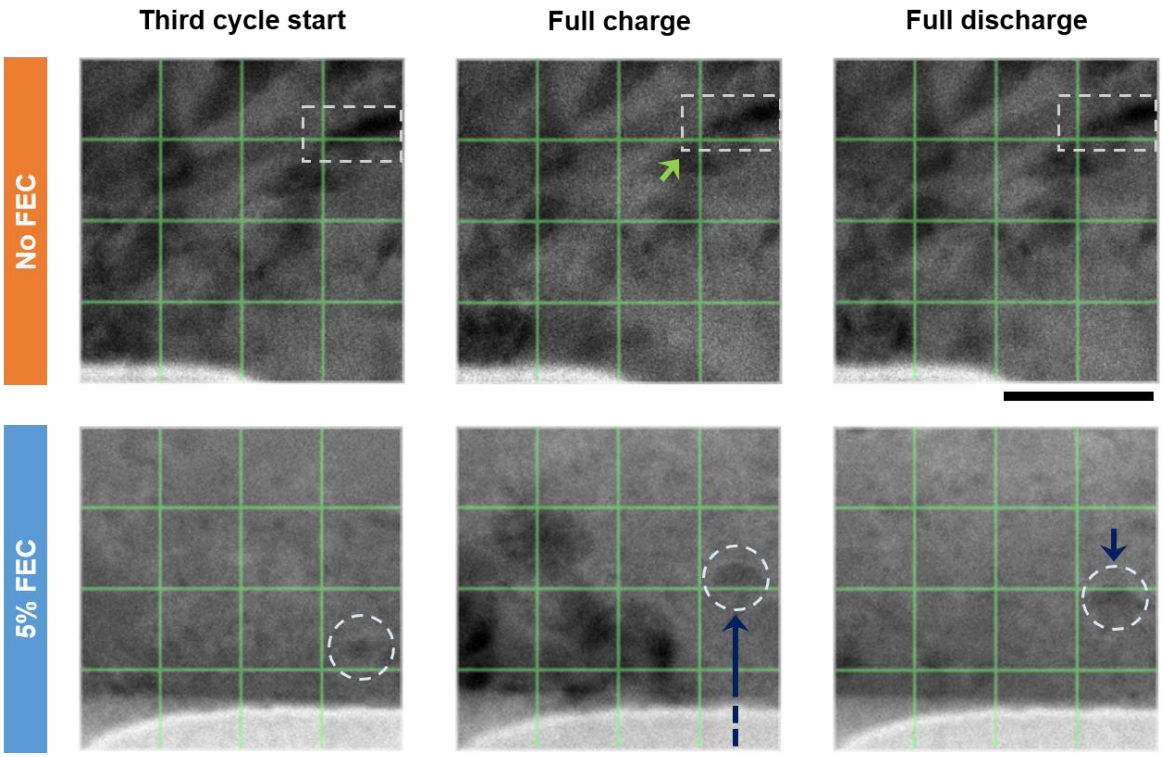


Figure 4.13. LC-STEM images of the lithium structural evolution in the third cycle. The dead lithium movement in the third cycle in LP30 and LP30 with 5% FEC is illustrated. Before the plating in no FEC case, there are lots of dead lithium from previous cycles, such as the dead lithium marked with a dotted white box. After the plating, the dead lithium is moved up a little bit, and it stays still after the stripping. By contrast, there is very little dead lithium in LP30 with the FEC case before cycling. A piece of dead lithium is chosen which is marked with a dotted white circle. After the plating, the dead lithium is moved up. Compared to the dead lithium in no FEC case, it is moved down obviously after cycling. The scale bar is 2 μm.

4.2.2 SEI chemical composition analysis by SIMS and NMR

To get a deeper understanding of how FEC additive affects SEI composition and how this subsequently influences the lithium plating and stripping processes, a comprehensive characterization of the SEI by online-MS, SIMS, NMR, and EIS was conducted with Li||Cu coin cells using the same LP30 electrolyte with and without 5% FEC.

Firstly, to confirm the formation of fluoride-rich interphase after adding FEC, depth profile SIMS analysis using a plasma-focused ion beam (PFIB) was used to quantitatively compare the $^{19}F^{-}/^{7}Li^{-}$ ratios from deposited lithium with the LP30 and LP30 with 5% FEC electrolytes. Both samples were plated for 20 minutes at 1 mA cm^{-2} in Li||Cu coin cells. The fluoride

distribution in these samples was investigated using SIMS depth profiling. A typical mass spectrum from a sample with 5% FEC is shown in Figure 4.14a and identifies the signals of interest; $^{7}Li^{-}$, $^{16}O^{-}$, and $^{19}F^{-}$. With depth profiling, these three signals could be obtained at every depth layer and the data is shown in Figure 4.14b. The final SIMS crater depth was also measured using PFIB sectioning, with an example of the cross-sectional view of a SIMS crater from the 5% FEC sample shown in Figure 4.14c. From this depth calibration, we can estimate that each sputtering cycle can remove a layer ~360 nm thick, so each elemental frame was created by removing a layer ~120 nm thick.

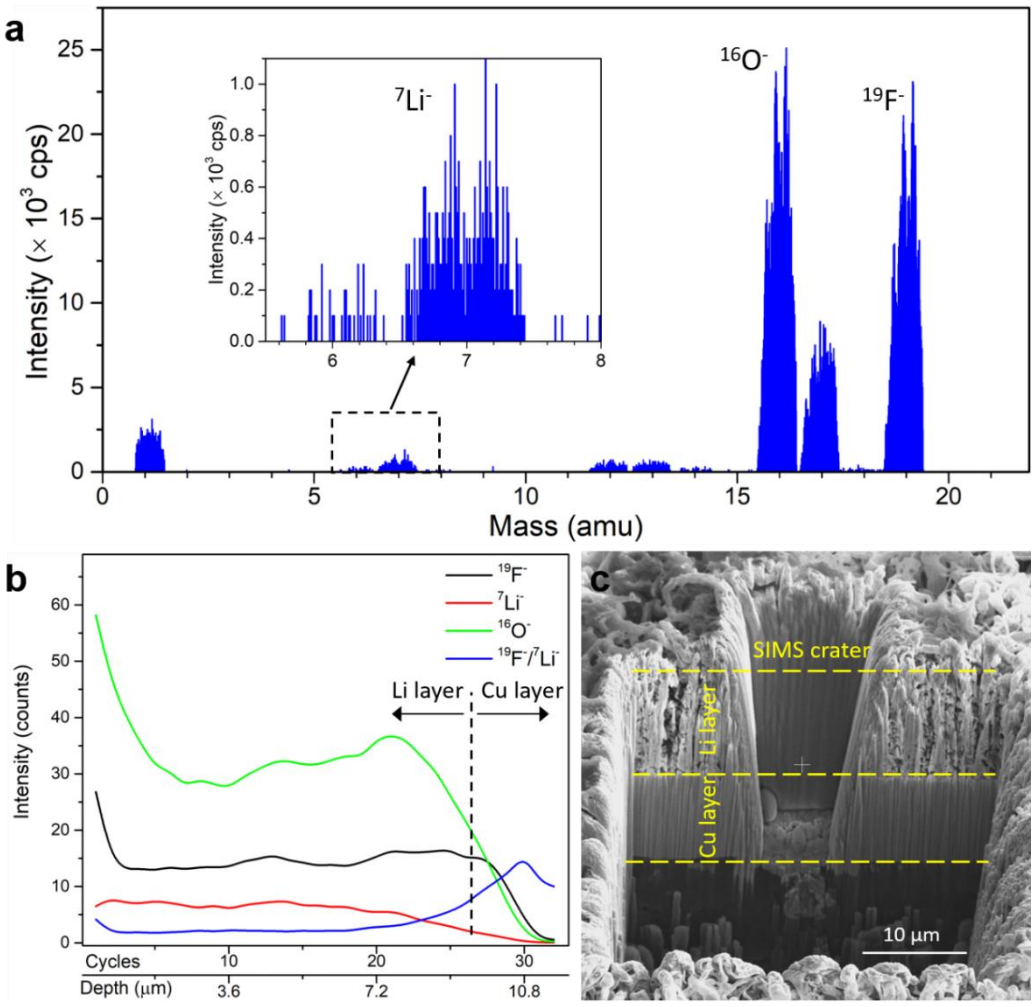


Figure 4.14. PFIB-SIMS profiling to measure the $^{19}F^{-}/^{7}Li^{-}$ ratio from the deposited Li sample. (a) Representative SIMS spectrum, showing counts from the negative Li, O, and F ions. (b) SIMS depth-profiling data through the Li layer, and (c) SEM cross-sectional view of the final SIMS crater. Using the SEM image as depth calibration, we can estimate that each cycle of sputtering removes a layer ~360 nm thick. The SIMS experiment and data analysis are performed by Dr. Junliang Liu.

The $^{19}F^-/^7Li^-$ ratio in the two systems is illustrated in Figure 4.15. Quantification using SIMS is challenging as different ion species can exhibit different ionization yields, and the nature of the matrix may also affect the yield or sensitivity (the so-called matrix effect).[215] This matrix effect explains the increase in the $^{19}F^-/^7Li^-$ ratio towards the interface with the Cu foil (as shown in Figure 4.15). Using the same SIMS depth profiling conditions (working distance, working voltage, current, dwell time, etc.), we can semi-quantitatively compare the levels of fluoride enrichment in the two systems using the $^{19}F^-/^7Li^-$ ratios. The $^{19}F^-/^7Li^-$ ratio in the No FEC system is around 0.74 ± 0.04 (as shown in Figure 4.15a), while the $^{19}F^-/^7Li^-$ ratio in the 5% FEC system is approximately 2.0 ± 0.2 (as shown in Figure 4.15b). It illustrates that the $^{19}F^-/^7Li^-$ ratio in a 5% FEC system is significantly higher than without FEC, confirming that the FEC additive yielded a fluoride-rich SEI.

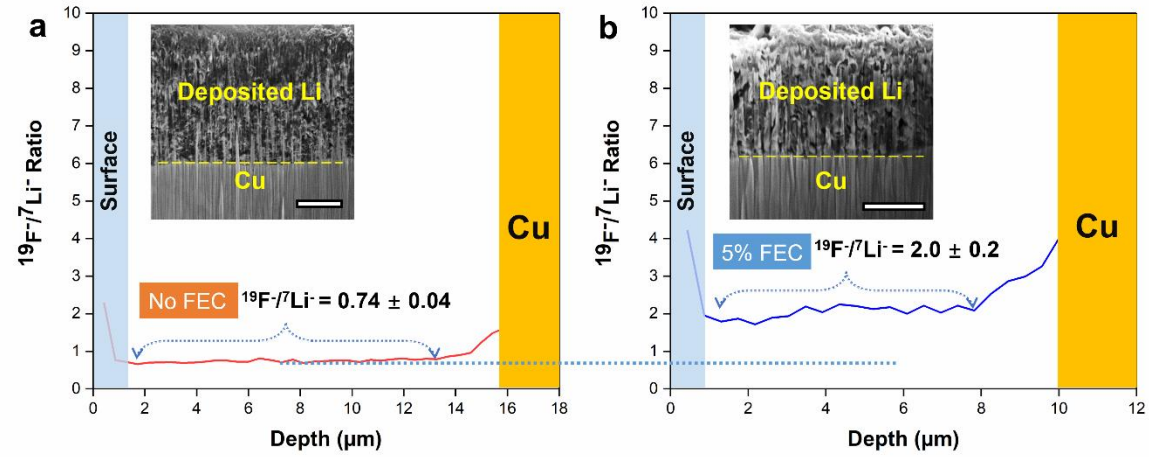


Figure 4.15. Characterization of the SEI chemical composition. (a-b) PFIB-SIMS depth profiles quantify the relative amount of fluoride ions in deposited lithium from LP30, with and without a 5% FEC additive, by comparing the negative ion $^{19}F^-/^7Li^-$ ratio. (a) The $^{19}F^-/^7Li^-$ ratio was measured at 0.74 ± 0.04 in the deposited lithium in LP30; (b) the $^{19}F^-/^7Li^-$ ratio has a platform at 2.0 ± 0.2 with the presence of FEC. Inserts show SEM images of the deposited lithium layer cross-sections from which the SIMS profiling data were acquired. Scale bars are 5 μm. The SIMS experiment and data analysis are performed by Dr. Junliang Liu.

To further explore the chemical composition in the SEI, the Solid-state magic-angle

spinning NMR of ^{7}Li was performed on the deposited lithium in LP30 with 5% FEC electrolyte (as shown in Figure 4.16). It clearly confirms the presence of LiF on the plated Li surface. As introduced before, LiF is believed to be a critical component of a high-performance SEI layer. In addition, LiH was also discovered in the SEI. The existence of LiH was a controversial discussion in the SEI structure.[21,216] Thus, more methods are required to confirm its existence, and the online-MS experiment below is designed.

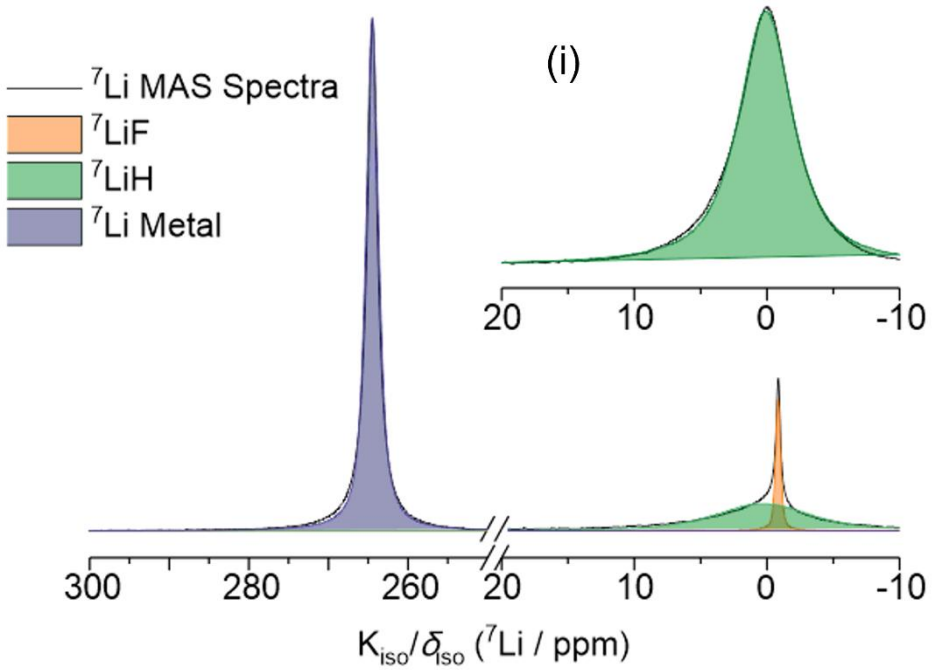


Figure 4.16. The ^{7}Li magic angle spinning (υ_R = 10 kHz) NMR (υ_0 = 155.5 MHz) spectrum of plated lithium. The resonance at K_{iso} = 264 ppm is vertically aligned Li metal (with respect to the magnetic field, B_0).[217] The peak at δ_{iso} = −1 ppm is in good agreement with that of $LiF_{(s)}$.[151] A further broader ^{7}Li resonance is centered between 0 – 1 ppm and is in good agreement with bulk $LiH_{(s)}$ shown in the inset (i). I made all the sample preparation. The NMR experiment and data analysis are performed by Dr. Gregory Rees.

4.2.3 Online-MS analysis

The operando STEM experiments revealed a significant difference in dead lithium formation between the two electrolyte systems. To explore this at the coin-cell level, online-MS (shown in Figure 3.6) was designed. As introduced in Chapter 3.3.4, this method was

performed by adding deuterated water (D_2O) to cycled electrode specimens and measuring the resultant gas evolution. This permitted quantitative identification of the sources of lithium loss – whether by detachment and electrical isolation (dead lithium) or by being consumed in an expanding SEI.[218,219] Measuring the evolved gases with MS allows us to identify the various gas species, which can be assigned as products from particular reactions that correspond to the amount of unreacted metallic lithium (which we assume to be exclusively dead lithium), lithium hydride (LiH), and some SEI organic species such as $(CH_2OCO_2Li)_2$ and $LiOCO_2R$ (we will refer to as 'C-organic SEI' here). The titration chemical reactions are as follows:

$$(1)\ 2Li + 2D_2O = 2LiOD + D_2\uparrow$$

$$(2)\ LiH + D_2O = LiOD + HD\uparrow;$$

$$(3)\ 2LiOCO_2R + D_2O = Li_2CO_3 + 2ROD + CO_2\uparrow$$

$$(4)\ (CH_2OCO_2Li)_2 + D_2O = Li_2CO_3 + (CH_2OD)_2 + CO_2\uparrow$$

This quantitative isotope titration method is effective to study the irreversible lithium after stripping because it studied the left structures on copper foil in a stripped coin cell. The reversible lithium can be learned from the electrochemical galvanostatic diagram because the reversible lithium is stripped lithium. The ratio of reversible lithium to deposited lithium is the coulomb efficiency. More details are introduced in Chapter 3.3.4. Therefore, the lithium distribution ratio after specific cycles can be obtained and it is illustrated in Figure 4.17. From this distribution diagram, we can learn that the dead lithium is the main reason to cause the capacity loss in the LP30 electrolyte battery, especially after the first cycle. By contrast, less dead lithium formed in the LP30 with a 5% FEC battery.

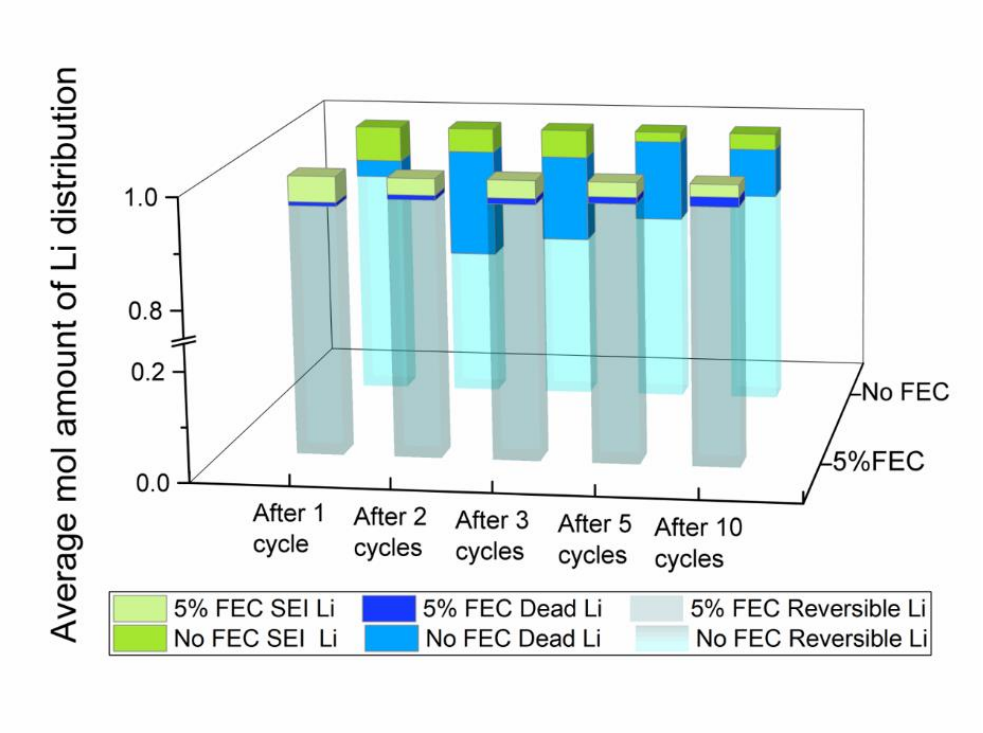


Figure 4.17. The measured lithium distribution ratio after the specified number of cycles for each electrolyte. The lithium was plated and stripped at 1 mA cm^{-2} for 2 hours in Cu||Li coin cells.

For showing more details of the dead lithium and SEI components, the amount of metallic dead Li, LiH, and 'C-organic SEI' from LP30 with and without 5% FEC additive after completing 1, 2, 3, 5, and 10 cycles are compared and shown in Figure 4.18. A trend can be seen for all these components; for plating in LP30 with and without FEC additive, the amount of all three (metallic Li, LiH, 'C-organic SEI') increased with several cycles. The increase in LiH and organics indicates that in both systems, SEI growth is a continuous process. However, plating through a fluoride-rich SEI showed significantly smaller increases of these SEI components (LiH and 'C-organic SEI'); over 10 cycles, FEC effectively reduced dead lithium formation by more than 80%, LiH formation by 34%, and C-organic formation by around 47%. This confirmed that the 5% FEC additive effectively reduced the amount of total SEI formed during cycling and further decreased the electrolyte decomposition.

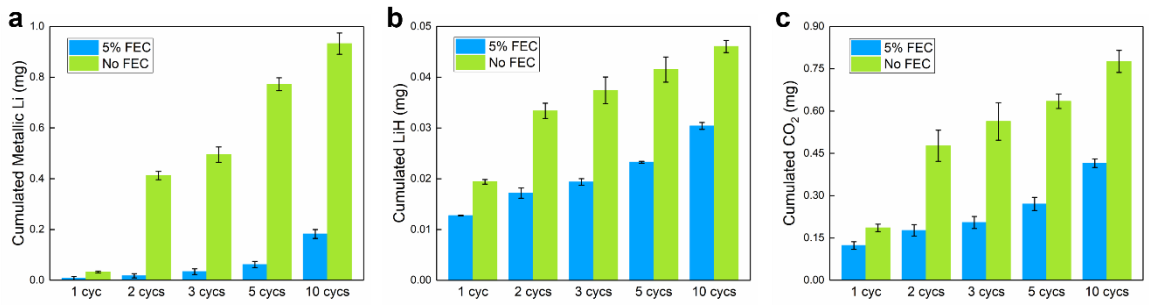


Figure 4.18. Quantification of metallic lithium and certain SEI components by online mass spectrometry. (a-c) Measured cumulative metallic Li, LiH, and organic SEI components such as $(CH_2OCO_2Li)_2$ and $LiOCO_2R$ following the specified number of cycles. The lithium was plated and stripped at 1 mA cm^{-2} for 2 hours in Cu||Li coin cells.

Especially, far less dead lithium forms when a fluoride-rich SEI is present as shown in Figure 4.18a, consistent with our previous STEM results and that this dead lithium consumed a smaller proportion of the irreversible lithium in the system. It is worth mentioning that these two systems both showed the presence of LiH in the SEI, as was further confirmed by NMR (as shown in Figure 4.16). There have been few investigations into the possible influence of LiH in Li-battery performance; however recent cryo-STEM studies have suggested that LiH can form into dendrites and cause significant capacity loss.[19] Our results quantifiably demonstrate that less LiH is formed when the FEC additive is employed, suggesting an additional benefit of fluoride-rich interphase for promoting high cycling efficiency.

4.2.4 Electrochemical impedance spectroscopy (EIS) analysis

To compare the ionic conductivity of SEI, the EIS measurement was performed on the corresponding lithium metal batteries. The Li||Cu coin cells were plated in LP30 with and without 5% FEC electrolytes at a current density of the usual 1 mA cm^{-2}. As shown in Figure 4.19, the ionic conductivity is much higher in the 5% FEC cell compared to the No FEC cell, whether the deposition time is 20 minutes or 2 hours. More experimental details

are shown in Chapter 3.2.3.

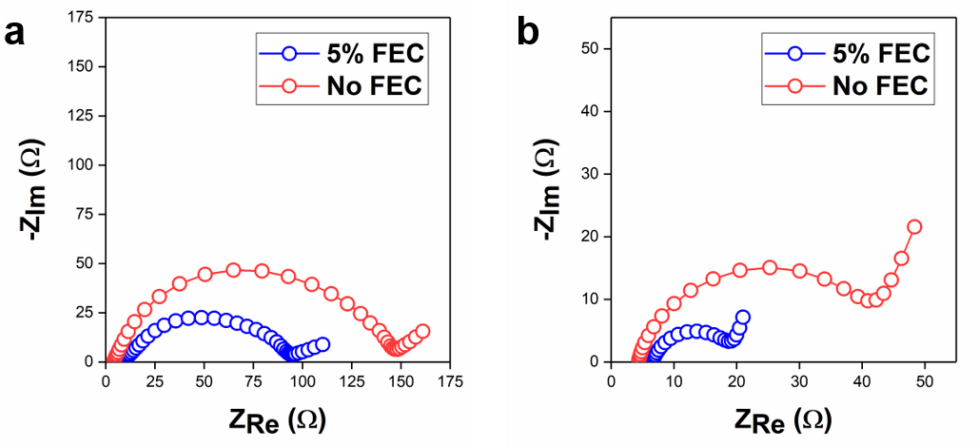


Figure 4.19. Nyquist impedance spectra of Li||Cu coin cells with LP30 with and without FEC electrolytes. (a) Measured after galvanostatic lithium plating for 20 min at 1 mA cm^{-2}. (b) Measured after the first galvanostatic cycle (plated at 1 mA cm^{-2} for 2 hours). It illustrates that the ion conductivity is higher with 5% FEC, for both during plating and after stripping.

4.3 Discussion

4.3.1 The effects of fluoride-rich interphase

The PFIB-SIMS and online MS studies, taken together with the operando STEM observations, demonstrate that the fluoride-rich SEI formed during the first cycle significantly affects the following lithium plating and stripping dynamics (Figure 4.11 and Figure 4.12). The real-time observations underline the importance of the structural dynamics of lithium growth during deposition and stripping, with a clear preference for a uniform and denser morphology. These finer morphologies ensure that a path is always available for electrons to reach the lithium, allowing for dissolution to take place.[21] By contrast, the dendritic structures observed in the fluoride-deficient SEI were more susceptible to electrical isolation during stripping. While the real-time STEM imaging provides direct confirmation of the beneficial role of a fluoride-rich SEI in facilitating the formation of reliably strippable lithium structures, understanding how the SEI facilitates

this remains complex. There is an increasing understanding around the likely importance of LiF as an SEI constituent,[203] and while it has a poor ionic conductivity at the bulk scale, recent work has shown that it forms nanoparticles dispersed through the SEI, meaning in practice interfacial and other mechanisms are more likely to dominate ionic conductivity.[220]

The PFIB-SIMS and NMR results suggest that the fluoride-rich SEI likely contains more LiF, and EIS measurements (Figure 4.19) demonstrate a marked improvement in ionic conductivity. Based on the TEM observations, the fluoride-rich SEI provides a more homogenous ionic conductivity distribution, leading to the formation of flatter structures on plating, and preventing 'hot spots' of ionic conductivity during stripping that could cause lithium isolation. The mechanical role of the SEI may also influence performance, with a durable and elastic layer more able to accommodate the volume change during cycling. Less continued SEI formation and less electrolyte decomposition occurred with the fluoride-rich interphase, as the elastic SEI will ensure that reactive Li is less frequently left exposed to the electrolyte, leaving fewer opportunities for excess SEI to form. Thus, the coulombic efficiency is significantly improved by fluoride-rich interphase.

4.3.2 The impacts of bubble on the electroplating and stripping of lithium on LC-STEM experiments

The bubble effects have to be discussed in the LC-STEM experiments because it is about whether our LC-STEM results are reliable. In general, we can expect the bubble may have a significant role in inhibiting ion transfer due to reducing the contact area between the electrolyte and the electrode/SEI. Therefore, we compared the morphology of lithium deposited between areas where the bubble is in close proximity and where it is further away, and between the first and second cycles (as shown in Figure 4.20). In Figure 4.20a, we can see a bubble close to deposited lithium in the second cycle. When we move around the field

of view and move away from the initial bubble (Figure 4.20b), the lithium deposition morphology is discovered to remain similar. It indicates that the bubble does not control the lithium deposition morphology. By comparing the lithium deposition morphology between the first and second cycles (Figure 4.20a, b, and Figure 4.20c, respectively), we can see a clear difference in morphology. However, the bubble can be seen nearby during lithium plating for both Figure 4.20a and Figure 4.20c. The main effect of the bubble on lithium plating would be to limit ion transport. If the bubble has a significant impact, we expect it to control lithium plating morphology due to limiting ion supply, and thus for the lithium deposits in Figure 4.20a and Figure 4.20c to be similar. We instead see distinct morphologies, which we propose to be due to the development of a favorable fluoride-rich SEI layer during the first cycle. While these observations do not eliminate any confounding role the bubbles may have on lithium plating behavior, they suggest that it is secondary to the fluoride-rich SEI mechanism we propose.

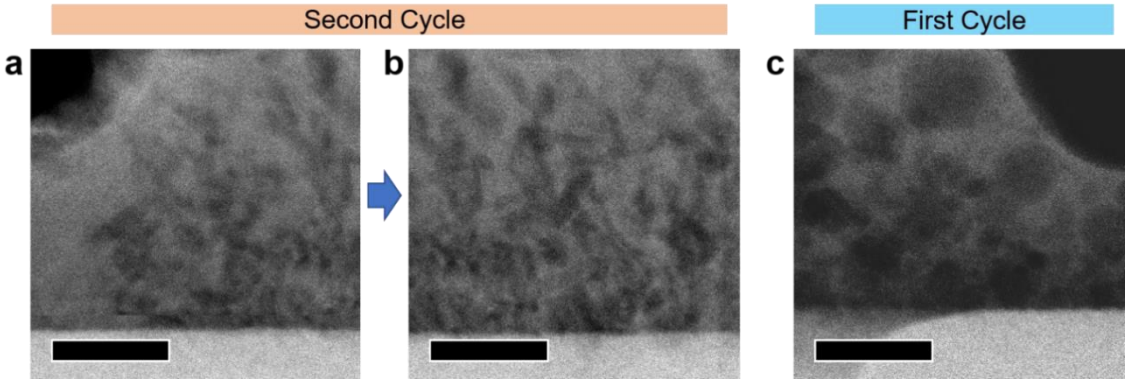


Figure 4.20. In-situ liquid-cell HAADF-STEM images from lithium plating of LP30 + 5% FEC. (a-b) Lithium plating from the second cycle. (a) A bubble is present near the lithium deposition site. (b) Moving the field-of-view, lithium plated away from the initial bubble location exhibits consistent structure observed in (a). (c) Lithium plating from the first cycle shows distinct lithium morphology to the second cycle, despite being a similar distance from a bubble, suggesting an alternative mechanism behind the difference in deposition morphology. Scale bars are 2 µm in all cases.

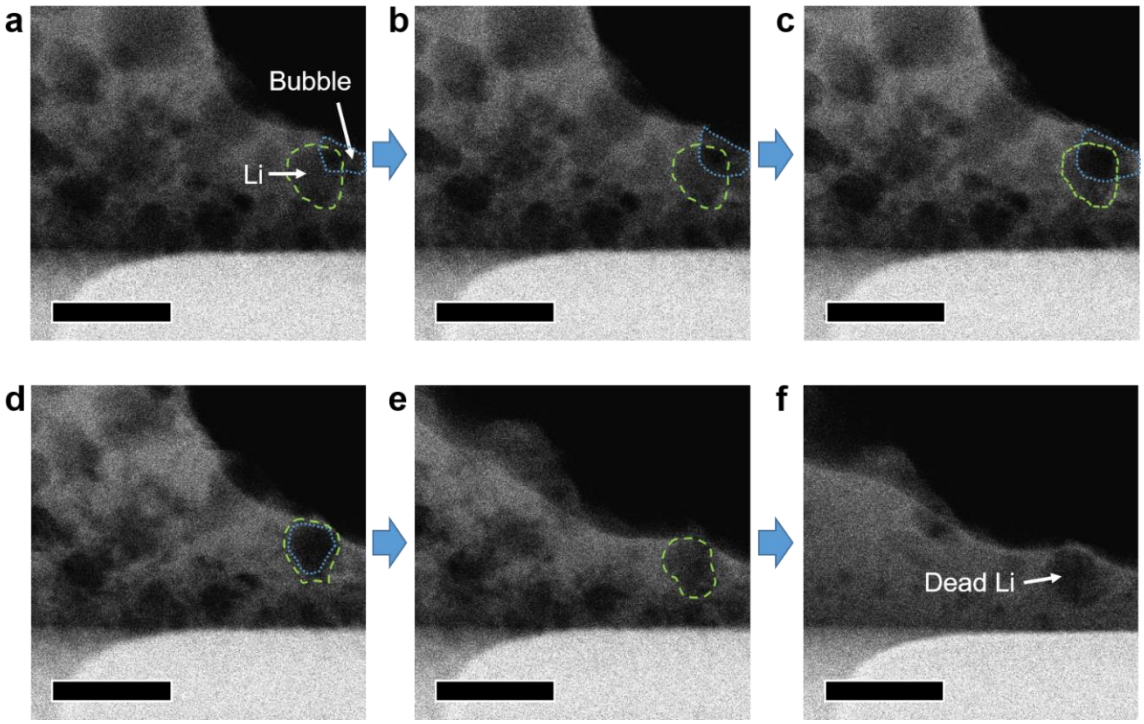


Figure 4.21. The effect of a nearby bubble on Lithium stripping. A small bubble formed off the larger parent bubble in the top right (dotted blue line) and grew over the plated lithium (dashed green line) at the start of the lithium stripping cycle. (a) to (c) shows the bubble grows from the big bubble toward the plated lithium deposit. (d) The bubble fully overlaps the lithium, inhibiting ion flow, and thus it does not undergo dissolution during the stripping cycle. (e) The bubble disappears, presumably re-merging with the larger growing bubble to the top right. (f) The lithium deposit interacting with this bubble remains as a large dead lithium deposit. Scale bars are 2 µm in all cases.

The bubble does have effects on the lithium stripping behaviour. A careful examination of the data reveals an instance of a bubble interacting with a lithium deposit in a manner that strongly inhibits its electrochemical dissolution. In the first cycle of the FEC experiments, a small bubble was observed to grow off from the larger parent bubble (as shown in Figure 4.21). The smaller bubble grows to overlap the plated lithium deposit (Figure 4.21a-c). This occurs at the start of the electrostripping cycle. From Figure 4.21d onwards, the lithium on the electrode can be seen to undergo rapid stripping. However, the lithium adjacent to this small bubble remains unaffected mainly, with changes in its shape due to some limited dissolution combined with particle rotation. This tiny bubble eventually re-joins the larger

bubble in Figure 4.21e, evidenced by a change in contrast in the indicated area, yet this stage has completed the stripping cycle. The lithium deposit that interacted with this bubble remains, unable to undergo dissolution during stripping due to the bubble's presence, thus becoming electrically isolated as the surrounding lithium was removed. This shows that gas bubbles can strongly influence the lithium electroplating and stripping behavior by limiting ion transfer between the electrode and the electrolyte; however, they appear to need to be close to have this impact. The dynamic movies are more clearly observed in motion, which is shown in the paper we published before.[221]

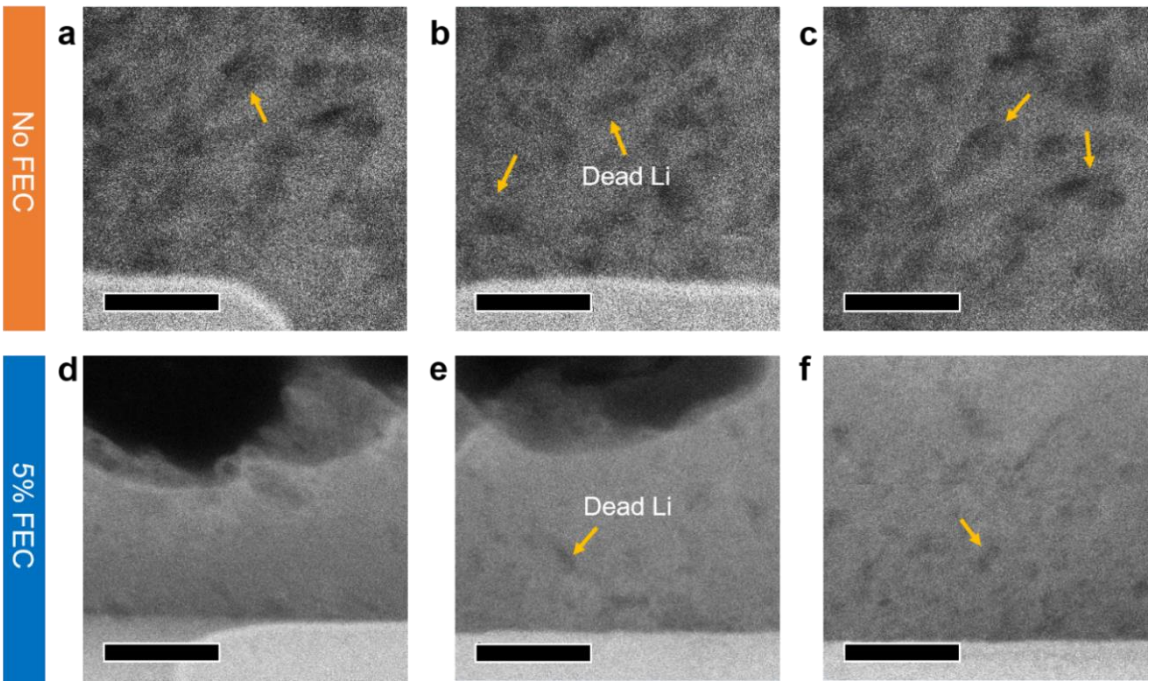


Figure 4.22. Moving around the working electrode after the second lithium stripping cycle to allow comparison of dead lithium distribution. (a-c) The No FEC case and (d-f) the FEC case. Consistent dead lithium distributions were observed in each experiment away from the initially imaged field of view. Scale bars are 2 μm in all cases.

Another question is that does the bubble promote the lithium stripping in 5% FEC because

the results shown in Figure 4.11 show the superior stripping performance of the 5% FEC additive electrolyte and the bubble occurs. To show that the relative effectiveness of the stripping is consistent across the working electrode, we moved the stage to examine areas of the electrode away from the field of view where the CV cycle was captured. We can then compare the quantity of remaining dead lithium deposits to infer the relative effectiveness of stripping behaviour between the two systems (as shown in Figure 4.22). This suggests that the superior stripping performance is consistent across the working electrode and not unique to the filmed area. In addition, Figure 4.22f is away from any apparent bubble and shows a consistent dead lithium quantity to that observed in Figure 4.22e.

The effect of any bubble would be to inhibit the dissolution of lithium during the stripping cycle. However, we directly observe the opposite. This shows that if the bubble is having any effect, it must be secondary to the dominant effect of the SEI composition. Thus, the bubble has a limited impact on our LC-STEM results.

4.4 Conclusion

In these studies, the real-time dynamics of lithium plating and stripping and how this is affected by the presence of fluoride-rich interphase were directly imaged by LC-STEM. By comparing lithium cycling across fluoride-poor and fluoride-rich interphases, we have demonstrated that the fluoride-rich SEI suppresses dead lithium formation and decreases electrolyte decomposition. Imaging the dynamics of lithium cycling revealed that the fluoride-rich SEI yields a flatter and finer plated lithium structure that presents a better morphology for uniform stripping, thus resulting in a significant reduction in dead lithium. Direct imaging is the first choice for studying material evolution. These observations further verify that fluoride-rich interphase is more uniform and durable, which promotes

uniform lithium plating/stripping.

In addition, the isotopic labeling method was used in this project in the online-MS titration analysis. By employing D_2O, the LiH and dead lithium can be distinguished, and the LiH was quantificationally verified in the SEI component. Whether or not LiH exists in SEI of lithium metal batteries is a matter of debate before.[19,21] we are one of the pioneers to supply solid evidence to confirm its existence.

With the help of online-MS quantitative titration analysis, the dead lithium was found to be the main degradation reason for the lithium metal batteries. There is a large amount of dead lithium formation in every cycle and it is different with the lithium-ion batteries. Furthermore, the continuous electrolyte decomposition was also verified by the quantitative method because there are lots of LiH and 'C-organics' generation in each cycle. Both of them are SEI components, so the electrolyte has to be consumed continuously. The FEC additive can effectively decrease the dead lithium formation and prevent electrolyte decomposition, thus it improves the coulombic efficiency. This degradation study provides an idea for improving the coulombic efficiency of lithium metal batteries.

Chapter 5. Operando Study of the Role of Electrolyte Solvents for Sodium Metal Battery

5.1 Introduction

A sodium metal anode is believed to be an ideal negative electrode for future sodium batteries.[125,126] Carbonate ester solvent-based electrolytes, which are widely used in lithium battery chemistries, have been found to form particularly unstable interphases on Na metal anodes, yielding higher interfacial impedances and much lower coulombic efficiencies than their lithium anode counterparts.[133,134] Employing glyme solvent electrolytes have shown promising results, with excellent electroplating and stripping performance. Attaining a more comprehensive understanding of the underlying mechanisms behind the improved performances for glyme electrolytes will help design reliably reversible sodium metal anode cells. In particular, it is essential to relate how the differing SEI links to potential degradation modes, such as the interphases' ionic conductivity, susceptibility toward continued reactions with the electrolyte, mechanical robustness, and others.

To develop an accurate understanding of how manipulating the electrolyte and SEI composition improves the electrochemical performance measured at the cell level, we need to diagnose precisely how it influences and changes the processes occurring at the electrode interface. The dynamic nature of these processes, coupled with the fragile nature of the metal-electrolyte interface, strongly favors the use of in-situ characterization techniques.[207,227–229] Applying appropriate in-situ techniques will thus prove invaluable for diagnosing the SEI's role in sodium electroplating and stripping, and precisely how different SEIs favor or impede metal anode cycling performance.

Here, the operando LC-(S)TEM, in-situ AFM, DEMS, etc., were performed to

systematically study the Na dynamic plating/stripping process in carbonate-based and ether-based electrolyte systems and figure out the role of electrolyte solvents in Na metal anode. My study reveals that the ether-based electrolyte promotes a robust SEI that is thin and has better elasticity. The conformal SEI could help suppress Na dendrites formation and lead to uniform Na deposition. Additionally, the bubble plays a vital role during Na deposition and dissolution because the generated gas could trap in the SEI shell and affect the Na further cycling. These findings for the SEI property and bubble formation in Na metal battery electrolyte systems will assist the researcher in better understanding the role of electrolytes during Na cycling and help to design a better electrolyte system further.

5.2 Results

5.2.1 Electrochemical performance analysis

The Na electrolyte, 1 M $NaPF_6$ in EC and DMC, EC: DMC = 1:1, and 1 M $NaPF_6$ in monoglyme (dimethoxyethane, DME), were employed as representative carbonate and glyme electrolytes. To better understand the Na degradation mechanisms in a carbonate-based electrolyte, the commonly used 10% FEC and 10% VC additives were also studied. The electrochemical performance was measured in Na || Cu cells as shown in Figure 5.1. In the first cycle (Figure 5.1a), the carbonate electrolyte cell yielded a poor coulombic efficiency (CE) of 24%. The inclusion of VC or FEC additives improved the CE significantly, reaching 70% and 74%, respectively. In contrast, the glyme electrolyte cell yields a much better CE of 94%. In the following 10 cycles (as shown in Figure 5.1b), the CE for the carbonate electrolyte cell decreased to 22%, and the CE for the VC and FEC additive cells were at 73% and 75%, respectively. These results demonstrate that the significant CE loss is not only for the first cycle but for every cycle. The VC and FEC

additives improve the electrochemical performance of sodium carbonate-based electrolytes, but the effects are limited and remain far below desirable levels. The CE for VC and FEC cells stabilizes at around 75% in the tenth cycle indicating that there are still dead sodium and SEI formation in the following cycles. Due to 75% of CE of the Na || Cu coin cell means around 25% sodium is irreversible during stripping. The irreversible sodium has to be consumed and cannot join the following cycles anymore. At each cycle in the galvanostatic mode, the same deposition capacity means the same amount of sodium coming from sodium anode to the Cu current collector (deposited at the same time under the same current density). So, both SEI formation (during plating) and dead sodium generation (during stripping) can cause irreversible sodium loss. It can be inferred that the SEI formed in previous cycle may be unstable, and cannot well passivate sodium and prevent electrolyte continual decomposition. However, the glyme electrolyte showed significantly better deposition/stripping performance, with its CE stabilizing at over 99.9%, indicating the lower CE of the first cycle was due to initial interphase formation losses, and that once formed the interphase remained stable over the subsequent cycles.

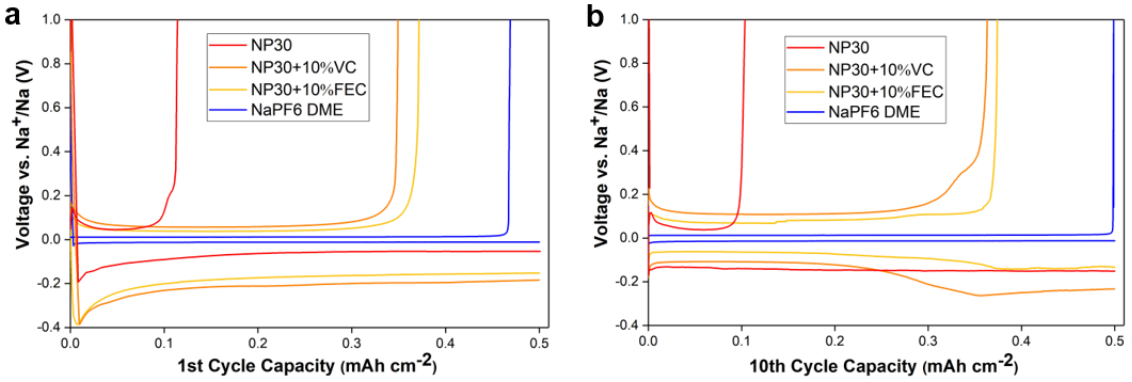


Figure 5.1. Electrochemical performance comparison of sodium electrolytes with carbonate or glyme solvents. Deposition capacity at 0.5 mA cm^{-2} for 0.5 mAh cm^{-2} after the (a) first and (b) tenth charge-discharge cycle. The 1 M $NaPF_6$ salt concentration for all electrolytes after the first cycle.

To test the electrochemical cycling stability of the glyme electrolyte. Fifty cycles were cycled in Na||Cu coin cells at 0.5 mA cm^{-2} for 0.5 mAh cm^{-2} capacity. As shown in Figure 5.2, the coulombic efficiency was very stable and kept at approximately 99.9% in fifty cycles. These results illustrate the outstanding electrochemical performance of glyme electrolytes in sodium metal batteries and they are consistent with the previous report.[133]

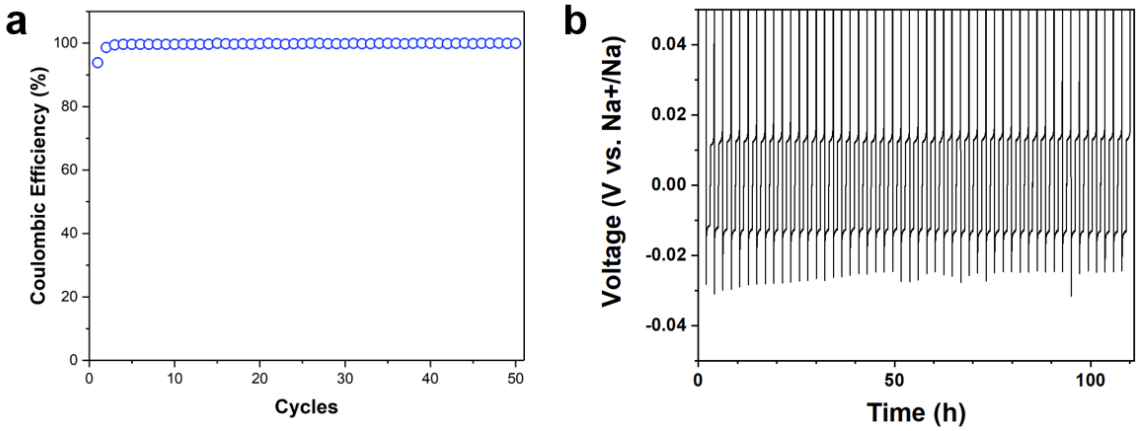


Figure 5.2. Cycling performance of Na||Cu coin cell using DME electrolyte. (a) Coulombic efficiency and (b) voltage over 50 cycles. Deposition capacity at 0.5 mA cm^{-2} for 0.5 mAh cm^{-2}, discharge to 1 V vs. Na^+/Na.

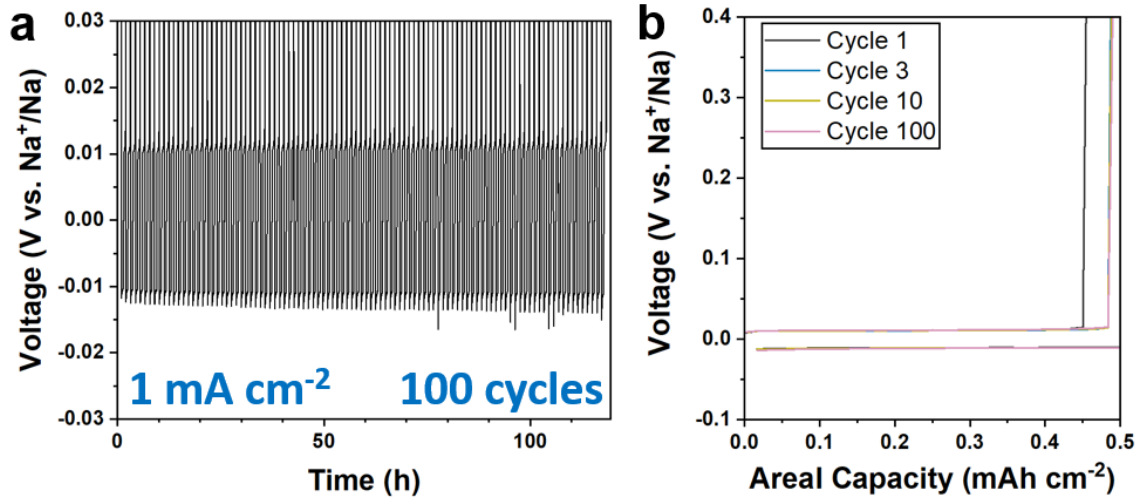


Figure 5.3. Cycling performance of Na||Cu coin cells using DME electrolyte at 1 mA cm^{-2} cycling rates for 100 cycles. (a) Cell voltage with time and (b) representative capacity plots for 1 mA cm^{-2} cycling rates, respectively. Deposition capacity of 0.5 mAh cm^{-2}, discharge to 1 V vs. Na^+/Na, for all cells.

Due to 0.5 mA cm^{-2} being a relatively low current density and some higher rates tests for the glyme electrolytes are required to show good performance. The higher rates of the current density of 1, 4, and 5 mA cm^{-2} were studied in Na||Cu coin cells and all to the same 0.5 mAh cm^{-2} areal capacity and discharged to 1 V vs. Na^+/Na. The 1 mA cm^{-2} current density was cycled for 100 cycles, as shown in Figure 5.3.

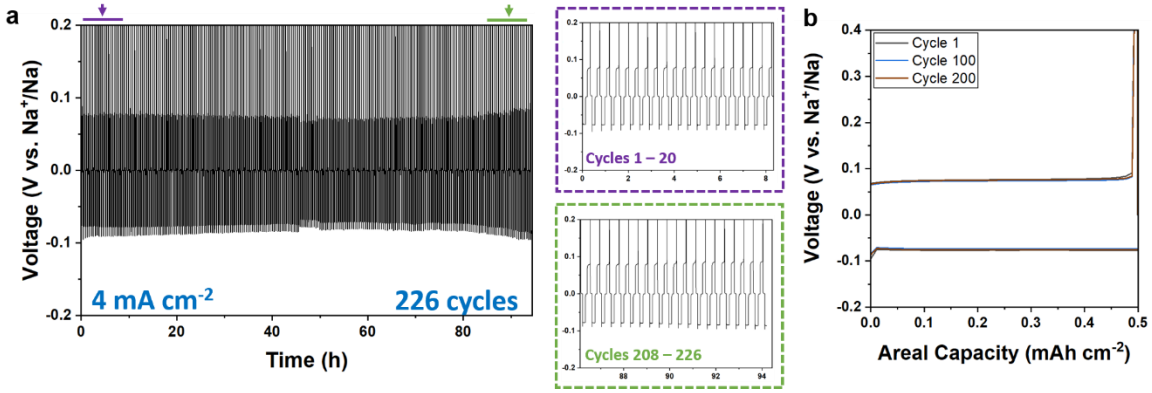


Figure 5.4. Cycling performance of Na||Cu coin cells using DME electrolyte at 4 mA cm^{-2} cycling rates. (a) Cell voltage with time and (b) representative capacity plots for 4 mA cm^{-2} cycling rates, respectively. Deposition capacity of 0.5 mAh cm^{-2}, discharge to 1 V vs. Na^+/Na, for all cells.

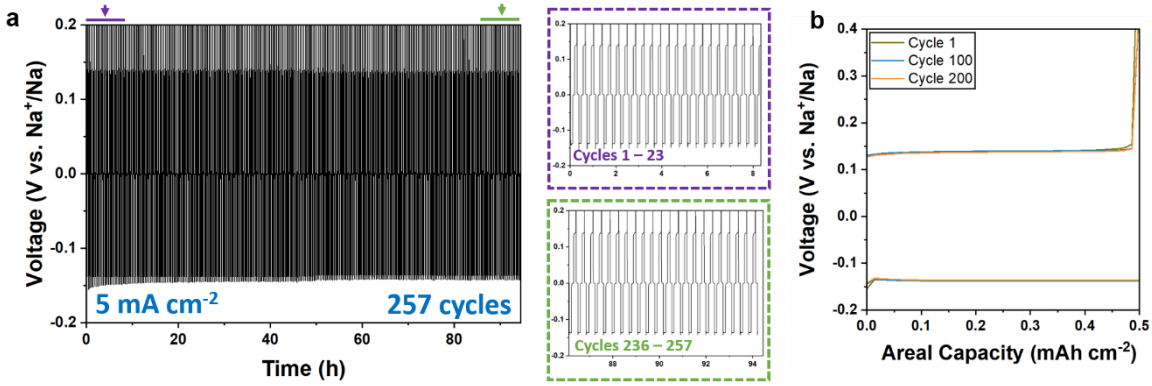


Figure 5.5. Cycling performance of Na||Cu coin cells using DME electrolyte at 5 mA cm^{-2} cycling rates. (a) Cell voltage with time and (b) representative capacity plots for 5 mA cm^{-2} cycling rates, respectively. Deposition capacity of 0.5 mAh cm^{-2}, discharge to 1 V vs. Na^+/Na, for all cells.

The 4 mA cm^{-2} and 5 mA cm^{-2} rates were cycled for over 90 hours (more than 200 cycles), as shown in Figure 5.4 and Figure 5.5. All the cells were running with a galvanostatic method. In each part, the cell voltage with time and representative specific cycle plots were presented in the Figures. From the electrochemical cycling data, we can clearly learn that the coin cells in glyme electrolytes have excellent cycling performance even at high rates, and the coulombic efficiency reaches over 99% in all of 1, 4, and 5 mA cm^{-2}. The high performance is maintained even after long cycling, with no drop in electrostripping capacity observed after one hundred cycles, which shows the cycling stability of glyme electrolytes.

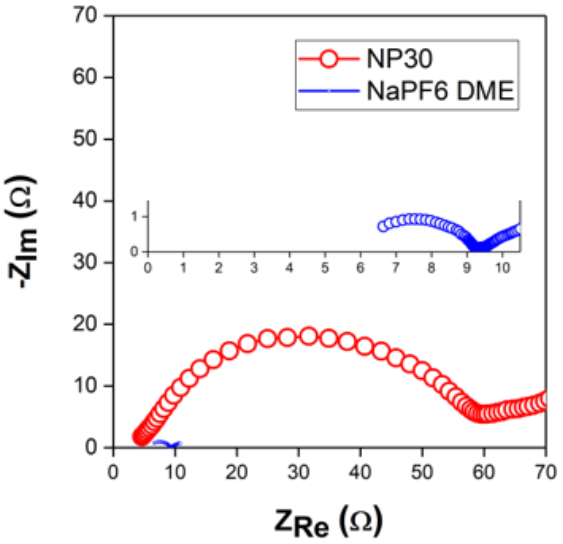


Figure 5.6. The EIS measurements of Na||Cu coin cells. A magnified view of the EIS of $NaPF_6$ in DME is shown in the insert. Both of the coin cells were deposited at 0.5 mA cm^{-2} current density for 0.5 mAh cm^{-2} capacity.

In order to explore why the glyme electrolytes have excellent performance, the impedance of the cells was measured as shown in Figure 5.6. The EIS measurements demonstrated a lower ionic conductivity for the carbonate electrolyte system, which might be attributed to a thicker SEI composed of compounds with low ionic conductivity. Since the two systems were tested using the same conditions, a big difference in resistance was likely the result of

different SEI formed during plating. Therefore, combined with the CE and EIS measurements, they suggested a critical role for the SEI in discriminating the performances of the two electrolytes.

To diagnose the contributions of initial SEI formation to Na loss, and to better quantify the overall size and composition of the SEI, online mass spectrometry (online-MS) was performed on the cycled electrolyte cells. The coin cells were plated at 0.5 mA cm^{-2} for 0.5 mAh cm^{-2}, stripped at 0.5 mA cm^{-2} to 1 V (vs. Na^+/Na) for one cycle, and then transferred to our online-MS setup where they were titrated with deuterated water (D_2O). The electrically isolated 'dead' Na and some SEI components were quantitatively identified by measuring the resultant gas evolution (D_2, HD, and CO_2). The quantity of reversible Na was known from the coin cell electrochemical performance, and the Na consumed in SEI equalled the amount of non-reversible Na minus the dead Na.[221] More experimental details were illustrated in Chapter 3.3.4.

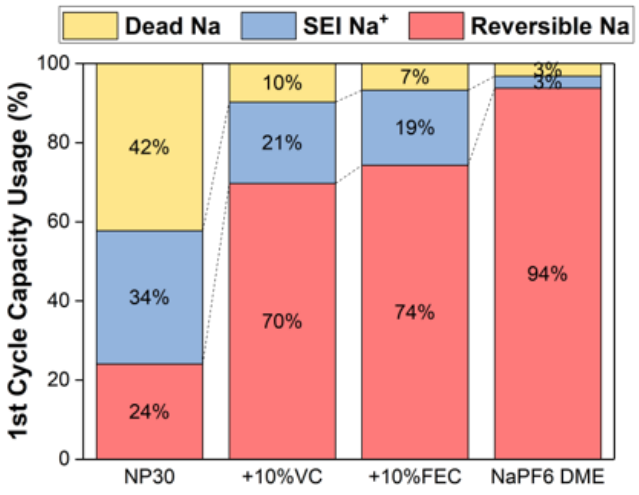


Figure 5.7. The Relative distribution of Na after the first charge-discharge cycle from online-MS titration measurement. The deposition capacity at 0.5 mA cm^{-2} for 0.5 mAh cm^{-2} for all the Na||Cu coin cells. The salt concentration of all the electrolytes is 1M $NaPF_6$.

The distribution of sodium in the first cycle was analysed by the isotopic titration method and the results were shown in Figure 5.7. The measurements showed that 42% Na was consumed to form dead Na and 34% Na was consumed to form the SEI in the EC: DMC electrolyte cell, while just 3% Na was consumed to form dead Na and SEI in the glyme electrolyte cell in the first cycle. Including additives in the carbonate electrolyte decreased the Na lost to dead Na significantly, but not to the degree found for the glyme electrolyte. There was 10% Na consumed to form dead Na and 21% Na was consumed to form SEI in 10% VC additive carbonate electrolyte. While there was 7% Na consumed to form dead Na and 19% Na consumed to form SEI in 10% FEC additive carbonate electrolyte. They were also less effective in preventing Na loss to SEI formation. The total Na consumed into the SEI for the EC: DMC solvent cell was ten times more than the glyme electrolyte cell. These results suggested that the carbonate solvent electrolytes yield thicker SEIs, consuming more Na in the SEI formation. This was supported by the EIS (Figure 5.6), with the carbonate electrolyte resistance measurement roughly seven times higher, as the formation of a thicker SEI layer would be expected to impede transport.

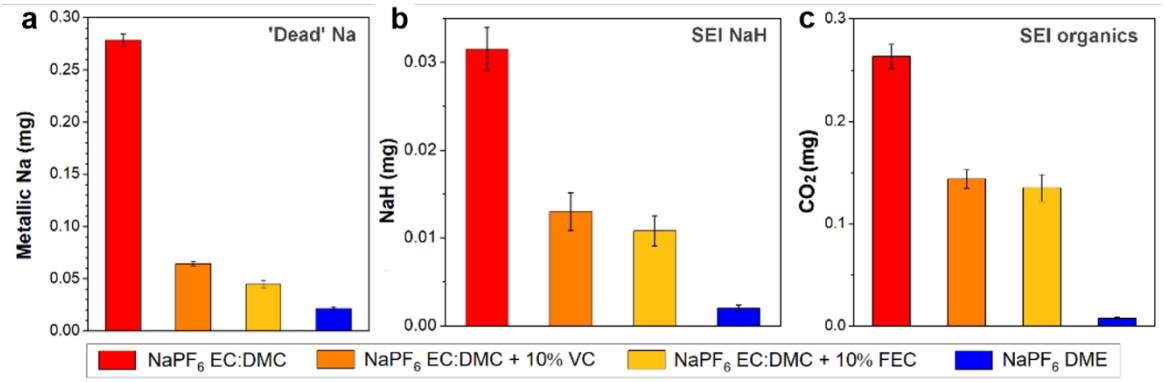


Figure 5.8. Quantitative online-MS measurements of (a) dead Na, (b) NaH, and (c) CO2, the signature of organic SEI components such as $(CH_2OCO_2Na)_2$ and $NaOCO_2R$. The deposition capacity at 0.5 mA cm^{-2} for 0.5 mAh cm^{-2} for all the Na||Cu coin cells. The salt concentration of all the electrolytes is 1M $NaPF_6$.

In addition, the dead Na, sodium hydride (NaH), and some organic species such as $(CH_2OCO_2Na)_2$ and $NaOCO_2R$ (we will refer to them as 'organic carbonates' here) could be quantitatively measured. As shown in Figure 5.8, a greater quantity of dead Na, NaH, and organic carbonates was found for the carbonate electrolytes, with their amounts correlated with the battery's coulombic efficiency. The 'Dead' sodium formation was understood to largely arise due to the uneven dissolution of dendritic electroplated structures, leading to metal detachment from the electrode and subsequent electrical isolation.[21] The online-MS results suggest the ether electrolyte suppresses dead sodium formation, which may be because of the uniform deposition. Interphase NaH forms by the reaction of sodium metal with hydrogen gas (or some sodium-based hydrated compounds),[230] and has been suggested to hinder Na^+ ion transport at the electrode interface.[128] The measured organic SEI products can further decompose into inorganic Na_2CO_3,[231] which has been shown to be unstable when exposed to sodium electrolytes.[222] Thus the comparatively high quantities of NaH and Na organics found in the carbonate electrolyte SEIs support the poor electrochemical performances measured for them; the NaH will contribute to the insulating character of the SEI (Figure 5.6), and the organics will lead to continued SEI dissolution and replenishment and thus contribute to the sustained low CE (Figure 5.1) and high cumulative SEI product formation.

In addition, the cumulated dead Na, NaH, and organic carbonates were measured after the third cycle for all four electrolytes (as shown in Figure 5.9). It showed that around three times the mass of dead Na, four times NaH, and two times of organic carbonates were cumulated for EC: DMC compared to the first cycle, while the increase for glyme was marginal. These demonstrated that the SEI formed in EC: DMC was unstable, leading to continuous uncontrolled dead Na generation and electrolyte decomposition. While for ether

SEI, once created, it was relatively stable and remains little changed upon subsequent cycling.

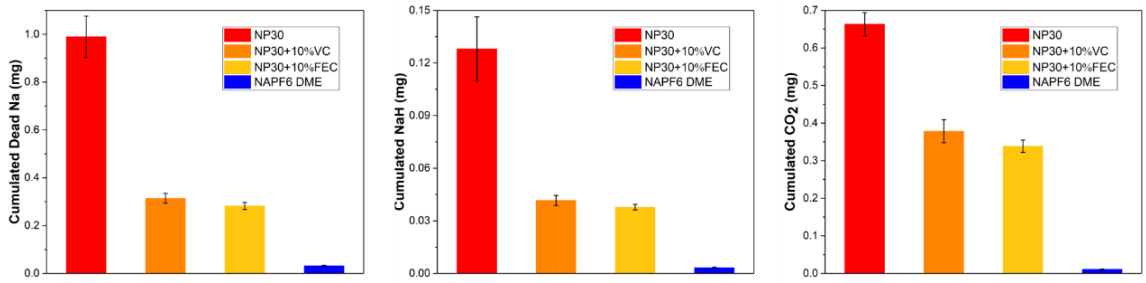


Figure 5.9. Quantitative online-MS measurements of dead Na, NaH, and CO_2 signature of organic carbonates SEI components such as $(CH_2OCO_2Na)_2$ and $NaOCO_2R$ after the third cycle. All the cells are plated at 0.5 mA cm^{-2} to 0.5 mAh cm^{-2}, and stripped to 1 V for 3 cycles. The concentration of 1 M $NaPF_6$ salt for all electrolytes.

5.2.2 Operando liquid TEM characterization

The mass spectrometry measurements demonstrated that ether electrolyte limits 'dead' Na formation, implying that it inhibits dendritic Na morphologies that are more prone to detachment and isolation. To verify this, operando electrochemical liquid-cell TEM was performed to study the Na dynamic electroplating/stripping process onto a Pt working electrode (WE) from a liquid electrolyte environment with galvanostatic electrochemical cycling (Figure 5.10 and Figure 5.11). The contrast mechanism in TEM is largely dependent on the relative densities of the imaged structures;[169] and unfortunately the Na is hard to distinguish due to its similar density to the surrounding electrolyte (as shown in Table 5.1).[169] Both the density of Na and electrolyte are around 1 g cm^{-3}.

	Li	Na	LiPF6 in EC/DMC	NaPF6 in EC/DMC	CO2	H2
Density (g/cm^3)	0.53	0.968	1.3	1.32	0.002	0.0009

Table 5.1. Densities of metals, gases, and electrolytes relevant to the reported liquid-cell TEM experiments.

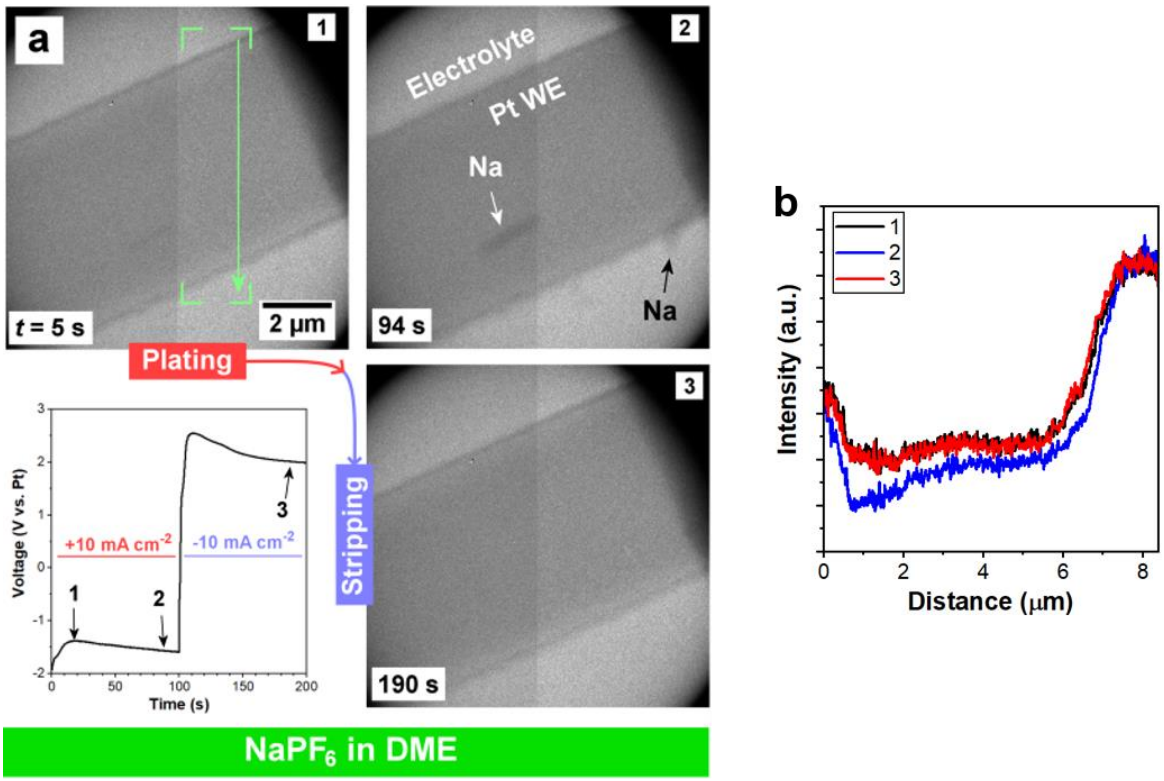


Figure 5.10. Operando electrochemical liquid-cell TEM imaging of Na plating/stripping in glyme electrolyte. (a) Galvanostatic cycle (10 mA cm^{-2}) of $NaPF_6$ in DME. Annotation in panel 1 denotes where box-averaged intensity profiles were acquired from each panel. (b) Intensity profiles extracted from panels 1 to 3.

Although the delineation of deposited metal morphologies was challenging due to the low contrast between deposited Na and electrolyte, particularly in the case of the ether electrolyte. However, careful examination of the complete electroplating and stripping process from the ether electrolyte revealed a largely uniform deposition and dissolution of sodium as shown in Figure 5.10. For the glyme electrolyte, the Na was seen to be deposited uniformly and stripped fluently and no bubble formation was observed indicative of side reactions. The change in intensity due to sodium plating and stripping is confirmed by box-averaged intensity profile measurements extracted from the three frames (as shown in Figure 5.10b). Alongside the largely uniform plating over the WE surface, two-micron-sized Na structures can be seen to deposit and dissolve, as indicated with arrows in Figure

5.10a, panel 2. The largely flat morphology of the plated Na supports the online-MS measurements, as flat plating and uniform stripping will preclude any 'dead' Na detachment.

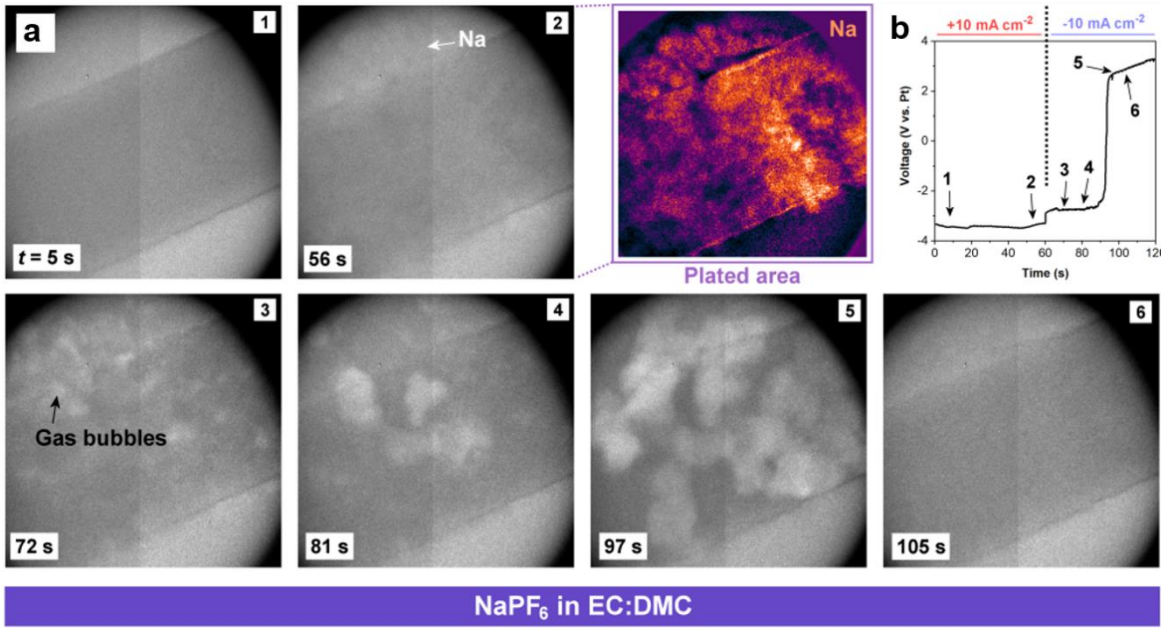


Figure 5.11. Operando electrochemical liquid-cell TEM imaging Na plating/stripping in $NaPF_6$ in EC: DMC electrolyte. (a) The sodium plating and stripping evolution process under the galvanostatic cycle (10 mA cm^{-2}). Insert is false-color of panel 2 following background subtraction, highlighting Na deposition. (b)The corresponding galvanostatic electrochemical diagram.

The observed cycling behavior with a carbonate EC: DMC electrolyte was distinct (Figure 5.11). To highlight the areas where plating occurred, background subtraction and a false-color look up table were applied to Figure 5.11, panel 2, suggesting a looser deposited sodium structure. However, the low relative contrast of deposited Na made comparison with the glyme plating structure difficult. During the stripping process, many localized bubbles were generated around the plated Na and near the electrode (white regions, Figure 5.11, panels 3-5). These small gas bubbles rapidly nucleated on the Na metal surfaces, grew, and eventually dissolved into the electrolyte. Following the completion of the galvanostatic

cycle, moving the stage revealed the growth of a large bubble. This indicates that gas evolution from the cycling process had been sufficient to overcome the saturation limit of the electrolyte in the liquid-cell, leading to degassing/gas accumulation into the large bubble. The excessive bubble formation during stripping, localized directly on the plated Na, while no such effervescence was observed for the ether electrolyte, presents a possible mechanism for the difference in their cycling performances; bubble formation at the stripping interface physically displaces the electrolyte away from the electrode and may damage the SEI, thus will impede uniform dissolution of the plated Na and lead to the lower CEs exhibited by the carbonate electrolytes. A control experiment was performed to test the beam effect in Figure 5.12, suggesting that bubble formation was unrelated to the beam damage.

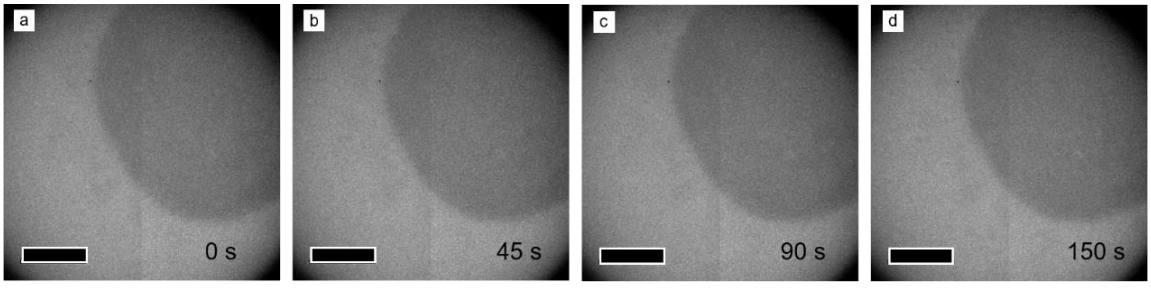


Figure 5.12. A control experiment testing the beam effect in TEM mode. This is performed under the same conditions as the cycling experiments, except with no external bias applied to the working electrode. TEM imaging an area of plated Na in NaPF6 EC: DMC electrolyte for 0s (a), 45s (b), 90s (c), 150s (d). There is no bubble formation within the 150s, suggesting the bubble formation and other side reactions are not caused by beam damage. Scale bars are 1 μm.

5.2.3 Post-mortem SEM characterization

To see the deposited Na morphology on a large scale, SEM was used to characterize the cycled working electrodes used in the operando TEM experiments in Chapter 5.2.2. The working electrode chip was dismantled in the glovebox and was transferred into SEM air-

tight holder. Due to the deposited Na and SEI being air-sensitive, the whole process is air-tight. The SEM images of the disassembled cell after the in-situ TEM experiment for $NaPF_6$ in DME were shown in Figure 5.13, there were only a few dead sodium pieces. By contrast, lots of dead sodium were observed in the cycled electrode of NaPF6 in the carbonate electrolyte, as shown in Figure 5.14. These dead sodium pieces seemed to be very dendritic.

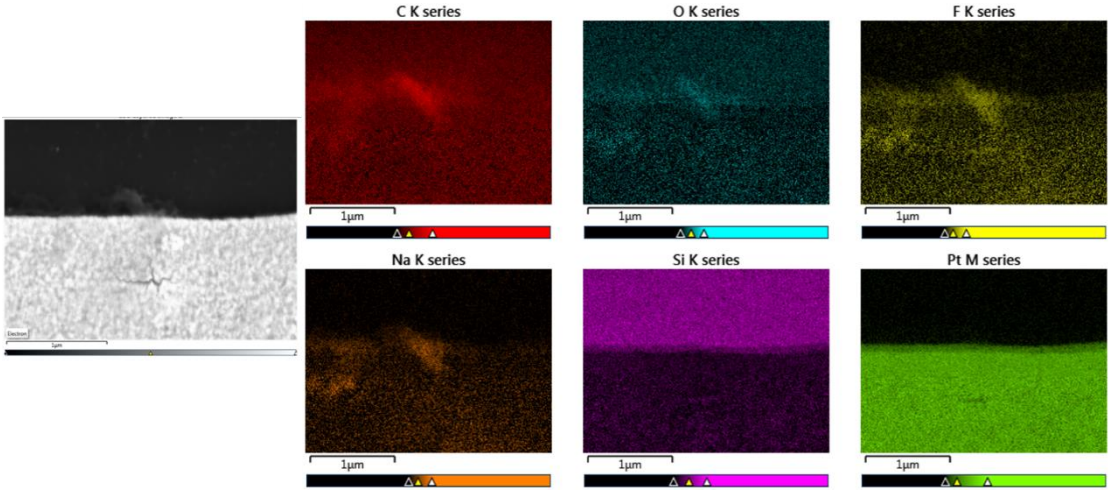


Figure 5.13. SEM image of the disassembled cell after an in-situ TEM experiment for $NaPF_6$ in DME.

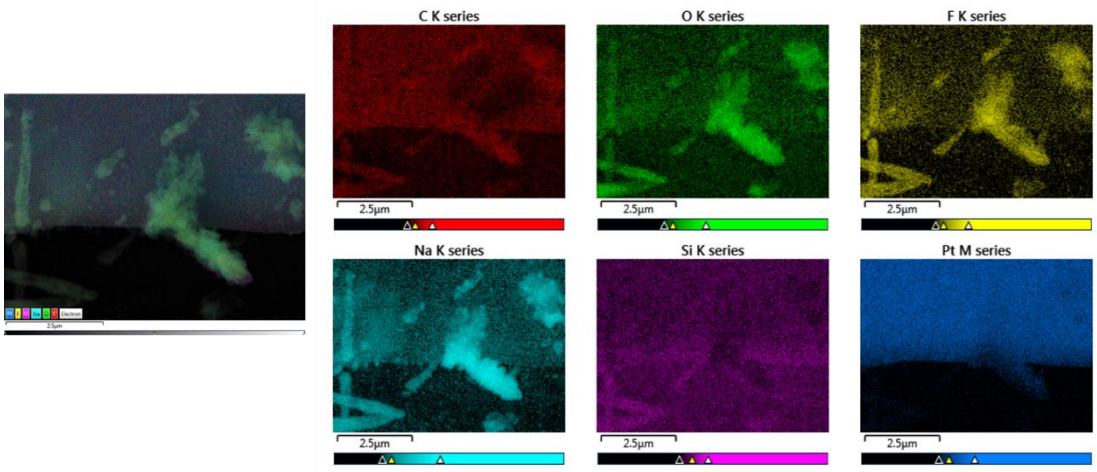


Figure 5.14. SEM image of the disassembled cell after an in-situ TEM experiment for $NaPF_6$ in EC/DMC.



Figure 5.15. Image of the plated Na in carbonate cell and ether cell after disassembling coin cell in the glove box. The top coin cell is cycled in EC:DMC electrolyte, and the bottom coin cell is cycled in DME electrolyte.

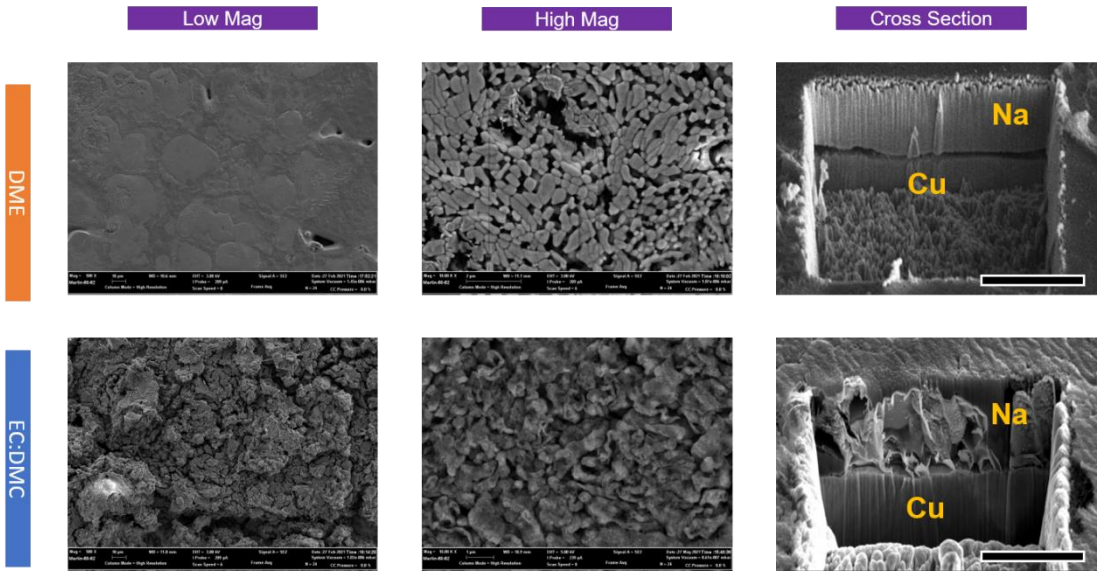


Figure 5.16. SEM images of the plated Na in carbonate cell and ether coin cells. FIB performed cross-sectional images, showing the deposited Na in ether cell is much denser. Scale bars are 10 μm for cross-section images.

To verify whether they have morphology differences in coin cell level, a comparison of deposition structure following electroplating (deposition capacity at 0.5 mA cm^{-2} for 5 mAh cm^{-2}) was performed in the coin cells. After disassembling the plated Na coin cells in the glove box, the image of the deposited Na in DME was uniform and shiny, while the

deposited in EC: DMC was loose and porous (as shown in Figure 5.15). The SEM imaging and FIB cross-sectioning further confirmed the more dendritic and looser morphology of the Na plated from carbonate electrolyte (as shown in Figure 5.16). The deposited Na in the DME electrolyte was dense and uniform. By contrast, the deposited Na in the carbonate electrolyte was very loose. The porous structure of deposited Na in carbonate electrolyte may cause by the trapped gas in SEI shells, which is consistent with the operando TEM results.

5.2.4 Operando liquid STEM characterization

To further explore the localized bubble formation in the carbonate electrolyte system, operando electrochemical HAADF STEM was performed on cyclic voltammetry cycled $NaPF_6$ in EC: DMC with 10%FEC electrolyte (as shown in Figure 5.17). The carbonate electrolyte with FEC additive was studied because it has been shown to limit gas formation, and so represents the 'best case' carbonate electrolyte.

The HAADF-STEM is a dark field imaging technique, as such the contrast is inverted compared to TEM imaging; i.e., low-density features like gas bubbles are dark and high-density features like the Pt WE are bright. With the voltage going down during CV, faint Na deposits can be initially distinguished in Figure 5.17b (pointed by white arrows). The bubble was also observed in the field of view in the black area of the upper left corner in Figure 5.17b. Honestly, it is hard to distinguish the edge of SEI here, because the electrolyte and Na have similar contrast in this HADDF-STEM image. The edge of the bubble could be also formed between the electrolyte and the bubble. To observe the edge of the bubble, the field of view in this experiment was moved, which was shown in Figure 5.17h and Figure 5.18. A bubble can be seen to form away from the electrode, showing that gas

formation occurs throughout the cycle. Between the electrode and the bubbles, there were some deposited Na with SEI structures which were all immersed in the electrolyte.

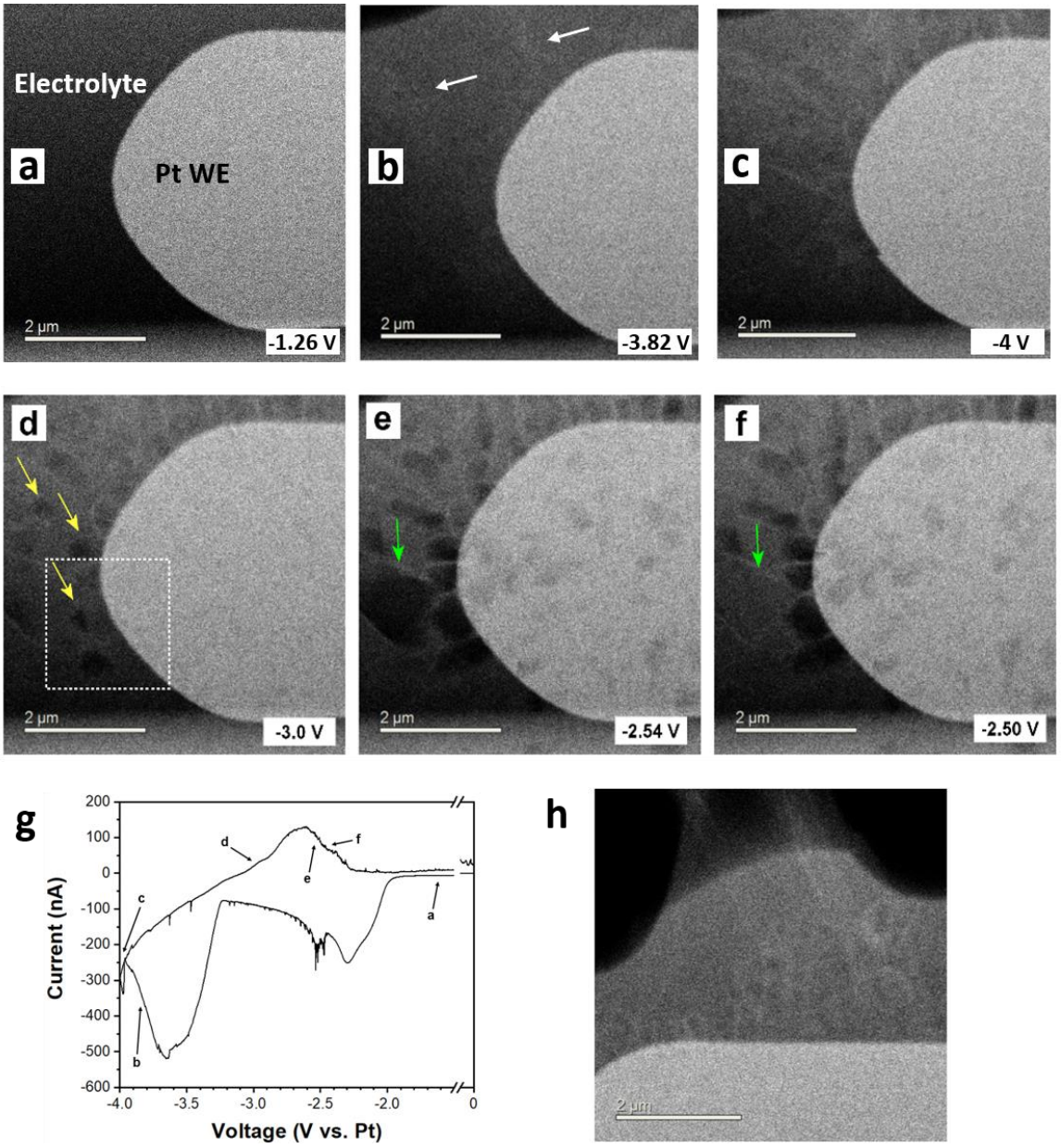


Figure 5.17. Operando electrochemical HAADF-STEM imaging of bubble formation from 1 M $NaPF_6$ in EC: DMC with 10%FEC. (a-f) Liquid-cell STEM time-series of cyclic voltammetry cycling. (g) The corresponding CV profile of (a-f). (h) Selected an image from the plating process to show the edge of the bubble.

With plating time going on, the contrast of Na was increased in (Figure 5.17c), which meant more Na is deposited. The contrast between metallic Na and the surrounding solvent was low due to the close relative densities, yet the dynamic deposition was observable in the real-time movie which was shown in my published paper.[232] However, once the electrostripping stage of the cyclic voltammetry sweep started, some small bubble formation localized at the Na metal surfaces was once more observed (Figure 5.17d, yellow arrows). Interestingly, these bubbles were seen to grow toward the working electrode during the Na stripping process, expanding to fully occupy the spaces in which Na deposited areas before. Because once the Na was deposited, the SEI would be formed at the edge of Na and electrolyte. The Na electrostripping process and the bubble movement behaviors revealed that there are apparent SEI shells left behind. These SEI shells were delaminated from the retreating sodium metal and then occupied by the growing bubbles during stripping. Some localized bubbles eventually dissipated (Figure 5.17e and f, green arrows), presumably through gaps in the SEI shell. Only bubbles can appear and disappear suddenly, it further indicated the black objects were bubbles.

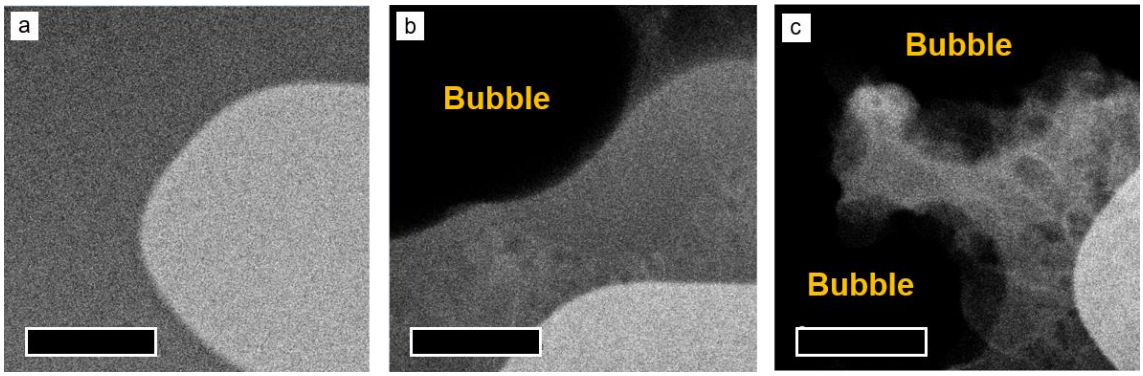


Figure 5.18. A large bubble was observed growing beside the working electrode. The gas bubble forms once CV starts, and continually grows during cycling. Scale bars are 2 μm.

To clearly present the bubble growing process in SEI shells during the Na stripping process, the magnified views of the bubble formation process were picked from the white dotted

square in Figure 5.17d-f. As shown in Figure 5.19a, the bubbles were grown toward the electrode in the same direction as sodium stripping. Thus, it was reasonable to infer that the SEI shells were still there after sodium stripping. The localized formed bubbles in this process occupied the SEI shells gradually. It is important to note that it is not possible to reliably distinguish between Na metal and electrolyte inside the SEI shell (darker blue in Figure 5.19b) due to their similar contrast, thus liquid electrolyte may be entering the SEI shell following Na dissolution, with the growing gas bubbles subsequently displacing it. Some brighter streaks in the SEI were observed, such as in Figure 5.17h and Figure 5.19a. These brighter streaks seemed to form at the edge of deposited sodium and especially occurred in the SEI shells. Due to brighter contrast in the STEM-HAADF mode means heavier density, these brighter streaks are probably inorganic SEI such as Na_2CO_3 (with a density of 2.53 g cm^{-3}) and Na_2O (with a density of 2.27 g cm^{-3}).

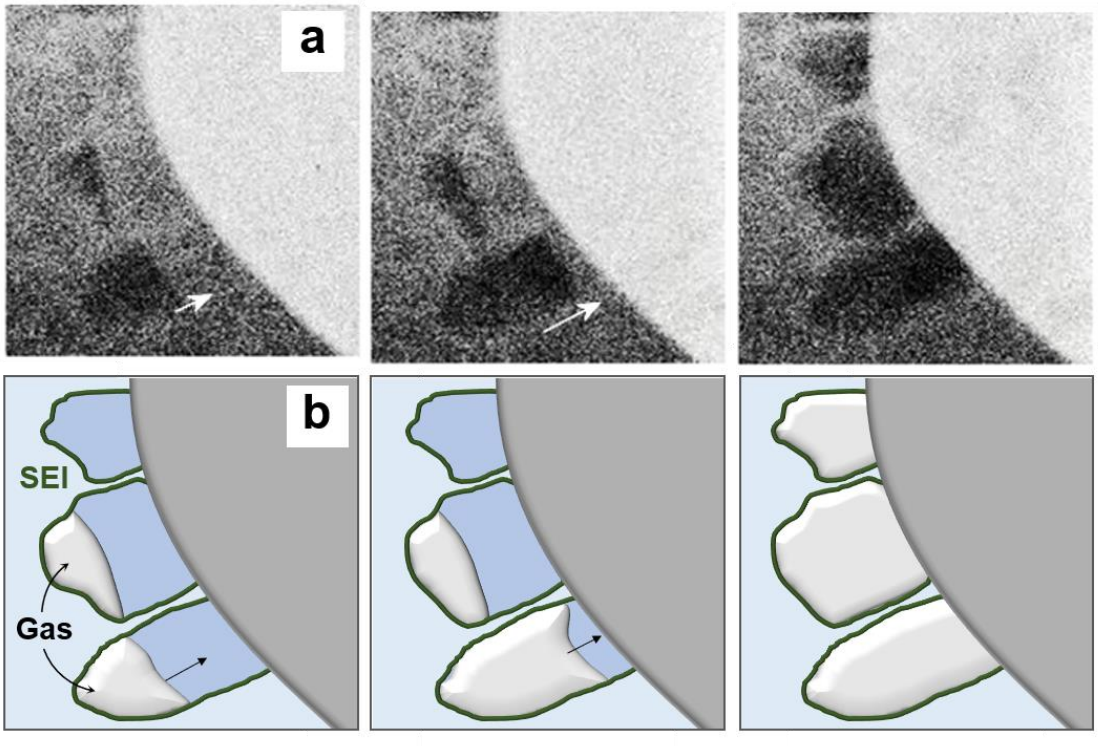


Figure 5.19. The magnified views show bubble formation during the stripping process. (a) The bubble formation process which picking from the white dotted square in Figure 5.17d-f. (b) Illustrations corresponding to (a).

That the SEI shells remain protruding from the surface following stripping suggests an SEI with less elasticity form from carbonate electrolyte. Such mechanical properties mean that the SEI cannot easily maintain conformity with the retreating metal; the SEI does not follow the electrode's expansion and contraction through the electroplating and stripping cycle but rather remains at the maximum extent. This may be aided by interceding gas bubbles delaminating the SEI away from the Na metal as it is stripped. The observed detachment would necessitate the SEI to be reformed every cycle, as new Na deposition would be left exposed to the electrolyte, which would explain the sustained capacity loss to SEI formation over repeated cycling experienced by carbonate electrolytes (Figure 5.7).

5.2.5 Ex-situ AFM characterization

To further study the morphology of plated Na, the topography of Cu working electrodes that cycled in Na||Cu coin cells were studied by AFM. In order to better describe the flatness of the sample surface, 'roughness' is introduced in the AFM measurement. During AFM measurement, the relative height of each location can be detected and corresponding data is formed at each detection point. The roughness in this experiment is used to describe the deviation of a surface from a mean height. Therefore, every location has its own roughness in a figure, and the roughness in a figure is the arithmetic mean of all the roughness numbers. The standard deviation of all the roughness numbers is the corresponding error bar in this experiment.

As shown in Figure 5.20, the morphology of the plated sodium on the working electrode of the glyme electrolyte was smooth and uniform. The surface roughness of deposited sodium was around 26 ± 5 nm and decreased to 6 ± 2 nm after stripping. However, the deposited

sodium in the carbonate electrolyte was highly heterogeneous, forming rough sodium metal spikes/islands on the electrode (as shown in Figure 5.21). The plated Na metal demonstrated an ununiform shape with a roughness of 208 ± 26 nm in carbonate electrolyte, which is considerably higher than the roughness in glyme electrolyte. After subsequent stripping, the roughness decreased to 32 ± 8 nm for the carbonate electrolyte, which was still significantly higher than the glyme electrolyte. This result verified the excellent flat plating morphology of the deposited sodium in the glyme electrolyte, which is consistent with the operando TEM and post-mortem SEM results. This flat morphology will be robust toward detachment, and thus supports the low quantities of measured 'dead' Na lost with glyme electrolyte (Figure 5.7).

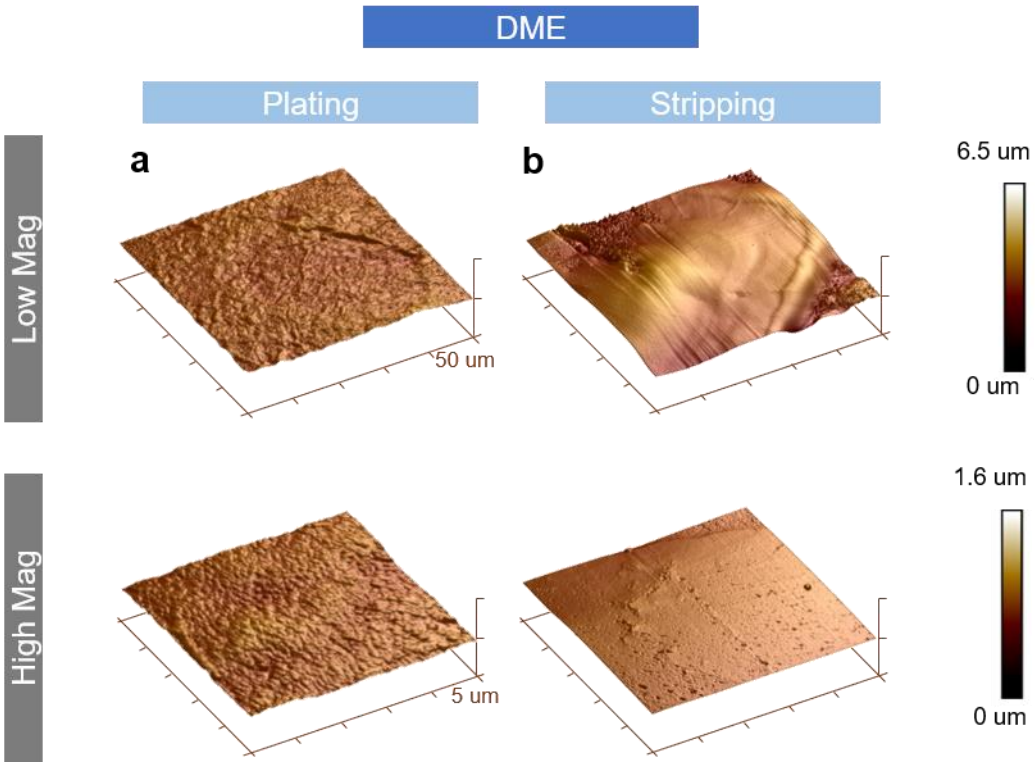


Figure 5.20. AFM imaging and measurement of deposited/stripped sodium. AFM images of Cu electrodes galvanostatically cycled (plating at 0.5 mA cm^{-2} for 0.5 mAh cm^{-2}) in glyme solvent Na electrolytes, imaged following (a) electroplating and (b) stripping. The color scale indicates the height. The AFM experiment and data analysis are performed by Shengming Zhang and me.

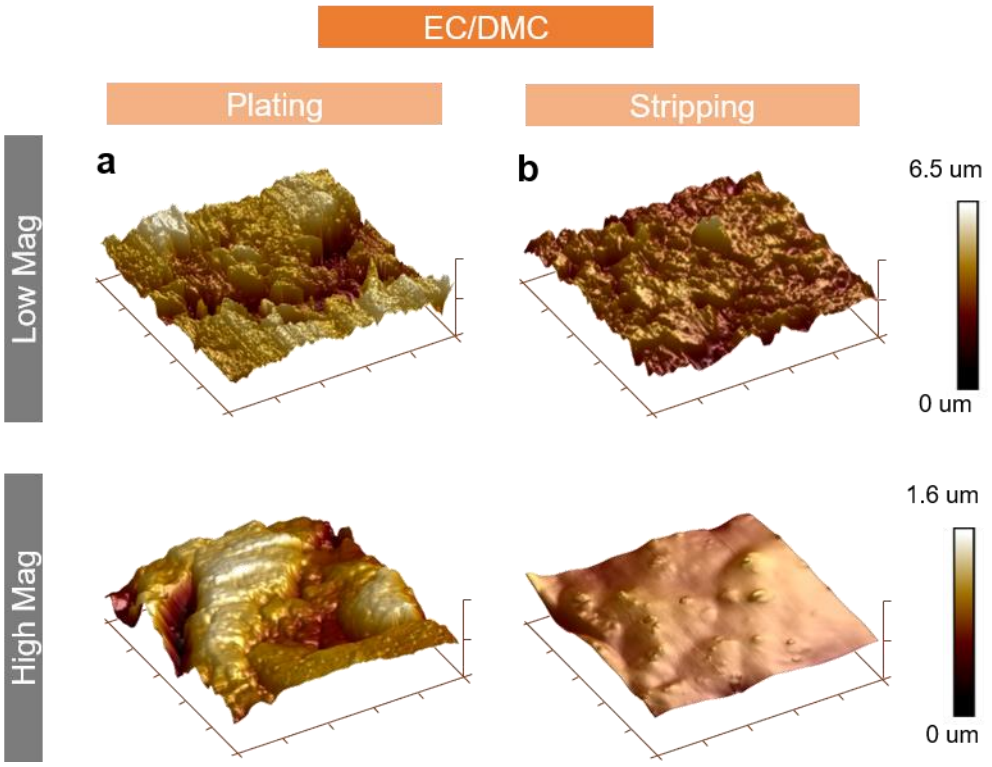


Figure 5.21. AFM imaging and measurement of deposited/stripped sodium. AFM images of Cu electrodes galvanostatically cycled (plating at 0.5 mA cm^{-2} for 0.5 mAh cm^{-2}) in carbonate solvent (EC: DMC) Na electrolytes, imaged following (a) electroplating and (b) stripping. The color scale indicates the height. The AFM experiment and data analysis are performed by Shengming Zhang and me.

Furthermore, AFM indentation was performed to measure the mechanical properties of SEI, because the SEI was believed to govern the Na deposition morphology and the degree of electrolyte decomposition. As shown in Figure 5.22, it revealed the mechanical properties of the SEI formed from the two electrolyte systems on Na metal. The samples were cycled 10 cycles in both electrolytes, so the SEI should be enough to be characterized. The mechanical nanoindentation experiments were conducted in a 5 um * 5 um region with over 100 points evenly disturbed in the field of view of cycled electrodes. A low PeakForce setpoint (20 nN) was first used to avoid permanent damage to the SEI film and to measure Young's modulus of the SEI in the elastic region. Subsequently, a higher PeakForce

setpoint (350 nN) was deliberately used to break the SEI and record the force-response curves from nanoindentation as shown in Figure 5.22a and Figure 5.22b.

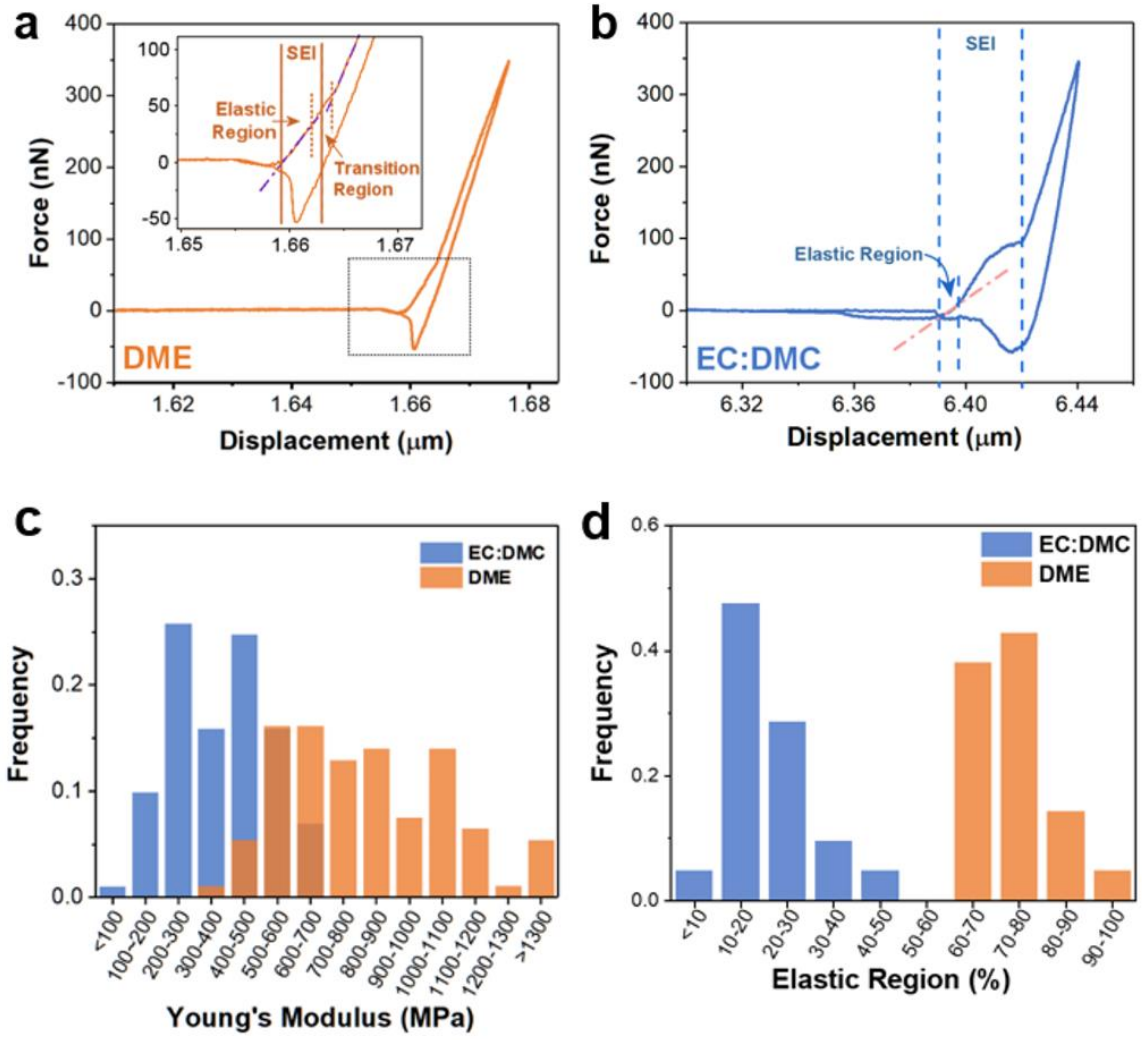


Figure 5.22. Measured mechanical properties of the SEIs formed on electroplated Na metal after ten cycles. (a,b) Representative force-displacement curves of the electrode surface after electroplating from ether and carbonate solvent electrolytes onto Cu current collectors (plating at 0.5 mA cm^{-2} for 0.5 mAh cm^{-2}). A low PeakForce setpoint (20 nN) was first used to avoid permanent damage to the SEI film and to measure Young's modulus of the SEI in the elastic region. Subsequently, a higher PeakForce setpoint (350 nN) was deliberately used to break the SEI and record the force-response curves from nanoindentation. As the AFM probe tip approaches the sample surface, the started lower gradient line represents the force response from the SEI film generally followed by a higher gradient line from the Cu substrate. The percentage of the elastic region for the SEI film is defined as the ratio of the thickness of the elastic region to the total thickness of the SEI film which also includes the plastic region. (c) Young's modulus and (d) elastic region distributions of the SEI layer on the electroplated electrodes from ~100 measurements.

For details, as the AFM probe tip approaches the sample surface, the started lower gradient line represents the force response from the SEI film (as shown in Figure 5.22 a&b). After the SEI fracture, the probe tip approaches sodium or Cu metal, it will show another higher gradient line in the Figure. Therefore, the thickness of the SEI part can be measured. In the glyme electrolyte experiment as shown in Figure 5.22a, the force-response curve shows two straight segments of different gradient lines in the SEI part, which are the linear elastic part and non-linear elastic part, respectively. As we all know, the elastic region presents a linear line in the relations between force and displacement. The percentage of the elastic region for an SEI film in this experiment is defined as a ratio of the thickness of the elastic region to the total thickness of the SEI film, which also includes the plastic region. However, for the carbonate electrolyte, the force-response curve in Figure 5.22b shows a clear change of gradient from high slope to low slope, indicating the elastic-to-plastic transition, which we see pretty easily for DMC but not DME.[226] Derjaguin-Muller-Toporov (DMT) model fitted the force response curves to calculate Young's modulus. This methodology has been widely used to characterize the mechanical of the SEI.[233] The mechanical data from over 100 site measurements are statistically summarised in Figures 5.22c and 5.22d. Young's modulus of SEI in glyme electrolyte is much higher than the SEI in carbonate electrolyte, confirming that the SEI formed from glyme electrolyte is more rigid and stiffer. In addition, the SEI of glyme electrolyte has a larger elastic region, which has better mechanical stability for the sodium volume expansion during plating and stripping.

In this project, a ratio of the thickness of the elastic region to the total thickness of the SEI film is used to describe the ability of elasticity of an SEI film. Because the SEI is formed once the sodium deposition in the electrolyte, the elastic region of SEI is responsible for being tolerant to the volume expansion upon fresh sodium deposition. If most of the SEI is

a plastic region, the SEI is easy to be broken even if the SEI is thick. Therefore, from Figure 5.22c &d, we can learn that the stiffer and good elastic performance of the ether electrolyte SEI and the more brittle character of the carbonate electrolyte SEI, which is in good agreement with similar experiments performed recently on Sn anodes.[226] The less elastic SEI formed from the EC: DMC electrolyte may be attributed to the larger amount of carbonate ester ($NaOCO_2R$) and brittle inorganic components (NaH and Na_2CO_3) formed, as seen in the mass spectrometry measurements (Figure 5.8). These measured mechanical properties support the liquid-cell STEM observations, with the non-conformal SEI seen to rigidly remain following the Na electrostripping in carbonate electrolyte.

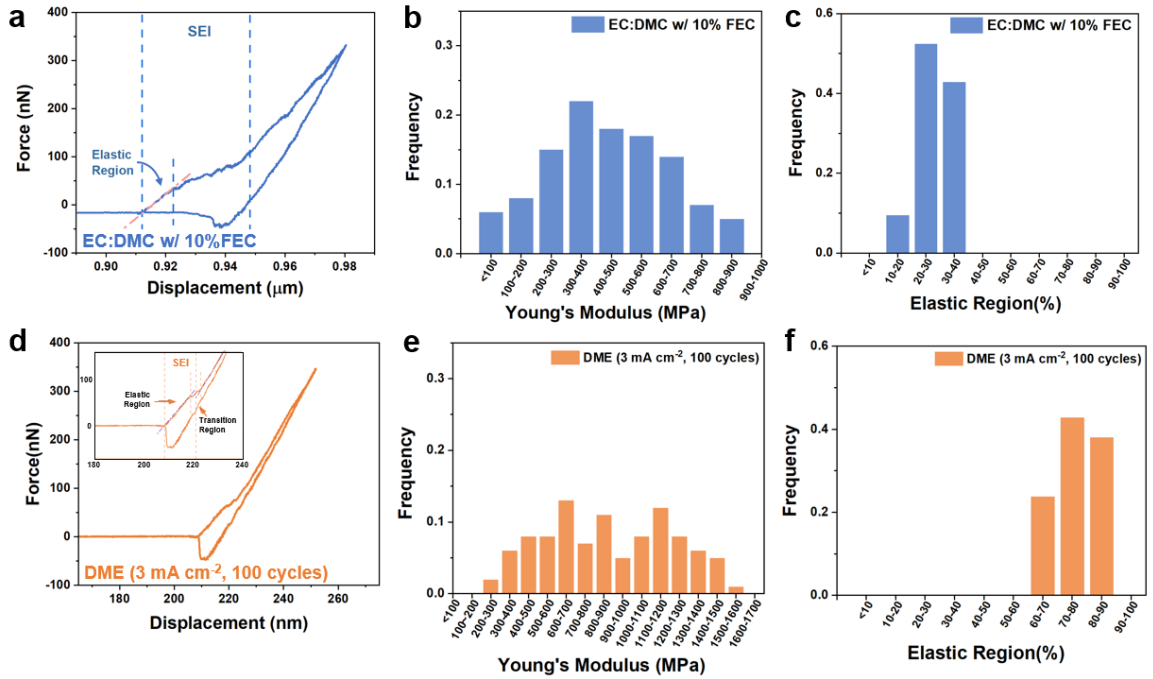


Figure 5.23. Measured mechanical properties of the SEIs formed on electroplated Na metal after ten cycles (EC: DMC with 10% FEC) and 100 cycles (DME at high rate cycling). (a,d) Representative force-displacement curves of the electrode surface after electroplating from EC: DMC solvent with 10% FEC additive, and DME at high current density (3 mA cm^{-2}) and for 100 cycles, respectively. (b,e) Young's modulus and (c,f) elastic region of the SEI layer on the electroplated electrodes for the EC: DMC with FEC additive and high rate DME,

To further understand the additive effects of SEI in carbonate electrolyte, additional AFM mechanical measurements were performed to characterize the mechanical properties of the SEI for 1 M $NaPF_6$ in EC: DMC with 10% FEC electrolyte (as shown in Figure 5.23a-c). All the same experimental parameters were performed (such as both 10 cycles at 0.5 mA cm^{-2} to 0.5 mAh cm^2). Comparing these to the existing data from EC: DMC without FEC additive (Figure 5.22), there is a somewhat larger elastic region and modestly higher Young's modulus, however, it remains much less than in both cases to what we measured for Na plated from DME. This suggests a similar, but less effective, mechanism may occur with FEC additive, with the FEC enhancing cycling performance by improving the interphase elasticity.

The electrochemical behaviour of sodium plating/stripping in glyme electrolyte is also excellent as shown in Figure 5.4 and Figure 5.5. To confirm the mechanical properties of SEI at high current density in glyme electrolyte, the AFM measurements were performed to study the SEI properties at a current density of 3 mA cm^{-2} from ether electrolyte. The additional force-displacement curve, Young's modulus, and elasticity measurements are presented in Figure 5.23d-f. The distribution of Young's modulus measurements is similar, with a somewhat increased tail of Young's modulus at the high end (above 1100 MPa) compared to the originally reported 0.5 mA cm^{-2} current density results (in Figure 5.22c). It also shares a similar elastic region distribution. This confirms the mechanical stability of the ether-derived SEI remains robust to higher current densities and for repeated cycling.

5.2.6 In-situ AFM characterization

The uniform sodium deposition was shown in Figure 5.20 by characterizing the disassembled coin cell electrode. To further directly image the sodium deposition process

in real-time, the in-situ liquid-cell AFM was designed to gain the sodium evolution during electroplating. The same Cu foil was used as the working electrode, a concentric ring of Na metal was used as the counter electrode, and a flake of Na metal on the Cu wire was used as the reference electrode in this experiment. The cell was connected to the Gamry potentiostats to plate Na onto the Cu working electrodes electrochemically, which the in-situ setup as illustrated in Figure 3.7. The pristine morphology of Cu foil under liquid electrolyte was captured and compared to an identical scan performed in the air, verifying the morphology and capture resolution excluding any side effects from liquid electrolyte (as shown in Figure 5.24).

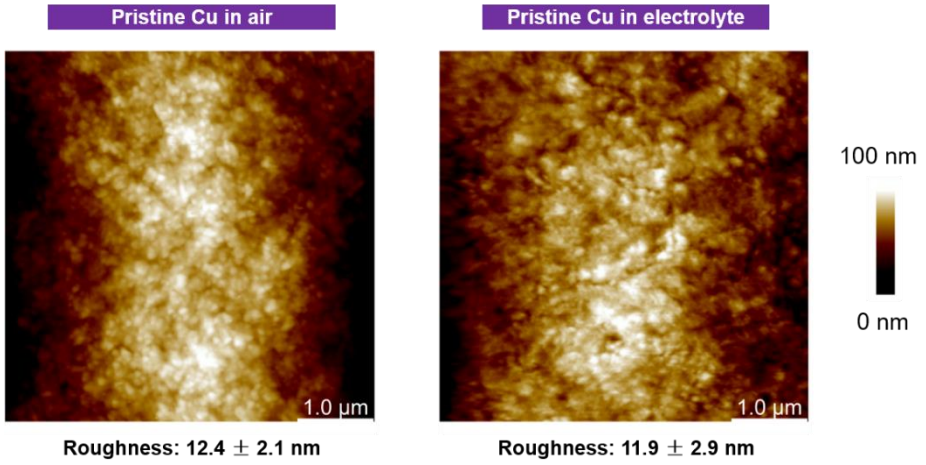


Figure 5.24. AFM Images of pure Cu current collector in air and electrolyte. The pristine Cu foil morphology is characterized under an identical scan performed in the air and electrolyte, verifying the morphology and capture resolution excluding any side effect from the liquid electrolyte. The roughness of Cu in the air is 12.4 ± 2.1 nm, and the roughness of Cu in the electrolyte is 11.9 ± 2.9 nm.

The topography of the working electrode was captured during plating from the ether electrolyte at a current density of 0.5 mA cm^{-2} (as shown in Figure 5.25). After 600 s of

plating, Na metal was evenly distributed on the Cu working electrode. With further plating to 1200 s, Na metal was observed to grow at lower sites, highlighted by dashed yellow regions, which were further away from the counter electrode. The same phenomenon was also observed toward the end of plating (the 1800s), where the regions labeled by dashed blue curves again demonstrated growth of Na metal at lower sites.

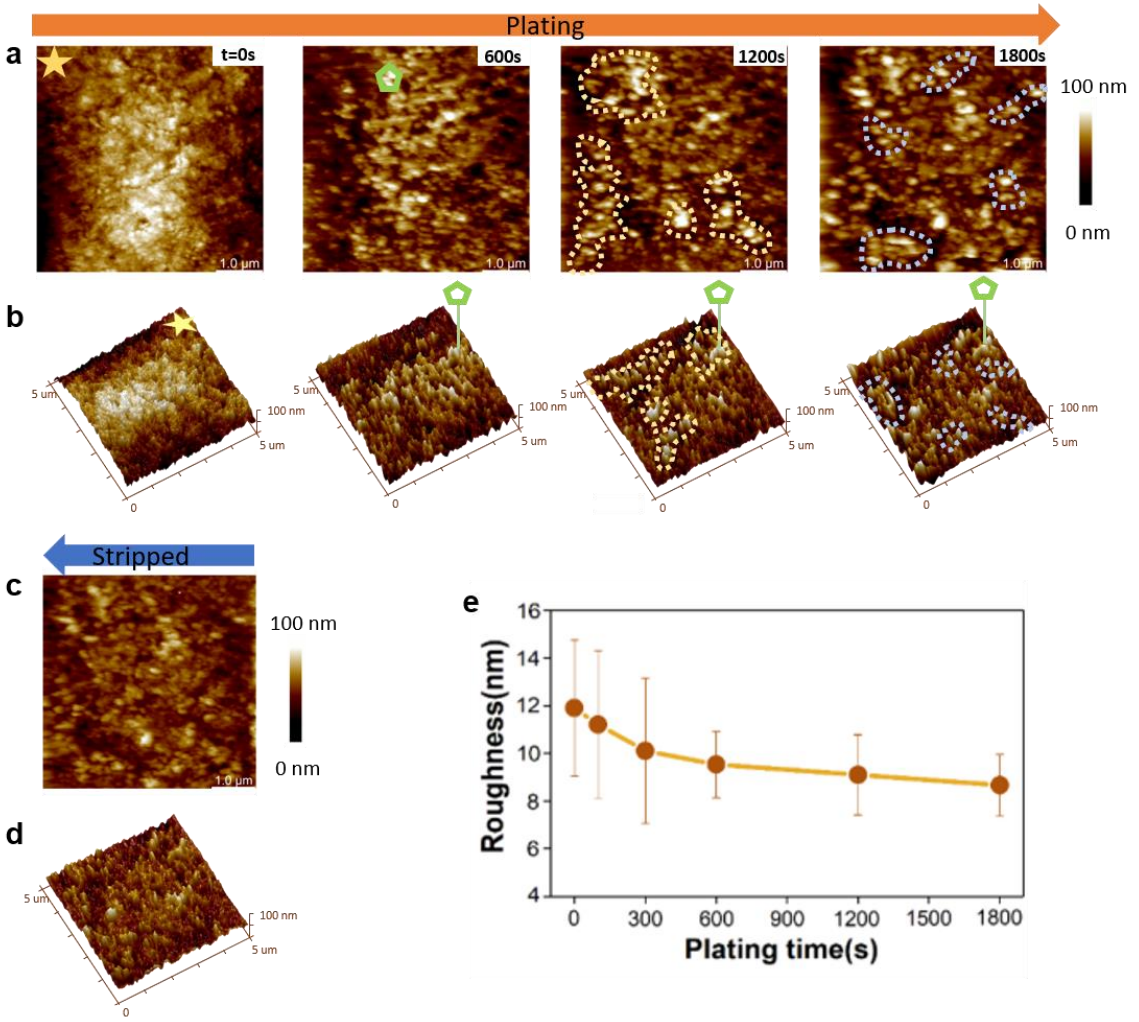


Figure 5.25. In-situ liquid-cell AFM topography of galvanostatic cycling from 1 M $NaPF_6$ in DME. (a) AFM image time-series of the Cu WE during Na electroplating at 0.5 mA cm^{-2}. (b) Perspective views of the images in (a). (c) The Cu WE after galvanostatic stripping to 1V. (d) Perspective views of the images in (c). (e) Change in electrode roughness with electroplating time. The AFM experiment and data analysis are performed by Shengming Zhang and me.

The tendency of Na deposition to preferentially occur at lower sites is reflected in the decreasing surface roughness measured over the course of the plating cycle (Figure 5.25e), suggesting that the deposition dynamics from ether electrolyte maintain the smoothness of the electrode surface and crucially avoid the formation of Na protrusions that may act as focal points for dendritic growth. This electroplating behavior is unexpected, as deposition should typically occur at protrusions rather than recesses due to the higher local electric field, leading to dendrite growth.[193,234] The smoothness of the electrode was found to be maintained after stripping (Figure 5.25c), with a roughness of 7.1 ± 2.1 nm, confirming the good stripping performance with ether electrolyte.

A possible explanation for this unusual recess deposition mechanism may be the combination of the ether SEI's mechanical properties and its good ionic conductivity. With a higher Young's modulus and a wider elastic region of the SEI formed from the ether electrolyte, a greater compression on Na can be maintained without breakage of the SEI. The compressive stress has been modeled to have a suppression effect on the deposition kinetics by shifting the electrochemical potential at the interface.[139] Such suppression of deposition kinetics would be the strongest at the tip of any deposited Na, where the elastic deformation from compressive stress would be the largest, leading to Na deposition at the valleys, as seen in the in-situ AFM results (Figure 5.25). The SEI layer formed from the ether electrolyte was also significantly thinner, as evidenced by previous online-MS results (Figure 5.7 and Figure 5.8), which identified that the Na consumed to form SEI from the EC: DMC electrolyte was ten times more than for the ether solvent in the first cycle. This thinner SEI ensured faster Na^+ transport across it compared with that formed from the carbonate electrolyte (Figure 5.6), facilitating a less diffusion-limited process of Na deposition at the interface along with a lower overpotential of Na deposition. This lower

overpotential of Na deposition will have aided a denser and more homogeneous growth of Na. The low deposition overpotential from an ionically conductive SEI, together with a strong suppression of deposition kinetics at Na tips, might contribute to a self-regulating Na interface that maintains a flat morphology, as observed in the in-situ AFM experiments.

5.2.7 DEMS analysis

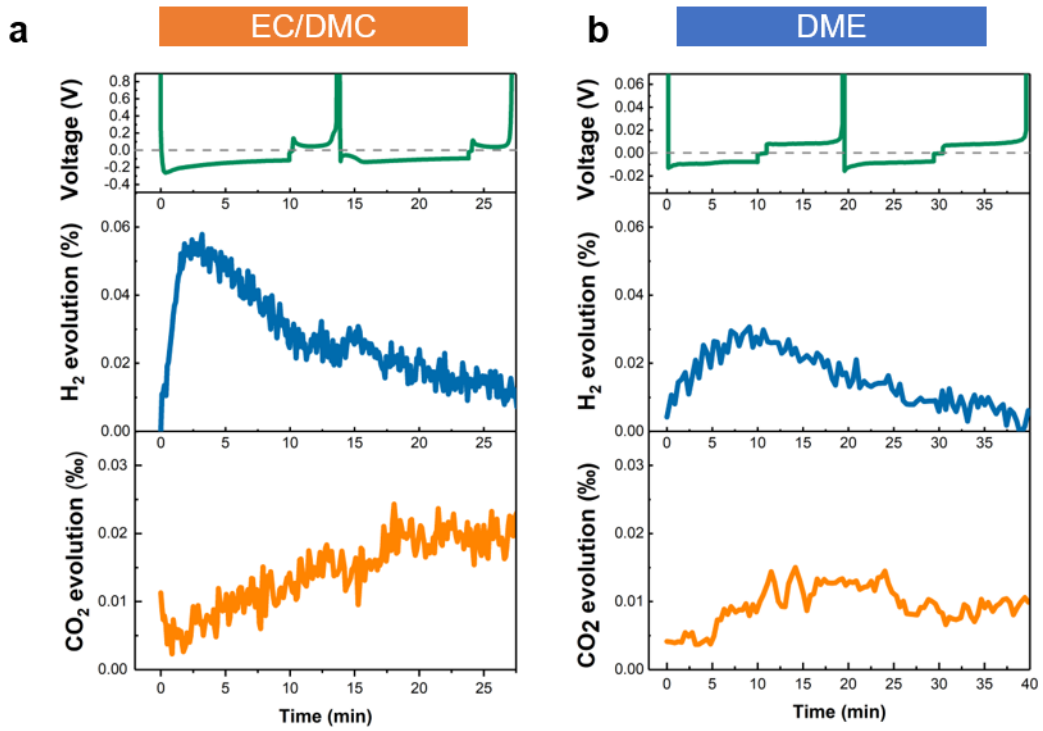


Figure 5.26. Differential electrochemical mass spectrometry (DEMS) analysis compares hydrogen evolution from carbonate and glyme electrolyte cells. It measured gas evolution during charge cycling with (a) carbonate (EC: DMC) and (b) glyme (DME) solvent electrolytes in a battery cell (with a current density 0.5 mA cm^{-2}).

The DEMS was performed to identify the gas evolution during battery cycling with carbonate and glyme electrolytes (as shown in Figure 5.26). A cold trap was integrated to cool the carrier gas after flowing through the battery cell to prevent solvent evaporation into

the spectrometer. This setup allowed the detection of gas evolution in real time with battery cycling. More details are illustrated in Chapter 3.3.4. Both cells were plated at a current density of 0.5 mA cm^{-2} for 10 minutes and then stripped to 1V. We found significantly more H_2 and CO_2 formation during cycling from the carbonate electrolyte (Figure 5.26), which is consistent with our in-situ TEM work.

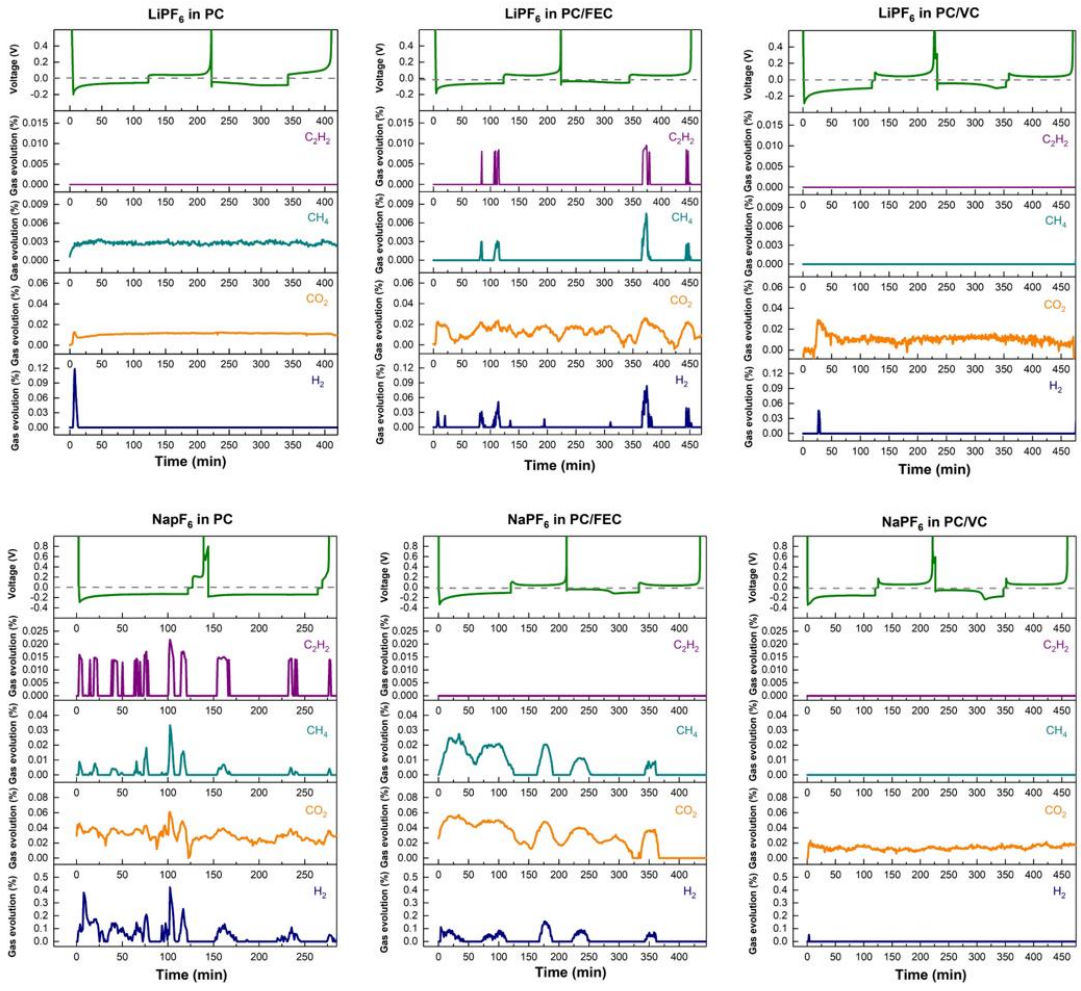


Figure 5.27. Differential electrochemical mass spectrometry (DEMS) study of gas evolution from carbonate electrolyte in Li and Na cells. The batteries were galvanostatically cycled at 0.5 mA cm^{-2} for two hours of plating and then stripped to 1V. More bubble formation is seen with the Na electrolyte compared to the Li electrolyte, especially for the C_2H_2, CO_2, and H_2.

In general, the gas was mainly formed during the first cycle when most of the electrolyte decomposition and SEI formation occurred.[222,235,236] There were more gas formation in carbonate-based cell and one possibility was that the SEI formed from the carbonate electrolyte was less stable. The SEI was more easily broken during the Na stripping process, leaving fresh Na exposed to the electrolyte and leading to new SEI formation.[222,236] The gas evolution during cycling in Li and Na carbonate electrolytes was systematically studied (Figure 5.27), revealing the greater degree of gas evolution from Na electrolytes compared to their Li analogs, thus highlighting the more significant role gas formation had for Na batteries. As shown in Figure 5.27, more C_2H_2, CO_2, and H_2 gas were seen with the Na electrolyte compared to the Li electrolyte. For the effect of adding additives, the VC was more effective in preventing the bubble formation from both Li and Na systems. In contrast, FEC induced more gas formation in the Li system, which might be attributed to the FEC decomposition to form SEI.[236]

5.2.8 Coin cell studies with other anode and cathode materials

To confirm the SEI formed by ether-based electrolytes can also positively affect other anode and cathode materials. The coin cell studies were performed to illustrate how the electrolyte solvent consideration remains relevant for cells beyond that of the simple metal anode half-cell (i.e., the Na||Cu coin cell). As shown in Figure 5.28, the hard carbon was cycled in Na||hard carbon half cells with ether electrolyte and carbonate electrolyte. The current density of C/3, C/10, and C/20 were cycled respectively for the first cycle. The coulombic efficiency of coin cells in ether electrolytes was better than carbonate electrolytes, although they performed similarly at the current density of C/3.

At the same current density of C/3, the Na||hard carbon coin cells with ether electrolyte and carbonate electrolyte were cycled for 30 cycles as shown in Figure 5.29. It clearly showed that the ether electrolyte drastically improved coin cell cycle life, with far less capacity fade in comparison to an equivalent carbonate electrolyte cell after long cycle life. These cycling data shows significantly improved cycling performance when a DME solvent electrolyte is used compared to EC: DMC solvent, even with a hard carbon anode.

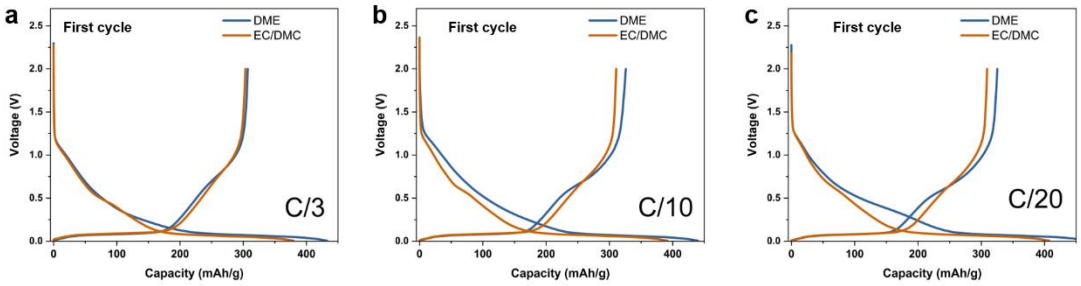


Figure 5.28. Cycling performance of Na||hard carbon coin cells for the first cycle at different current densities. The cycling is running at a specific rate of using 1 M $NaPF_6$ dissolved in DME solvent (ether), and EC: DMC solvent for the electrolyte. The active mass loading of hard carbon is around 3mg/cm^2 and C-rate was calculated by assuming a theoretical specific capacity of 150 mAh/g.

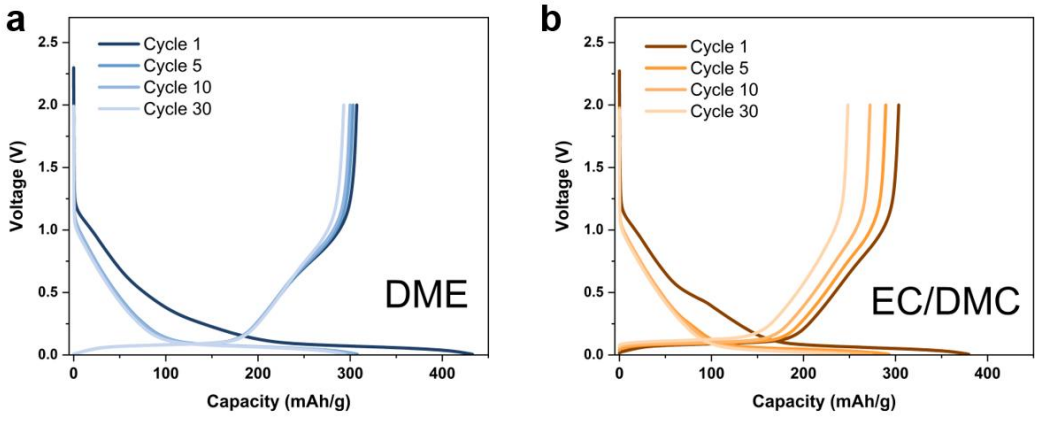


Figure 5.29. Cycling performance of Na||hard carbon coin cells. Capacity evolution over repeated charge/discharge cycling at a rate of C/3 using 1 M $NaPF_6$ dissolved in either (a) DME solvent (ether), or (b) EC: DMC solvent for the electrolyte. The active mass loading of hard carbon is around 3mg/cm^2 and C-rate was calculated by assuming a theoretical specific capacity of 150 mAh/g.

Recent works using an ether rather than carbonate-based Na electrolyte with hard carbon anodes have shown this performance improvement as well, and have attributed this to the distinct thin and conformal character of the formed interphase layer.[231,237,238] Similar performance improvement with using ether solvent electrolyte has also been shown when using Sn anodes. This suggests that the beneficial role of an ether solvent is agnostic to the anode material; the resulting thinner SEI layer, which offers better ionic conductivity, and the more accommodating mechanical properties that favor conformality during cycling, appears to offer generic utility for any Na anode.

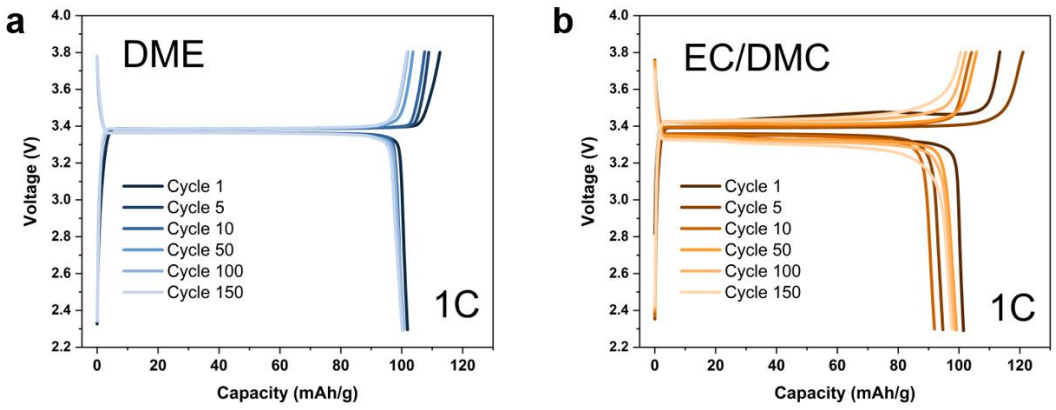


Figure 5.30. Cycling performance of $Na_3V_2(PO_4)_3$||Na coin cells in ether and carbonate electrolyte at a current density of 1C. Capacity evolution over repeated charge/discharge cycling at a rate of 1C for (a) 1 M $NaPF_6$ in DME and (b) 1 M $NaPF_6$ in EC: DMC electrolyte. The active mass loading of cathode material is around 3.0mg/cm^2 and C-rate was calculated by assuming a theoretical capacity of 118 mAh/g.

To claim the merit of ether-based electrolytes compared to carbonated-based electrolytes in the Na-ion battery system, the cathode material of $Na_3V_2(PO_4)_3$ was used for the coin cell test. The $Na_3V_2(PO_4)_3$ is a popular and stable sodium cathode material and it is widely used in the sodium electrolyte study. The $Na_3V_2(PO_4)_3$||Na coin cells were cycled in this

experiment with ether-based electrolyte and carbonate-based electrolyte at a current density of 1C first (as shown in Figure 5.30). The coulombic efficiency of ether-based coin cells was relatively stable, while there was obvious capacity decay in the carbonate-based electrolyte coin cells as shown in Figure 5.30b.

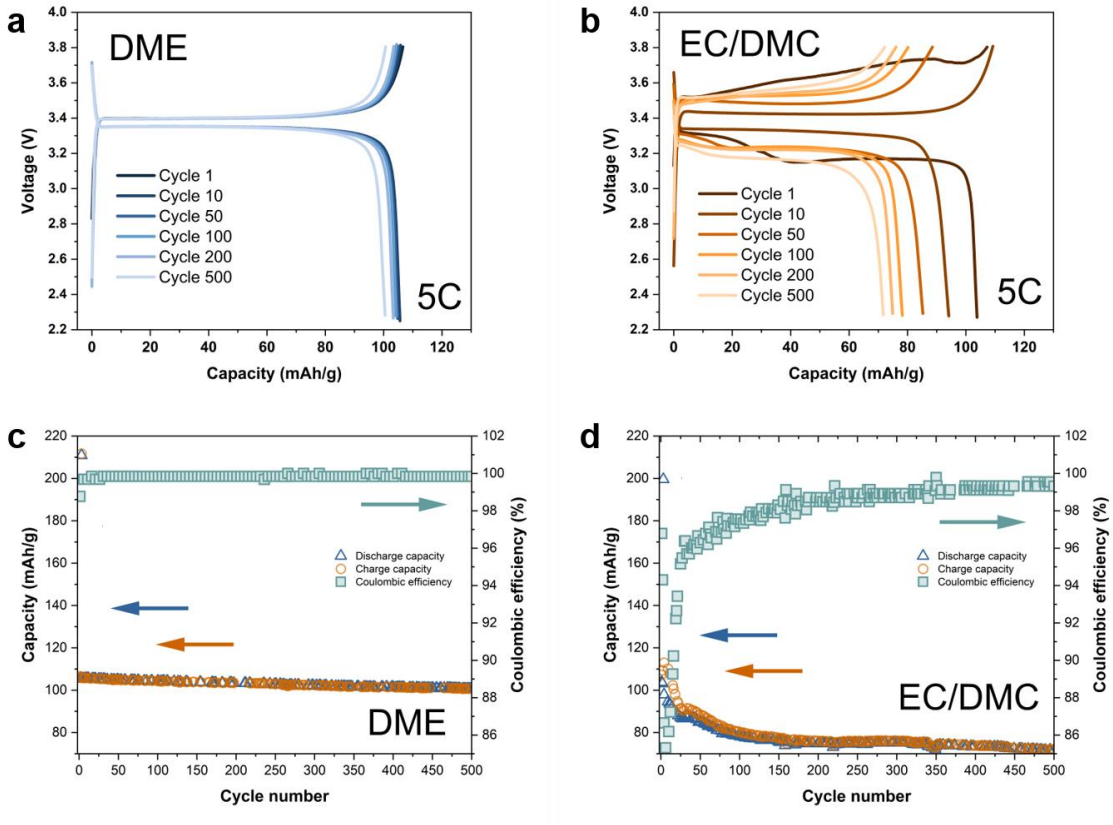


Figure 5.31. Cycling performance of $Na_3V_2(PO_4)_3$||Na coin cells in ether and carbonate electrolyte at a current density of 5C. Capacity evolution over repeated charge/discharge cycling at a rate of 5C for (a) 1 M $NaPF_6$ in DME and (b) 1 M $NaPF_6$ in EC: DMC electrolyte. The active mass loading of cathode material is around 3.0mg/cm^2 and C-rate was calculated by assuming a theoretical capacity of 118 mAh/g. (c,d) Charge and discharge capacity evolution and per cycle coulombic efficiency for DME and EC: DMC solvent electrolyte cells, respectively.

Cells cycled at a high rate (5C) were also measured as shown in Figure 5.31, the coin cells in ether-based electrolytes still exhibited excellent stability (Figure 5.31a), and very poor electrochemical cycling performance was presented in the carbonate-based electrolyte cells

(Figure 5.31b). The charge and discharge capacity evolution and per cycle coulombic efficiency for ether-based and carbonate-based electrolyte cells were illustrated in Figure 5.31c&d, respectively. These experiments show the significant performance improvement gained by using DME-based sodium electrolyte in metal anode full cells, with significantly less capacity decay observed over long-term cycling. This is in good agreement with the presented Na||Cu half-cell results.

5.3 Discussion

Bringing the all observations together, we can attribute the stronger performance of the glyme ether electrolyte to its (i) thinner and (ii) more mechanically robust SEI layer, compared to that formed by the carbonate ester electrolyte, as shown in Figure 5.32.

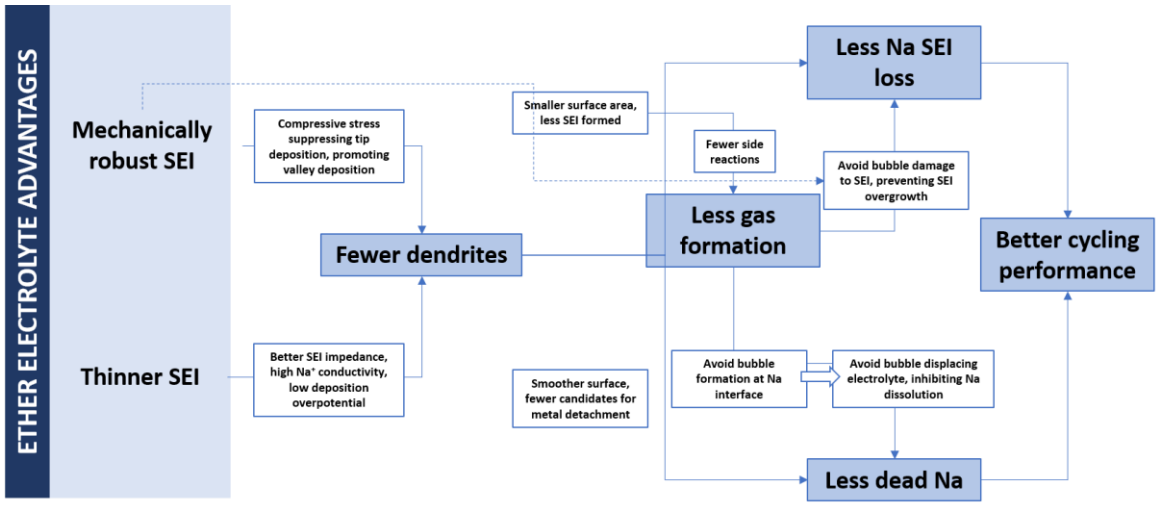


Figure 5.32. The logical map for the ether electrolyte advantages is based on our analysis.

The SEI layer formed from the glyme electrolyte was significantly thinner. According to

the online-MS study, we identified that the Na consumed to create SEI from the EC: DMC electrolyte was ten times more than for the glyme solvent in the first cycle (Figure 5.7), containing thirteen times more dead Na, sixteen times more NaH (Figure 5.8), and over thirty times more organic carbonates (such as $NaOCO_2R$ and CH_2OCO_2Na). For the third cycle, the SEI from EC: DMC continued to consume Na, while the glyme SEI underwent only limited growth (Figure 5.9). This supports the evaluation that the SEI formed from the EC: DMC electrolyte was thicker, while the glyme electrolyte SEI was comparatively thinner and more stable. This thinner SEI ensured a faster Na^+ transport across the SEI than that formed from the carbonate electrolyte (Figure 5.6), facilitating a less diffusion-limited process of Na deposition at the interface along with a lower overpotential of Na deposition. The lower overpotential of Na deposition aided Na's dense and homogeneous growth. The more uniform Na deposition from glyme electrolyte and rougher dendritic Na growth from EC: DMC electrolyte is well illustrated by the SEM (Figure 5.16) and AFM (Figure 5.20 and Figure 5.21) post-mortem images. As evidenced by the AFM, the smoother Na plating from ether electrolytes also reduces the level of SEI needed due to the smaller exposed electrolyte-electrode surface area.

The glyme electrolyte SEI is more elastic and stiffer and is thus more tolerant toward Na volume expansion (Figure 5.22). The less elastic SEI formed from the EC: DMC electrolyte may be attributed to the larger amount of carbonate ester ($NaOCO_2R$) and brittle inorganic components (NaH and Na_2CO_3) formed.[226] With a higher Young's modulus and a wider elastic region of the SEI formed from the glyme electrolyte, a greater mechanical back force (compressive) on Na can be maintained without breakage of the SEI.

The low deposition overpotential from a conductive SEI and strong suppression of deposition kinetics at the Na tip might contribute to a self-regulating Na interface that

maintains a flat morphology, as observed in our experiments (Figure 5.25). In addition, the elastic and stiff SEI formed from ether electrolyte will effectively defend against SEI breakage during Na cycling, minimizing the exposure of fresh Na to electrolyte and thus preventing further electrolyte decomposition. As gas bubbles are a product of electrolyte decomposition and are seen to be more prevalent for Na carbonate electrolytes (Figure 5.26), this may be a vital contributor to the high performance of ether electrolytes. The uncontrolled gas formation could further trap the SEI shell and lead to the porous deposited Na, as suggested in our in-situ STEM imaging (Figure 5.17) and SEM images (Figure 5.16). This results in more side reactions that generate other gas bubbles, yielding a negative feedback cycle of continual electrolyte decomposition.

5.4 Conclusion

We found that carbonate-based and ether-based electrolytes show significant differences in sodium electrochemical performance, and the mechanisms behind the improved sodium anode performance when cycling in ether electrolyte were systematically explored in this project. First, the dead sodium, NaH and SEI components were quantificationally measured by online-MS titration method, and the formation of hydrides in SEI was confirmed. Then, the extensive gas bubble formation during stripping along the electrode interface when operated in carbonate electrolyte was revealed by operando electrochemical TEM, while no such interfacial effervescence was observed when cycled with ether electrolyte. By employing with DEMS, significantly more H_2 and CO_2 formation during cycling from the carbonate electrolyte was verified. This gas formation at the interface will displace the electrolyte, and thus impede complete dissolution of plated sodium. The TEM imaging,

alongside AFM surface characterization, also highlighted the far smoother surface morphology for Na electroplated from ether electrolyte. In addition, the mechanical properties of SEI were measured by AFM and it showed that the ether SEI was more elastic and stiffer. This SEI provided more mechanical strength to suppress the non-uniform Na deposition and leading to fewer dendrites formation. I proposed that these favorable mechanical properties also prevented gas formation from SEI reactions that occurred during stripping, with the more inflexible non-conformal and brittle SEI derived from carbonate electrolyte more prone to delaminating from the Na and undergoing gas producing side reactions. The SEI structure was imaged by operando STEM to remain fixed in place, losing conformality with the electrode during electrostripping, and thus exposing fresh areas to side reactions with the electrolyte. The in-situ AFM was further performed to directly illustrate the sodium uniform deposition of the ether electrolyte.

The new science in this project included: (1) by using operando TEM and STEM, the localised gas bubbles formation was discovered and the effects on cycling behaviour were discussed. This has never been shown directly by microscopy before. (2) The dead sodium, NaH and some SEI organic components were quantificationally measured by isotope labelling online-MS titration method, this provided solid evidence to learn the degradation process of sodium metal battery. (3) The mechanical properties of SEI were measured, and the relationship between sodium plating/stripping process and SEI properties were discussed.

In summary, this project shows the critical importance of designing electrolytes such that they yield an elastic and robust SEI layer, as these properties promote uniform flat electroplating and inhibit gas producing side reactions.

Chapter 6. Conclusions and Future Work

6.1. Conclusions

Both the lithium metal anode and sodium metal anode are getting a lot of attention because of their high theoretical energy capacity and low electrochemical potential. However, the failure mechanisms of the metal anodes are required to be better understood. In this work, the degradation mechanisms of lithium metal anode and sodium metal anode in liquid batteries are systematically explored by several operando techniques, such as real-time LC-STEM, online-MS, DEMS, and in-situ AFM.

In the lithium project in Chapter 4, the degradation mechanism of the lithium metal anode was studied by comparing lithium cycling across fluoride-poor and fluoride-rich interphases. Through figuring out how the different SEI affected the lithium plating/stripping, the lithium morphology evolution in different systems was well investigated. In addition, the composition of the corresponding SEI was also analyzed, and the relationship between the SEI and lithium plating/stripping behaviors was discussed. By using LC-STEM to directly image the lithium plating/stripping process, the correlation between the deposition morphology and lithium stripping behavior was clearly established. For details, the plated lithium in a fluoride-poor system showed a loosely-packed needle-shaped morphology. Lithium was not necessarily removed exclusively from the dendrite tip; other parts might be stripped first, cutting off the conductive path to the dendrite tips and areas further away from the electrode surface. These isolated particles became ‘dead lithium’, and no longer grew or shrank with cycling. This uneven stripping can be attributed to the sparse dendritic morphology, which led to the electron channel easily being severed.

By contrast, the fluorinated system showed a flatter lithium deposit, where the plated lithium pieces were well connected. This relatively uniform lithium deposit morphology allowed most lithium to easily maintain electric contact with the working electrode during stripping. As a result, the stripping proceeded smoothly from the tips to the base, minimizing dead lithium formation. The real-time direct imaging of lithium plating/stripping dynamics supplies the solid evidence to describe how the dead lithium formation. In addition, with the help of the modified online-MS system, the fluoride-rich SEI was verified to help decrease electrolyte decomposition and suppressed LiH formation. This isotopic labeling experiment quantitatively proved the existence of LiH in SEI structures in lithium metal batteries. These findings on the relationship between SEI composition, lithium structural evolution, and the loss of lithium, will assist the informed design of new electrolytes and electrodes for more effective batteries.

In the sodium project in Chapter 5, the sodium plating/stripping mechanisms were studied based on my knowledge from the lithium project, as sodium was well known to be similar to lithium. Surprisingly, many differences were found between lithium and sodium, such as the growth morphology, SEI formation, and gas evolution. For sodium metal batteries, the carbonate-based fluoride-rich interphases showed a limited effect, and the ether-based electrolyte seemed almost perfect in cycling performance. With the help of online-MS, it was confirmed there was fewer dead sodium, Na_2CO_3, and NaH formation in the ether-based system compared to a carbonate-based electrolyte. The ex-situ AFM and in-situ AFM were employed to understand the details of the sodium plating/stripping process. The SEI in ether case was found to be much stiffer and more elastic, and plated sodium was more uniform. More importantly, by applying operando LC-TEM, the Na metal battery in the carbonate-based electrolyte was found to release plenty of gas during the sodium plating/stripping process. Gas evolution during the sodium plating/stripping process could

make sodium lose connection with the working electrode and form dead sodium. It was believed to be a significant problem for battery degradation. In contrast, few gases were observed in ether electrolytes. The DEMS experiment further verified the gas evolution phenomenon, proving more released gas from carbonate-based electrolytes. These observations emphasized the importance of understanding the sodium SEI properties and gas evolution in sodium metal battery design.

In conclusion, based on cutting-edge operando characterization techniques, this project has established some systematic understandings of the lithium/sodium metal anode degradation mechanisms, which could be helpful for the development of next-generation lithium/sodium metal batteries.

6.2. Future work

(1) In Chapter 4, there was an apparent bubble formation during lithium plating in LP30 with FEC electrolyte in in-situ STEM results (Figure 4.11). The bubble occurred in every cycle, and we had verified that it is not because of the electron beam. Surprisingly, the bubble was not discovered in LP30 electrolyte. Therefore, could we suspect that the FEC additives promote the bubble formation? As we know, the bubble could affect the lithium stripping process and harm the battery system; so, the FEC might not be an ideal additive, although it can significantly improve the lithium metal battery's coulombic efficiency. The detailed effects of the gas formation of FEC additive need to be explored. To answer this question, the DEMS setup could be used to measure the gas formation in lithium metal batteries in LP30 electrolyte with and without FEC additive. If there is obviously more gas formation after adding the FEC additive and the gas is generated in every cycle, the effects of the FEC in lithium metal battery need to be comprehensively discussed.

(2) By using online-MS in Chapter 4, lots of LiH was quantitatively found in SEI components in LP30 electrolyte batteries after cycling. The FEC additive could effectively reduce the LiH formation, and we have the same discoveries in sodium metal batteries. What is the role of the LiH or NaH in SEI components? Is it good or bad for the battery cycling? There are only a few works that explore it, while their views are usually opposite. We quantified the existence of the LiH and NaH in SEI, but how it forms and how it affects the battery in SEI still needs to be explored. To answer this question, the position of LiH in lithium metal battery SEI structures has to be confirmed first. The cryo-STEM and STEM EELS may be helpful with this analysis because the lithium metal anode and the SEI compositions are air-sensitive and beam-sensitive. If the LiH is observed to be large crystals and dendritic, it shows the LiH is not suitable to be a protective layer for the lithium metal anode and the LiH is bad for the battery cycling. Furthermore, the formation of LiH may have a relationship with H_2 evolution during battery cycling according to some previous studies. To verify this, different water-content electrolytes could be used to do the lithium metal battery cycling. The quantity of LiH could be measured by the isotope online-MS setup. After controlling all the other experimental parameters, if more LiH is measured in higher water content electrolyte case, it shows that the formation of LiH is related to the H_2 evolution in a battery because the trace of water can form H_2 during cycling.

(3) In Chapter 5, we observed that the sodium preferred to grow from the lower part while not the tip in the ether-based electrolyte from in-situ AFM characterization (Figure 5.25). This is not normal because there is usually stronger electric field distribution at the tip. Although we explained it by the SEI properties based on Monroe and Newman model, it still needs more evidence and explanations. First, it needs to check the mechanisms of sodium nucleation. Lithium prefers to grow like a whisker (Figure 1.4),

while sodium prefers to grow like particles (Figure 5.16), the nucleation of sodium has to be different and complex. Then the electric field distribution in the deposited sodium should be simulated considering the corresponding SEI properties. Thus, the sodium deposition mechanism could be better understood.

Chapter 7. References

1. Gilbert N. Lewis and Frederick G.Keyes. (1913). The potential of the lithium electrode. J. Am. Chem. Soc. *35*, 340–344.

2. Besenhard, J.O., and Eichinger, G. (1976). High energy density lithium cells. J. Electroanal. Chem. Interfacial Electrochem. *68*, 1–18.

3. B. M. L. Rao, R. W. Francis, H.A.C. (1977). Lithium-Aluminum Electrode. J. Electrochem. Soc. *124*, 1490.

4. Dey, A.N. (1971). Electrochemical Alloying of Lithium in Organic Electrolytes. J. Electrochem. Soc. *118*, 1547.

5. Besenhard, J.O. (1978). Cycling behaviour and corrosion of Li-Al electrodes in organic electrolytes. J. Electroanal. Chem. Interfacial Electrochem. *94*, 77–81.

6. Whittingham, M.S. (1974). Electrointercalation in transition-metal disulphides. J. Chem. Soc. Chem. Commun., 328–329.

7. Whittingham, M.S. (1976). Electrical Energy Storage and Intercalation Chemistry. Science. *192*, 1126–1127.

8. Whittingham, M.S., and Gamble, F.R. (1975). The lithium intercalates of the transition metal dichalcogenides. Mater. Res. Bull. *10*, 363–371.

9. Mizushima, K., Jones, P.C., Wiseman, P.J., and Goodenough, J.B. (1980). LixCoO2 (0<x<-1): A new cathode material for batteries of high energy density. Mater. Res. Bull. *15*, 783–789.

10. Thackeray, M.M., David, W.I.F., Bruce, P.G., and Goodenough, J.B. (1983). Lithium insertion into manganese spinels. Mater. Res. Bull. *18*, 461–472.

11. Dey, A.N., and Sullivan, B.P. (1970). The Electrochemical Decomposition of Propylene Carbonate on Graphite. J. Electrochem. Soc. *117*, 222.

12. Besenhard, J.O. (1976). The electrochemical preparation and properties of ionic alkali metal-and NR4-graphite intercalation compounds in organic electrolytes. Carbon N. Y. *14*, 111–115.

13. A. Yoshino, K. Sanechika, T.N. (1987). US patent 4668595A. United States Pat., 9.

14. Armand, M., and Tarascon, J.-M. (2008). Building better batteries. Nature *451*, 652–657.

15. Lin, D., Liu, Y., and Cui, Y. (2017). Reviving the lithium metal anode for high-energy batteries. Nat. Nanotechnol. *12*, 194–206.

16. Tikekar, M.D., Choudhury, S., Tu, Z., and Archer, L.A. (2016). Design principles for electrolytes and interfaces for stable lithium-metal batteries. Nat. Energy *1*, 16114.

17. Aurbach, D., Ein-Eli, Y., Chusid (Youngman), O., Carmeli, Y., Babai, M., and Yamin, H. (1994). The Correlation Between the Surface Chemistry and the Performance of Li-Carbon Intercalation Anodes for Rechargeable 'Rocking-Chair' Type Batteries. J. Electrochem. Soc. *141*, 603–611.

18. Zhou, Y., Su, M., Yu, X., Zhang, Y., Wang, J.G., Ren, X., Cao, R., Xu, W., Baer, D.R., Du, Y., et al. (2020). Real-time mass spectrometric characterization of the

solid–electrolyte interphase of a lithium-ion battery. Nat. Nanotechnol. *15*, 224–230.

19. Zachman, M.J., Tu, Z., Choudhury, S., Archer, L.A., and Kourkoutis, L.F. (2018). Cryo-STEM mapping of solid–liquid interfaces and dendrites in lithium-metal batteries. Nature *560*, 345–349.

20. Zhang, S. (2017). Chemomechanical modeling of lithiation-induced failure in high-volume-change electrode materials for lithium ion batteries. npj Comput. Mater. *3*, 7.

21. Fang, C., Li, J., Zhang, M., Zhang, Y., Yang, F., Lee, J.Z., Lee, M.H., Alvarado, J., Schroeder, M.A., Yang, Y., et al. (2019). Quantifying inactive lithium in lithium metal batteries. Nature *572*, 511–515.

22. Peled, E., and Menkin, S. (2017). Review-SEI: Past, Present and Future. J. Electrochem. Soc. *164*, 1703–1719.

23. Rosalind E. Franklin (1951). Crystallite growth in graphitizing and non-graphitizing carbons. Proc. R. Soc. A. *209*, 196–218.

24. Satoh, A. (1995). Electrochemical intercalation of lithium into graphitized carbons. Solid State Ionics *80*, 291–298.

25. Dahn, J.R., Zheng, T., Liu, Y., and Xue, J.S. (1995). Mechanisms for Lithium Insertion in Carbonaceous Materials. Science. *270*, 590–593.

26. Nishi, Y. (2001). Lithium ion secondary batteries; past 10 years and the future. J. Power Sources *100*, 101–106.

27. Shu, Z.X., McMillan, R.S., and Murray, J.J. (1993). Electrochemical Intercalation of

Lithium into Graphite. J. Electrochem. Soc. *140*, 922–927.

28. Lu, W., Donepudi, V.S., Prakash, J., Liu, J., and Amine, K. (2002). Electrochemical and thermal behavior of copper coated type MAG-20 natural graphite. Electrochim. Acta *47*, 1601–1606.

29. Buiel, E., and Dahn, J.. (1999). Li-insertion in hard carbon anode materials for Li-ion batteries. Electrochim. Acta *45*, 121–130.

30. Liu, Y., Xue, J.S., Zheng, T., and Dahn, J.R. (1996). Mechanism of lithium insertion in hard carbons prepared by pyrolysis of epoxy resins. Carbon N. Y. *34*, 193–200.

31. Nishi, Y. (2001). The development of lithium ion secondary batteries. Chem. Rec. *1*, 406–413.

32. Fong, R., von Sacken, U., and Dahn, J.R. (1990). Studies of Lithium Intercalation into Carbons Using Nonaqueous Electrochemical Cells. J. Electrochem. Soc. *137*, 2009–2013.

33. Kalhoff, J., Eshetu, G.G., Bresser, D., and Passerini, S. (2015). Safer Electrolytes for Lithium-Ion Batteries: State of the Art and Perspectives. ChemSusChem *8*, 2154–2175.

34. Aurbach, D., Gamolsky, K., Markovsky, B., Gofer, Y., Schmidt, M., and Heider, U. (2002). On the use of vinylene carbonate (VC) as an additive to electrolyte solutions for Li-ion batteries. Electrochim. Acta *47*, 1423–1439.

35. Michan, A.L., Parimalam, B.S., Leskes, M., Kerber, R.N., Yoon, T., Grey, C.P., and Lucht, B.L. (2016). Fluoroethylene Carbonate and Vinylene Carbonate Reduction:

Understanding Lithium-Ion Battery Electrolyte Additives and Solid Electrolyte Interphase Formation. Chem. Mater. *28*, 8149–8159.

36. Li, M., Lu, J., Chen, Z., and Amine, K. (2018). 30 Years of Lithium-Ion Batteries. Adv. Mater. *30*, 1800561.

37. Fujimoto, H., Fujimoto, M., Ikeda, H., Ohshita, R., Fujitani, S., and Yonezu, I. (2001). Electrochemical characteristics of lithiated graphite (LiC6) in PC based electrolytes. J. Power Sources *93*, 224–229.

38. Etacheri, V., Marom, R., Elazari, R., Salitra, G., and Aurbach, D. (2011). Challenges in the development of advanced Li-ion batteries: a review. Energy Environ. Sci. *4*, 3243.

39. Liu, X.H., and Huang, J.Y. (2011). In situ TEM electrochemistry of anode materials in lithium ion batteries. Energy Environ. Sci. *4*, 3844.

40. Chon, M.J., Sethuraman, V.A., McCormick, A., Srinivasan, V., and Guduru, P.R. (2011). Real-Time Measurement of Stress and Damage Evolution during Initial Lithiation of Crystalline Silicon. Phys. Rev. Lett. *107*, 045503.

41. Tian, H., Xin, F., Wang, X., He, W., and Han, W. (2015). High capacity group-IV elements (Si, Ge, Sn) based anodes for lithium-ion batteries. J. Mater. *1*, 153–169.

42. Xu, C., Lindgren, F., Philippe, B., Gorgoi, M., Björefors, F., Edström, K., and Gustafsson, T. (2015). Improved Performance of the Silicon Anode for Li-Ion Batteries: Understanding the Surface Modification Mechanism of Fluoroethylene Carbonate as an Effective Electrolyte Additive. Chem. Mater. *27*, 2591–2599.

43. Cheng, X.B., Zhang, R., Zhao, C.Z., and Zhang, Q. (2017). Toward Safe Lithium Metal Anode in Rechargeable Batteries: A Review. Chem. Rev. *117*, 10403–10473.

44. Xu, W., Wang, J., Ding, F., Chen, X., Nasybulin, E., Zhang, Y., and Zhang, J.G. (2014). Lithium metal anodes for rechargeable batteries. Energy Environ. Sci. *7*, 513–537.

45. Sun, Y., Liu, N., and Cui, Y. (2016). Promises and challenges of nanomaterials for lithium-based rechargeable batteries. Nat. Energy *1*, 16071.

46. Fang, C., Wang, X., and Meng, Y.S. (2019). Key Issues Hindering a Practical Lithium-Metal Anode. Trends Chem. *1*, 152–158.

47. Peled, E. (1979). The Electrochemical Behavior of Alkali and Alkaline Earth Metals in Nonaqueous Battery Systems—The Solid Electrolyte Interphase Model. J. Electrochem. Soc. *126*, 2047–2051.

48. Aurbach, D., Talyosef, Y., Markovsky, B., Markevich, E., Zinigrad, E., Asraf, L., Gnanaraj, J.S., and Kim, H.-J. (2004). Design of electrolyte solutions for Li and Li-ion batteries: a review. Electrochim. Acta *50*, 247–254.

49. Goodenough, J.B., and Kim, Y. (2010). Challenges for Rechargeable Li Batteries. Chem. Mater. *22*, 587–603.

50. Peled, E., Golodnitsky, D., and Ardel, G. (1997). Advanced Model for Solid Electrolyte Interphase Electrodes in Liquid and Polymer Electrolytes. J. Electrochem. Soc. *144*, L208–L210.

51. Aurbach, D., Markovsky, B., Levi, M.., Levi, E., Schechter, A., Moshkovich, M.,

and Cohen, Y. (1999). New insights into the interactions between electrode materials and electrolyte solutions for advanced nonaqueous batteries. J. Power Sources *81–82*, 95–111.

52. Spotte-Smith, E.W.C., Kam, R.L., Barter, D., Xie, X., Hou, T., Dwaraknath, S., Blau, S.M., and Persson, K.A. (2022). Toward a Mechanistic Model of Solid–Electrolyte Interphase Formation and Evolution in Lithium-Ion Batteries. ACS Energy Lett. *7*, 1446–1453.

53. Wang, L., Menakath, A., Han, F., Wang, Y., Zavalij, P.Y., Gaskell, K.J., Borodin, O., Iuga, D., Brown, S.P., Wang, C., et al. (2019). Identifying the components of the solid–electrolyte interphase in Li-ion batteries. Nat. Chem. *11*, 789–796.

54. Wang, X., Zhang, M., Alvarado, J., Wang, S., Sina, M., Lu, B., Bouwer, J., Xu, W., Xiao, J., Zhang, J.-G., et al. (2017). New Insights on the Structure of Electrochemically Deposited Lithium Metal and Its Solid Electrolyte Interphases via Cryogenic TEM. Nano Lett. *17*, 7606–7612.

55. Liu, W., Liu, P., and Mitlin, D. (2020). Review of Emerging Concepts in SEI Analysis and Artificial SEI Membranes for Lithium, Sodium, and Potassium Metal Battery Anodes. Adv. Energy Mater. *10*, 2002297.

56. Epelboin, I., Froment, M., Garreau, M., Thevenin, J., and Warin, D. (1980). Behavior of Secondary Lithium and Aluminum-Lithium Electrodes in Propylene Carbonate. J. Electrochem. Soc. *127*, 2100–2104.

57. Steiger, J., Kramer, D., and Mönig, R. (2014). Microscopic observations of the formation, growth and shrinkage of lithium moss during electrodeposition and

dissolution. Electrochim. Acta *136*, 529–536.

58. Park, M.S., Ma, S.B., Lee, D.J., Im, D., Doo, S.-G., and Yamamoto, O. (2015). A Highly Reversible Lithium Metal Anode. Sci. Rep. *4*, 3815.

59. Chen, Q., Geng, K., and Sieradzki, K. (2015). Prospects for Dendrite-Free Cycling of Li Metal Batteries. J. Electrochem. Soc. *162*, A2004–A2007.

60. Xiao, J. (2019). How lithium dendrites form in liquid batteries. Science. *366*, 426–427.

61. Sand, H.J.S. (1899). On the Concentration at the Electrodes in a Solution, with special reference to the Liberation of Hydrogen by Electrolysis of a Mixture of Copper Sulphate and Sulphuric Acid. Proc. Phys. Soc. London *17*, 496–534.

62. Elezgaray, J., Léger, C., and Argoul, F. (1998). Linear Stability Analysis of Unsteady Galvanostatic Electrodeposition in the Two-Dimensional Diffusion-Limited Regime. J. Electrochem. Soc. *145*, 2016–2024.

63. Bai, P., Li, J., Brushett, F.R., and Bazant, M.Z. (2016). Transition of lithium growth mechanisms in liquid electrolytes †. Energy Environ. Sci *9*, 3221.

64. Yang, C., Chen, J., Ji, X., Pollard, travis P., Lü, X., Sun, C.-J., Hou, S., Liu, Q., Liu, C., Qing, T., et al. (2019). Aqueous Li-ion battery enabled by halogen conversion–intercalation chemistry in graphite. Nature *569*, 245–250.

65. Yamada, Y., Wang, J., Ko, S., Watanabe, E., and Yamada, A. (2019). Advances and issues in developing salt-concentrated battery electrolytes. Nat. Energy *4*, 269–280.

66. Hu, Z., Zhang, S., Dong, S., Li, Q., Cui, G., and Chen, L. (2018). Self-Stabilized

Solid Electrolyte Interface on a Host-Free Li-Metal Anode toward High Areal Capacity and Rate Utilization. Cite This Chem. Mater *30*, 4039–4047.

67. Xu, R., Cheng, X.-B., Yan, C., Zhang, X.-Q., Xiao, Y., Zhao, C.-Z., Huang, J.-Q., and Zhang, Q. (2019). Artificial Interphases for Highly Stable Lithium Metal Anode. Matter *1*, 317–344.

68. Xu, Q., Yang, Y., and Shao, H. (2015). Substrate effects on Li + electrodeposition in Li secondary batteries with a competitive kinetics model. Phys. Chem. Chem. Phys. *17*, 20398–20406.

69. Brown, Z.L., Jurng, S., Nguyen, C.C., and Lucht, B.L. (2018). Effect of Fluoroethylene Carbonate Electrolytes on the Nanostructure of the Solid Electrolyte Interphase and Performance of Lithium Metal Anodes. ACS Appl. Energy Mater. *1*, 3057–3062.

70. Cheng, X.-B., Zhang, R., Zhao, C.-Z., Wei, F., Zhang, J.-G., and Zhang, Q. (2016). A Review of Solid Electrolyte Interphases on Lithium Metal Anode. Adv. Sci. *3*, 1500213.

71. Liu, Y., Lin, D., Li, Y., Chen, G., Pei, A., Nix, O., Li, Y., and Cui, Y. (2018). Solubility-mediated sustained release enabling nitrate additive in carbonate electrolytes for stable lithium metal anode. Nat. Commun. *9*, 3656.

72. Zhao, H., Yu, X., Li, J., Li, B., Shao, H., Li, L., and Deng, Y. (2019). Film-forming electrolyte additives for rechargeable lithium-ion batteries: progress and outlook. J. Mater. Chem. A *7*, 8700–8722.

73. Zhang, X.-Q., Cheng, X.-B., Chen, X., Yan, C., and Zhang, Q. (2017).

Fluoroethylene Carbonate Additives to Render Uniform Li Deposits in Lithium Metal Batteries. Adv. Funct. Mater. *27*, 1605989.

74. Zhang, S.S. (2006). A review on electrolyte additives for lithium-ion batteries. J. Power Sources *162*, 1379–1394.

75. Ma, L., Kim, M.S., and Archer, L.A. (2017). Stable Artificial Solid Electrolyte Interphases for Lithium Batteries. Chem. Mater. *29*, 4181–4189.

76. Cheng, X.-B., Yan, C., Chen, X., Guan, C., Huang, J.-Q., Peng, H.-J., Zhang, R., Yang, S.-T., and Zhang, Q. (2017). Implantable Solid Electrolyte Interphase in Lithium-Metal Batteries. Chem *2*, 258–270.

77. Li, N.-W., Yin, Y.-X., Yang, C.-P., and Guo, Y.-G. (2016). An Artificial Solid Electrolyte Interphase Layer for Stable Lithium Metal Anodes. Adv. Mater. *28*, 1853–1858.

78. Liu, Y., Lin, D., Yuen, P.Y., Liu, K., Xie, J., Dauskardt, R.H., and Cui, Y. (2017). An Artificial Solid Electrolyte Interphase with High Li-Ion Conductivity, Mechanical Strength, and Flexibility for Stable Lithium Metal Anodes. Adv. Mater. *29*, 1605531.

79. Basile, A., Bhatt, A.I., and O'Mullane, A.P. (2016). Stabilizing lithium metal using ionic liquids for long-lived batteries. Nat. Commun. *7*, ncomms11794.

80. Kazyak, E., Wood, K.N., and Dasgupta, N.P. (2015). Improved Cycle Life and Stability of Lithium Metal Anodes through Ultrathin Atomic Layer Deposition Surface Treatments. Chem. Mater. *27*, 6457–6462.

81. Chen, L., Connell, J.G., Nie, A., Huang, Z., Zavadil, K.R., Klavetter, K.C., Yuan, Y., Sharifi-Asl, S., Shahbazian-Yassar, R., Libera, J.A., et al. (2017). Lithium metal protected by atomic layer deposition metal oxide for high performance anodes. J. Mater. Chem. A *5*, 12297–12309.

82. Jing, H.-K., Kong, L.-L., Liu, S., Li, G.-R., and Gao, X.-P. (2015). Protected lithium anode with porous Al 2 O 3 layer for lithium–sulfur battery. J. Mater. Chem. A *3*, 12213–12219.

83. Fan, L., Zhuang, H.L., Gao, L., Lu, Y., and Archer, L.A. (2017). Regulating Li deposition at artificial solid electrolyte interphases. J. Mater. Chem. A *5*, 3483–3492.

84. Camacho-Forero, L.E., Smith, T.W., and Balbuena, P.B. (2017). Effects of High and Low Salt Concentration in Electrolytes at Lithium–Metal Anode Surfaces. J. Phys. Chem. C *121*, 182–194.

85. Yamada, Y., Furukawa, K., Sodeyama, K., Kikuchi, K., Yaegashi, M., Tateyama, Y., and Yamada, A. (2014). Unusual Stability of Acetonitrile-Based Superconcentrated Electrolytes for Fast-Charging Lithium-Ion Batteries. J. Am. Chem. Soc. *136*, 5039–5046.

86. Wan, C., Xu, S., Hu, M.Y., Cao, R., Qian, J., Qin, Z., Liu, J., Mueller, K.T., Zhang, J.-G., and Hu, J.Z. (2017). Multinuclear NMR Study of the Solid Electrolyte Interface Formed in Lithium Metal Batteries. ACS Appl. Mater. Interfaces *9*, 14741–14748.

87. Qian, J., Henderson, W.A., Xu, W., Bhattacharya, P., Engelhard, M., Borodin, O., and Zhang, J.-G. (2015). High rate and stable cycling of lithium metal anode. Nat.

Commun. *6*, 6362.

88. Zhang, R., Chen, X.-R., Chen, X., Cheng, X.-B., Zhang, X.-Q., Yan, C., and Zhang, Q. (2017). Lithiophilic Sites in Doped Graphene Guide Uniform Lithium Nucleation for Dendrite-Free Lithium Metal Anodes. Angew. Chemie Int. Ed. *56*, 7764–7768.

89. Zhang, Z., Peng, Z., Zheng, J., Wang, S., Liu, Z., Bi, Y., Chen, Y., Wu, G., Li, H., Cui, P., et al. (2017). The long life-span of a Li-metal anode enabled by a protective layer based on the pyrolyzed N-doped binder network. J. Mater. Chem. A *5*, 9339–9349.

90. Liang, Z., Zheng, G., Liu, C., Liu, N., Li, W., Yan, K., Yao, H., Hsu, P.-C., Chu, S., and Cui, Y. (2015). Polymer Nanofiber-Guided Uniform Lithium Deposition for Battery Electrodes. Nano Lett. *15*, 2910–2916.

91. Liu, W., Mi, Y., Weng, Z., Zhong, Y., Wu, Z., and Wang, H. (2017). Functional metal–organic framework boosting lithium metal anode performance via chemical interactions. Chem. Sci. *8*, 4285–4291.

92. Li, Q., Zhu, S., and Lu, Y. (2017). 3D Porous Cu Current Collector/Li-Metal Composite Anode for Stable Lithium-Metal Batteries. Adv. Funct. Mater. *27*, 1606422.

93. Yun, Q., He, Y.-B., Lv, W., Zhao, Y., Li, B., Kang, F., and Yang, Q.-H. (2016). Chemical Dealloying Derived 3D Porous Current Collector for Li Metal Anodes. Adv. Mater. *28*, 6932–6939.

94. Yang, C.-P., Yin, Y.-X., Zhang, S.-F., Li, N.-W., and Guo, Y.-G. (2015). Accommodating lithium into 3D current collectors with a submicron skeleton

towards long-life lithium metal anodes. Nat. Commun. *6*, 8058.

95. Matsuda, S., Kubo, Y., Uosaki, K., and Nakanishi, S. (2017). Lithium-metal deposition/dissolution within internal space of CNT 3D matrix results in prolonged cycle of lithium-metal negative electrode. Carbon N. Y. *119*, 119–123.

96. Zhang, D., Zhou, Y., Liu, C., and Fan, S. (2016). The effect of the carbon nanotube buffer layer on the performance of a Li metal battery. Nanoscale *8*, 11161–11167.

97. Cheng, X.-B., Peng, H.-J., Huang, J.-Q., Wei, F., and Zhang, Q. (2014). Dendrite-Free Nanostructured Anode: Entrapment of Lithium in a 3D Fibrous Matrix for Ultra-Stable Lithium-Sulfur Batteries. Small *10*, 4257–4263.

98. Zhang, X., Wang, W., Wang, A., Huang, Y., Yuan, K., Yu, Z., Qiu, J., and Yang, Y. (2014). Improved cycle stability and high security of Li-B alloy anode for lithium–sulfur battery. J. Mater. Chem. A *2*, 11660–11665.

99. Ji, X., Liu, D.-Y., Prendiville, D.G., Zhang, Y., Liu, X., and Stucky, G.D. (2012). Spatially heterogeneous carbon-fiber papers as surface dendrite-free current collectors for lithium deposition. Nano Today *7*, 10–20.

100. Zuo, T.-T., Wu, X.-W., Yang, C.-P., Yin, Y.-X., Ye, H., Li, N.-W., and Guo, Y.-G. (2017). Graphitized Carbon Fibers as Multifunctional 3D Current Collectors for High Areal Capacity Li Anodes. Adv. Mater. *29*, 1700389.

101. Zheng, F., Kotobuki, M., Song, S., Lai, M.O., and Lu, L. (2018). Review on solid electrolytes for all-solid-state lithium-ion batteries. J. Power Sources *389*, 198–213.

102. Lou, S., Zhang, F., Fu, C., Chen, M., Ma, Y., Yin, G., and Wang, J. (2021). Interface

Issues and Challenges in All-Solid-State Batteries: Lithium, Sodium, and Beyond. Adv. Mater. *33*, 2000721.

103. Zhao, H., Wang, J., Shao, H., Xu, K., and Deng, Y. (2022). Gas Generation Mechanism in Li-Metal Batteries. ENERGY Environ. Mater. *5*, 327–336.

104. Aurbach, D. (2002). A short review of failure mechanisms of lithium metal and lithiated graphite anodes in liquid electrolyte solutions. Solid State Ionics *148*, 405–416.

105. Rowden, B., and Garcia-Araez, N. (2020). A review of gas evolution in lithium ion batteries. Energy Reports *6*, 10–18.

106. Galushkin, N.E., Yazvinskaya, N.N., and Galushkin, D.N. (2019). Mechanism of Gases Generation during Lithium-Ion Batteries Cycling. J. Electrochem. Soc. *166*, A897–A908.

107. Metzger, M., Strehle, B., Solchenbach, S., and Gasteiger, H.A. (2016). Origin of H 2 Evolution in LIBs: H 2 O Reduction vs. Electrolyte Oxidation . J. Electrochem. Soc. *163*, A798–A809.

108. Imhof, R., and Novák, P. (1998). In Situ Investigation of the Electrochemical Reduction of Carbonate Electrolyte Solutions at Graphite Electrodes. J. Electrochem. Soc. *145*, 1081–1087.

109. Zhang, B., Metzger, M., Solchenbach, S., Payne, M., Meini, S., Gasteiger, H.A., Garsuch, A., and Lucht, B.L. (2015). Role of 1,3-Propane Sultone and Vinylene Carbonate in Solid Electrolyte Interface Formation and Gas Generation. J. Phys. Chem. C *119*, 11337–11348.

110. Gachot, G., Ribière, P., Mathiron, D., Grugeon, S., Armand, M., Leriche, J.-B., Pilard, S., and Laruelle, S. (2011). Gas Chromatography/Mass Spectrometry As a Suitable Tool for the Li-Ion Battery Electrolyte Degradation Mechanisms Study. Anal. Chem. *83*, 478–485.

111. He, M., Castel, E., Laumann, A., Nuspl, G., Novák, P., and Berg, E.J. (2015). In Situ Gas Analysis of Li 4 Ti 5 O 12 Based Electrodes at Elevated Temperatures. J. Electrochem. Soc. *162*, A870–A876.

112. Guillot, S.L., Usrey, M.L., Peña-Hueso, A., Kerber, B.M., Zhou, L., Du, P., and Johnson, T. (2021). Reduced Gassing In Lithium-Ion Batteries With Organosilicon Additives. J. Electrochem. Soc. *168*, 030533.

113. Schiele, A., Breitung, B., Hatsukade, T., Berkes, B.B., Hartmann, P., Janek, J., and Brezesinski, T. (2017). The Critical Role of Fluoroethylene Carbonate in the Gassing of Silicon Anodes for Lithium-Ion Batteries. ACS Energy Lett. *2*, 2228–2233.

114. Zhang, Y., Sun, W., Xu, R., Wang, L., and Tang, H. (2021). Lithium extraction from water lithium resources through green electrochemical-battery approaches: A comprehensive review. J. Clean. Prod. *285*, 124905.

115. Kelly, J.C., Wang, M., Dai, Q., and Winjobi, O. (2021). Energy, greenhouse gas, and water life cycle analysis of lithium carbonate and lithium hydroxide monohydrate from brine and ore resources and their use in lithium ion battery cathodes and lithium ion batteries. Resour. Conserv. Recycl. *174*, 105762.

116. Grosjean, C., Miranda, P.H., Perrin, M., and Poggi, P. (2012). Assessment of world lithium resources and consequences of their geographic distribution on the expected

development of the electric vehicle industry. Renew. Sustain. Energy Rev. *16,* 1735–1744.

117. Chayambuka, K., Mulder, G., Danilov, D.L., and Notten, P.H.L. (2018). Sodium-Ion Battery Materials and Electrochemical Properties Reviewed. Adv. Energy Mater. *8,* 1800079.

118. Tanibata, N., Tsukasaki, H., Deguchi, M., Mori, S., Hayashi, A., and Tatsumisago, M. (2017). Characterization of sulfur nanocomposite electrodes containing phosphorus sulfide for high-capacity all-solid-state Na/S batteries. Solid State Ionics *311*, 6–13.

119. Ye, H., Ma, L., Zhou, Y., Wang, L., Han, N., Zhao, F., Deng, J., Wu, T., Li, Y., and Lu, J. (2017). Amorphous MoS 3 as the sulfur-equivalent cathode material for room-temperature Li–S and Na–S batteries. Proc. Natl. Acad. Sci. *114*, 13091–13096.

120. Wang, Y., Zhang, B., Lai, W., Xu, Y., Chou, S., Liu, H., and Dou, S. (2017). Room-Temperature Sodium-Sulfur Batteries: A Comprehensive Review on Research Progress and Cell Chemistry. Adv. Energy Mater. *7*, 1602829.

121. Sun, Q., Yang, Y., and Fu, Z.-W. (2012). Electrochemical properties of room temperature sodium–air batteries with non-aqueous electrolyte. Electrochem. commun. *16*, 22–25.

122. Xia, C., Black, R., Fernandes, R., Adams, B., and Nazar, L.F. (2015). The critical role of phase-transfer catalysis in aprotic sodium oxygen batteries. Nat. Chem. *7,* 496–501.

123. Frith, J.T., Landa-Medrano, I., Ruiz de Larramendi, I., Rojo, T., Owen, J.R., and

Garcia-Araez, N. (2017). Improving Na–O 2 batteries with redox mediators. Chem. Commun. *53*, 12008–12011.

124. Xu, S., Lu, Y., Wang, H., Abruña, H.D., and Archer, L.A. (2014). A rechargeable Na–CO 2 /O 2 battery enabled by stable nanoparticle hybrid electrolytes. J. Mater. Chem. A *2*, 17723–17729.

125. Lee, B., Paek, E., Mitlin, D., and Lee, S.W. (2019). Sodium Metal Anodes: Emerging Solutions to Dendrite Growth. Chem. Rev. *119*, 5416–5460.

126. Zheng, X., Huang, L., Ye, X., Zhang, J., Min, F., Luo, W., and Huang, Y. (2021). Critical effects of electrolyte recipes for Li and Na metal batteries. Chem *7*, 2312–2346.

127. Zheng, X., Bommier, C., Luo, W., Jiang, L., Hao, Y., and Huang, Y. (2019). Sodium metal anodes for room-temperature sodium-ion batteries: Applications, challenges and solutions. Energy Storage Mater. *16*, 6–23.

128. Xiang, Y., Zheng, G., Liang, Z., Jin, Y., Liu, X., Chen, S., Zhou, K., Zhu, J., Lin, M., He, H., et al. (2020). Visualizing the growth process of sodium microstructures in sodium batteries by in-situ 23Na MRI and NMR spectroscopy. Nat. Nanotechnol. *15*, 883–890.

129. Cohn, A.P., Muralidharan, N., Carter, R., Share, K., and Pint, C.L. (2017). Anode-Free Sodium Battery through in Situ Plating of Sodium Metal. Nano Lett. *17*, 1296–1301.

130. Fan, L., and Li, X. (2018). Recent advances in effective protection of sodium metal anode. Nano Energy *53*, 630–642.

131. Fang, C., Wang, X., and Meng, Y.S. (2019). Key Issues Hindering a Practical Lithium-Metal Anode. Trends Chem. *1*, 152–158.

132. Hu, J., Wang, H., Wang, S., Lei, Y., Qin, L., Li, X., Zhai, D., Li, B., and Kang, F. (2021). Electrochemical deposition mechanism of sodium and potassium. Energy Storage Mater. *36*, 91–98.

133. Seh, Z.W., Sun, J., Sun, Y., and Cui, Y. (2015). A Highly Reversible Room-Temperature Sodium Metal Anode. ACS Cent. Sci. *1*, 449–455.

134. Iermakova, D.I., Dugas, R., Palacín, M.R., and Ponrouch, A. (2015). On the Comparative Stability of Li and Na Metal Anode Interfaces in Conventional Alkyl Carbonate Electrolytes. J. Electrochem. Soc. *162*, A7060–A7066.

135. Dugas, R., Ponrouch, A., Gachot, G., David, R., Palacin, M.R., and Tarascon, J.M. (2016). Na Reactivity toward carbonate-based electrolytes: The effect of FEC as additive. J. Electrochem. Soc. *163*, A2333–A2339.

136. Rudola, A., Aurbach, D., and Balaya, P. (2014). A new phenomenon in sodium batteries: Voltage step due to solvent interaction. Electrochem. commun. *46*, 56–59.

137. Hong, Y.-S., Li, N., Chen, H., Wang, P., Song, W.-L., and Fang, D. (2018). In operando observation of chemical and mechanical stability of Li and Na dendrites under quasi-zero electrochemical field. Energy Storage Mater. *11*, 118–126.

138. Ma, L.A., Naylor, A.J., Nyholm, L., and Younesi, R. (2021). Strategies for Mitigating Dissolution of Solid Electrolyte Interphases in Sodium-Ion Batteries. Angew. Chemie Int. Ed. *60*, 4855–4863.

139. Wang, E., Niu, Y., Yin, Y.-X., and Guo, Y.-G. (2021). Manipulating Electrode/Electrolyte Interphases of Sodium-Ion Batteries: Strategies and Perspectives. ACS Mater. Lett. *3*, 18–41.

140. Mogensen, R., Brandell, D., and Younesi, R. (2016). Solubility of the Solid Electrolyte Interphase (SEI) in Sodium Ion Batteries. ACS Energy Lett. *1*, 1173–1178.

141. Wei, S., Choudhury, S., Xu, J., Nath, P., Tu, Z., and Archer, L.A. (2017). Highly Stable Sodium Batteries Enabled by Functional Ionic Polymer Membranes. Adv. Mater. *29*, 1605512.

142. Rodriguez, R., Loeffler, K.E., Nathan, S.S., Sheavly, J.K., Dolocan, A., Heller, A., and Mullins, C.B. (2017). In Situ Optical Imaging of Sodium Electrodeposition: Effects of Fluoroethylene Carbonate. ACS Energy Lett. *2*, 2051–2057.

143. Zhang, L., Tsolakidou, C., Mariyappan, S., Tarascon, J.M., and Trabesinger, S. (2021). Unraveling gas evolution in sodium batteries by online electrochemical mass spectrometry. Energy Storage Mater. *42*, 12–21.

144. Chen, X., Shen, X., Li, B., Peng, H., Cheng, X., Li, B., Zhang, X., Huang, J., and Zhang, Q. (2018). Ion–Solvent Complexes Promote Gas Evolution from Electrolytes on a Sodium Metal Anode. Angew. Chemie Int. Ed. *57*, 734–737.

145. Guo, R., Wang, D., Zuin, L., and Gallant, B.M. (2021). Reactivity and Evolution of Ionic Phases in the Lithium Solid–Electrolyte Interphase. ACS Energy Lett. *6*, 877–885.

146. Chen, H., Pei, A., Lin, D., Xie, J., Yang, A., Xu, J., Lin, K., Wang, J., Wang, H., Shi,

F., et al. (2019). Uniform High Ionic Conducting Lithium Sulfide Protection Layer for Stable Lithium Metal Anode. Adv. Energy Mater. *9*, 1900858.

147. Rehnlund, D., Ihrfors, C., Maibach, J., and Nyholm, L. (2018). Dendrite-free lithium electrode cycling via controlled nucleation in low LiPF6 concentration electrolytes. Mater. Today *21*, 1010–1018.

148. Jiao, S., Zheng, J., Li, Q., Li, X., Engelhard, M.H., Cao, R., Zhang, J.-G., and Xu, W. (2018). Behavior of Lithium Metal Anodes under Various Capacity Utilization and High Current Density in Lithium Metal Batteries. Joule *2*, 110–124.

149. Jurng, S., Brown, Z.L., Kim, J., and Lucht, B.L. (2018). Effect of electrolyte on the nanostructure of the solid electrolyte interphase (SEI) and performance of lithium metal anodes. Energy Environ. Sci. *11*, 2600–2608.

150. Li, Y., Li, Y., Pei, A., Yan, K., Sun, Y., Wu, C.-L., Joubert, L.-M., Chin, R., Koh, A.L., Yu, Y., et al. (2017). Atomic structure of sensitive battery materials and interfaces revealed by cryo–electron microscopy. Science. *358*, 506–510.

151. Wan, C., Xu, S., Hu, M.Y., Cao, R., Qian, J., Qin, Z., Liu, J., Mueller, K.T., Zhang, J.-G., and Hu, J.Z. (2017). Multinuclear NMR Study of the Solid Electrolyte Interface Formed in Lithium Metal Batteries. ACS Appl. Mater. Interfaces *9*, 14741–14748.

152. Jin, C., Suenaga, K., and Iijima, S. (2008). Plumbing carbon nanotubes. Nat. Nanotechnol. *3*, 17–21.

153. Shih, D.S., Robertson, I.M., and Birnbaum, H.K. (1988). Hydrogen embrittlement of α titanium: In situ tem studies. Acta Metall. *36*, 111–124.

154. Legros, M., Cabié, M., and Gianola, D.S. (2009). In situ deformation of thin films on substrates. Microsc. Res. Tech. *72*, 270–283.

155. Taheri, M.L., Lagrange, T., Reed, B.W., Armstrong, M.R., Campbell, G.H., DeHope, W.J., Kim, J.S., King, W.E., Masiel, D.J., and Browning, N.D. (2009). Laser-based in situ techniques: Novel methods for generating extreme conditions in TEM samples. Microsc. Res. Tech. *72*, 122–130.

156. Sharma, R. (2009). Kinetic measurements from in situ TEM observations. Microsc. Res. Tech. *72*, 144–152.

157. Jiang, Y., Chen, Z., Han, Y., Deb, P., Gao, H., Xie, S., Purohit, P., Tate, M.W., Park, J., Gruner, S.M., et al. (2018). Electron ptychography of 2D materials to deep sub-ångström resolution. Nature *559*, 343–349.

158. Gu, M., Li, Y., Li, X., Hu, S., Zhang, X., Xu, W., Thevuthasan, S., Baer, D.R., Zhang, J.-G., Liu, J., et al. (2012). In Situ TEM Study of Lithiation Behavior of Silicon Nanoparticles Attached to and Embedded in a Carbon Matrix. ACS Nano *6*, 8439–8447.

159. Gong, Y., Zhang, J., Jiang, L., Shi, J.-A., Zhang, Q., Yang, Z., Zou, D., Wang, J., Yu, X., Xiao, R., et al. (2017). In Situ Atomic-Scale Observation of Electrochemical Delithiation Induced Structure Evolution of LiCoO 2 Cathode in a Working All-Solid-State Battery. J. Am. Chem. Soc. *139*, 4274–4277.

160. Liu, X.H., Zheng, H., Zhong, -Li, Huang, S., Karki, K., Zhang, L.Q., Liu, Y., Kushima, A., Liang, W.T., Wang, J.W., et al. (2011). Anisotropic Swelling and Fracture of Silicon Nanowires during Lithiation. Nano Lett. *11*, 3312–3318.

161. Huang, J.Y., Zhong, L., Wang, C.M., Sullivan, J.P., Xu, W., Zhang, L.Q., Mao, S.X., Hudak, N.S., Liu, X.H., Subramanian, A., et al. (2010). In Situ Observation of the Electrochemical Lithiation of a Single SnO 2 Nanowire Electrode. Science. *330*, 1515–1520.

162. Liu, X.H., Zhang, L.Q., Zhong, L., Liu, Y., Zheng, H., Wang, J.W., Cho, J.-H., Dayeh, S.A., Picraux, S.T., Sullivan, J.P., et al. (2011). Ultrafast Electrochemical Lithiation of Individual Si Nanowire Anodes. Nano Lett. *11*, 2251–2258.

163. Williamson, M.J., Tromp, R.M., Vereecken, P.M., Hull, R., and Ross, F.M. (2003). Dynamic microscopy of nanoscale cluster growth at the solid–liquid interface. Nat. Mater. *2*, 532–536.

164. Jonge, N. de, Peckys, D.B., Kremers, G.J., and Piston, D.W. (2009). Electron microscopy of whole cells in liquid with nanometer resolution. Proc. Natl. Acad. Sci. *106*, 2159–2164.

165. Zheng, H., Smith, R.K., Jun, Y. -w., Kisielowski, C., Dahmen, U., and Alivisatos, A.P. (2009). Observation of Single Colloidal Platinum Nanocrystal Growth Trajectories. Science. *324*, 1309–1312.

166. Gu, M., Parent, L.R., Mehdi, B.L., Unocic, R.R., McDowell, M.T., Sacci, R.L., Xu, W., Connell, J.G., Xu, P., Abellan, P., et al. (2013). Demonstration of an Electrochemical Liquid Cell for Operando Transmission Electron Microscopy Observation of the Lithiation/Delithiation Behavior of Si Nanowire Battery Anodes. Nano Lett. *13*, 6106–6112.

167. Holtz, M.E., Yu, Y., Gunceler, D., Gao, J., Sundararaman, R., Schwarz, K.A., Arias,

T.A., Abruña, H.D., and Muller, D.A. (2014). Nanoscale Imaging of Lithium Ion Distribution During In Situ Operation of Battery Electrode and Electrolyte. Nano Lett. *14*, 1453–1459.

168. Yuk, J.M., Seo, H.K., Choi, J.W., and Lee, J.Y. (2014). Anisotropic Lithiation Onset in Silicon Nanoparticle Anode Revealed by in Situ Graphene Liquid Cell Electron Microscopy. ACS Nano *8*, 7478–7485.

169. Mehdi, B.L., Qian, J., Nasybulin, E., Park, C., Welch, D.A., Faller, R., Mehta, H., Henderson, W.A., Xu, W., Wang, C.M., et al. (2015). Observation and quantification of nanoscale processes in lithium batteries by operando electrochemical (S)TEM. Nano Lett. *15*, 2168–2173.

170. Zeng, Z., Liang, W.-I., Liao, H.-G., Xin, H.L., Chu, Y.-H., and Zheng, H. (2014). Visualization of Electrode–Electrolyte Interfaces in LiPF 6 /EC/DEC Electrolyte for Lithium Ion Batteries via in Situ TEM. Nano Lett. *14*, 1745–1750.

171. Sacci, R.L., Dudney, N.J., More, K.L., Parent, L.R., Arslan, I., Browning, N.D., and Unocic, R.R. (2014). Direct visualization of initial SEI morphology and growth kinetics during lithium deposition by in situ electrochemical transmission electron microscopy. Chem. Commun. *50*, 2104.

172. Unocic, R.R., Sun, X.-G., Sacci, R.L., Adamczyk, L.A., Alsem, D.H., Dai, S., Dudney, N.J., and More, K.L. (2014). Direct Visualization of Solid Electrolyte Interphase Formation in Lithium-Ion Batteries with In Situ Electrochemical Transmission Electron Microscopy. Microsc. Microanal. *20*, 1029–1037.

173. Sacci, R.L., Black, J.M., Balke, N., Dudney, N.J., More, K.L., and Unocic, R.R.

(2015). Nanoscale Imaging of Fundamental Li Battery Chemistry: Solid-Electrolyte Interphase Formation and Preferential Growth of Lithium Metal Nanoclusters. Nano Lett. *15*, 2011–2018.

174. Andersson, A.., and Thomas, J.. (2001). The source of first-cycle capacity loss in LiFePO4. J. Power Sources *97–98*, 498–502.

175. Srinivasan, V., and Newman, J. (2004). Discharge Model for the Lithium Iron-Phosphate Electrode. J. Electrochem. Soc. *151*, A1517.

176. Padhi, A.K., Nanjundaswamy, K.S., and Goodenough, J.B. (1997). Phospho-olivines as Positive-Electrode Materials for Rechargeable Lithium Batteries. J. Electrochem. Soc. *144*, 1188–1194.

177. Egerton, R.F., Li, P., and Malac, M. (2004). Radiation damage in the TEM and SEM. In Micron, pp. 399–409.

178. Abellan, P., Mehdi, B.L., Parent, L.R., Gu, M., Park, C., Xu, W., Zhang, Y., Arslan, I., Zhang, J., Wang, C., et al. (2014). Probing the Degradation Mechanisms in Electrolyte Solutions for Li-Ion Batteries by in Situ Transmission Electron Microscopy. Nano Lett. *14*, 1293–1299.

179. Ross, F.M. (2015). Opportunities and challenges in liquid cell electron microscopy. Science. *350*, aaa9886–aaa9886.

180. Yuan, Y., Wood, S.M., He, K., Yao, W., Tompsett, D., Lu, J., Nie, A., Islam, M.S., and Shahbazian-Yassar, R. (2016). Atomistic Insights into the Oriented Attachment of Tunnel-Based Oxide Nanostructures. ACS Nano *10*, 539–548.

181. Leenheer, A.J., Jungjohann, K.L., Zavadil, K.R., Sullivan, J.P., and Harris, C.T. (2015). Lithium Electrodeposition Dynamics in Aprotic Electrolyte Observed in Situ via Transmission Electron Microscopy. ACS Nano *9*, 4379–4389.

182. Grogan, J.M., Schneider, N.M., Ross, F.M., and Bau, H.H. (2014). Bubble and Pattern Formation in Liquid Induced by an Electron Beam. Nano Lett. *14*, 359–364.

183. Elgrishi, N., Rountree, K.J., McCarthy, B.D., Rountree, E.S., Eisenhart, T.T., and Dempsey, J.L. (2018). A Practical Beginner's Guide to Cyclic Voltammetry. J. Chem. Educ. *95*, 197–206.

184. Bredar, A.R.C., Chown, A.L., Burton, A.R., and Farnum, B.H. (2020). Electrochemical Impedance Spectroscopy of Metal Oxide Electrodes for Energy Applications. ACS Appl. Energy Mater. *3*, 66–98.

185. Zhou, W., Apkarian, R., Wang, Z.L., and Joy, D. (2006). Fundamentals of Scanning Electron Microscopy (SEM). In Scanning Microscopy for Nanotechnology (Springer New York), pp. 1–40.

186. Li, K., Aarholt, T., Liu, J., Hulme, H., Garner, A., Preuss, M., Lozano-Perez, S., and Grovenor, C. (2019). 3D-characterization of deuterium distributions in zirconium oxide scale using high-resolution SIMS. Appl. Surf. Sci. *464*, 311–320.

187. Harris, R.K., Becker, E.D., Cabral de Menezes, S.M., Goodfellow, R., and Granger, P. (2002). NMR Nomenclature: Nuclear Spin Properties and Conventions for Chemical Shifts. Solid State Nucl. Magn. Reson. *22*, 458–483.

188. Williams, D.B., and Carter, C.B. (2009). Transmission Electron Microscopy (Springer US).

189. Tang, C.Y., and Yang, Z. (2017). Transmission Electron Microscopy (TEM). In Membrane Characterization (Elsevier), pp. 145–159.

190. Wolf, S.G., and Elbaum, M. (2019). CryoSTEM tomography in biology. In Methods in Cell Biology (Elsevier Inc.), pp. 197–215.

191. Nellist, P.D., and Pennycook, S.J. (2000). The principles and interpretation of annular dark-field Z-contrast imaging. In Advances in Imaging and Electron Physics, pp. 147–203.

192. Unocic, R.R., Jungjohann, K.L., Mehdi, B.L., Browning, N.D., and Wang, C. (2020). In situ electrochemical scanning/transmission electron microscopy of electrode–electrolyte interfaces. MRS Bull. *45*, 738–745.

193. Pu, S.D., Gong, C., Gao, X., Ning, Z., Yang, S., Marie, J.-J., Liu, B., House, R.A., Hartley, G.O., Luo, J., et al. (2020). Current-Density-Dependent Electroplating in Ca Electrolytes: From Globules to Dendrites. ACS Energy Lett. *5*, 2283–2290.

194. Tikekar, M.D., Choudhury, S., Tu, Z., and Archer, L.A. (2016). Design principles for electrolytes and interfaces for stable lithium-metal batteries. Nat. Energy *1*, 16114.

195. Fan, X., Chen, L., Borodin, O., Ji, X., Chen, J., Hou, S., Deng, T., Zheng, J., Yang, C., Liou, S.-C., et al. (2018). Non-flammable electrolyte enables Li-metal batteries with aggressive cathode chemistries. Nat. Nanotechnol. *13*, 715–722.

196. Weber, R., Genovese, M., Louli, A.J., Hames, S., Martin, C., Hill, I.G., and Dahn, J.R. (2019). Long cycle life and dendrite-free lithium morphology in anode-free lithium pouch cells enabled by a dual-salt liquid electrolyte. Nat. Energy *4*, 683–689.

197. Fan, X., Chen, L., Ji, X., Deng, T., Hou, S., Chen, J., Zheng, J., Wang, F., Jiang, J., Xu, K., et al. (2018). Highly Fluorinated Interphases Enable High-Voltage Li-Metal Batteries. Chem *4*, 174–185.

198. Zheng, H., Xiang, H., Jiang, F., Liu, Y., Sun, Y., Liang, X., Feng, Y., and Yu, Y. (2020). Lithium Difluorophosphate-Based Dual-Salt Low Concentration Electrolytes for Lithium Metal Batteries. Adv. Energy Mater. *10*, 2001440.

199. Gao, Y., Rojas, T., Wang, K., Liu, S., Wang, D., Chen, T., Wang, H., Ngo, A.T., and Wang, D. (2020). Low-temperature and high-rate-charging lithium metal batteries enabled by an electrochemically active monolayer-regulated interface. Nat. Energy *5*, 534–542.

200. Luo, J., Fang, C.-C., and Wu, N.-L. (2018). High Polarity Poly(vinylidene difluoride) Thin Coating for Dendrite-Free and High-Performance Lithium Metal Anodes. Adv. Energy Mater. *8*, 1701482.

201. Sheng, O., Zheng, J., Ju, Z., Jin, C., Wang, Y., Chen, M., Nai, J., Liu, T., Zhang, W., Liu, Y., et al. (2020). In Situ Construction of a LiF-Enriched Interface for Stable All-Solid-State Batteries and its Origin Revealed by Cryo-TEM. Adv. Mater. *2000223*, 1–10.

202. Xu, Y., Wu, H., He, Y., Chen, Q., Zhang, J.G., Xu, W., and Wang, C. (2020). Atomic to Nanoscale Origin of Vinylene Carbonate Enhanced Cycling Stability of Lithium Metal Anode Revealed by Cryo-Transmission Electron Microscopy. Nano Lett. *20*, 418–425.

203. Wang, C., Meng, Y.S., and Xu, K. (2019). Perspective—Fluorinating Interphases. J.

Electrochem. Soc. *166*, A5184–A5186.

204. Hsieh, Y.-C., Leißing, M., Nowak, S., Hwang, B.-J., Winter, M., and Brunklaus, G. (2020). Quantification of Dead Lithium via In Situ Nuclear Magnetic Resonance Spectroscopy. Cell Reports Phys. Sci. *1*, 100139.

205. Xu, K. (2004). Nonaqueous liquid electrolytes for lithium-based rechargeable batteries. Chem. Rev. *104*, 4303–4417.

206. Egerton, R.F., Li, P., and Malac, M. (2004). Radiation damage in the TEM and SEM. Micron *35*, 399–409.

207. Pu, S., Gong, C., and Robertson, A.W. (2020). Liquid cell transmission electron microscopy and its applications. R. Soc. Open Sci. *7*, 191204.

208. Zou, P., Wang, Y., Chiang, S.W., Wang, X., Kang, F., and Yang, C. (2018). Directing lateral growth of lithium dendrites in micro-compartmented anode arrays for safe lithium metal batteries. Nat. Commun. *9*, 464.

209. Xu, K. (2014). Electrolytes and Interphases in Li-Ion Batteries and Beyond. Chem. Rev. *114*, 11503–11618.

210. Shkrob, I.A., Wishart, J.F., and Abraham, D.P. (2015). What Makes Fluoroethylene Carbonate Different? J. Phys. Chem. C *119*, 14954–14964.

211. Markevich, E., Salitra, G., and Aurbach, D. (2017). Fluoroethylene Carbonate as an Important Component for the Formation of an Effective Solid Electrolyte Interphase on Anodes and Cathodes for Advanced Li-Ion Batteries. ACS Energy Lett. *2*, 1337–1345.

212. Jin, Y., Kneusels, N.J.H., Marbella, L.E., Castillo-Martínez, E., Magusin, P.C.M.M., Weatherup, R.S., Jónsson, E., Liu, T., Paul, S., and Grey, C.P. (2018). Understanding Fluoroethylene Carbonate and Vinylene Carbonate Based Electrolytes for Si Anodes in Lithium Ion Batteries with NMR Spectroscopy. J. Am. Chem. Soc. *140*, 9854–9867.

213. Robertson, A.W., Zhu, G., Mehdi, B.L., Jacobs, R.M.J., De Yoreo, J., and Browning, N.D. (2018). Nanoparticle Immobilization for Controllable Experiments in Liquid-Cell Transmission Electron Microscopy. ACS Appl. Mater. Interfaces *10*, 22801–22808.

214. Hou, T., Yang, G., Rajput, N.N., Self, J., Park, S.W., Nanda, J., and Persson, K.A. (2019). The influence of FEC on the solvation structure and reduction reaction of LiPF6/EC electrolytes and its implication for solid electrolyte interphase formation. Nano Energy *64*, 103881.

215. Moore, K.L., Lombi, E., Zhao, F.J., and Grovenor, C.R.M. (2012). Elemental imaging at the nanoscale: NanoSIMS and complementary techniques for element localisation in plants. Anal. Bioanal. Chem. *402*, 3263–3273.

216. Shadike, Z., Lee, H., Borodin, O., Cao, X., Fan, X., Wang, X., Lin, R., Bak, S.-M., Ghose, S., Xu, K., et al. (2021). Identification of LiH and nanocrystalline LiF in the solid–electrolyte interphase of lithium metal anodes. Nat. Nanotechnol. *16*, 549–554.

217. Trease, N.M., Ko ster, T.K.-J., and Grey, C.P. (2011). In Situ NMR Studies of Lithium Ion Batteries. Interface Mag. *20*, 69–73.

218. Guéguen, A., Streich, D., He, M., Mendez, M., Chesneau, F.F., Novák, P., and Berg,

E.J. (2016). Decomposition of LiPF 6 in High Energy Lithium-Ion Batteries Studied with Online Electrochemical Mass Spectrometry. J. Electrochem. Soc. *163*, A1095–A1100.

219. Ray, A., Bristow, T., Whitmore, C., and Mosely, J. (2018). On-line reaction monitoring by mass spectrometry, modern approaches for the analysis of chemical reactions. Mass Spectrom. Rev. *37*, 565–579.

220. Zhang, Q., Pan, J., Lu, P., Liu, Z., Verbrugge, M.W., Sheldon, B.W., Cheng, Y.T., Qi, Y., and Xiao, X. (2016). Synergetic Effects of Inorganic Components in Solid Electrolyte Interphase on High Cycle Efficiency of Lithium Ion Batteries. Nano Lett. *16*, 2011–2016.

221. Gong, C., Pu, S.D., Gao, X., Yang, S., Liu, J., Ning, Z., Rees, G.J., Capone, I., Pi, L., Liu, B., et al. (2021). Revealing the Role of Fluoride-Rich Battery Electrode Interphases by Operando Transmission Electron Microscopy. Adv. Energy Mater. *11*, 2003118.

222. Eshetu, G.G., Diemant, T., Hekmatfar, M., Grugeon, S., Behm, R.J., Laruelle, S., Armand, M., and Passerini, S. (2019). Impact of the electrolyte salt anion on the solid electrolyte interphase formation in sodium ion batteries. Nano Energy *55*, 327–340.

223. Gu, Y., Wang, W.-W., Li, Y.-J., Wu, Q.-H., Tang, S., Yan, J.-W., Zheng, M.-S., Wu, D.-Y., Fan, C.-H., Hu, W.-Q., et al. (2018). Designable ultra-smooth ultra-thin solid-electrolyte interphases of three alkali metal anodes. Nat. Commun. *9*, 1339.

224. Hu, J., Wang, H., Wang, S., Lei, Y., Qin, L., Li, X., Zhai, D., Li, B., and Kang, F. (2021). Electrochemical deposition mechanism of sodium and potassium. Energy

Storage Mater. *36*, 91–98.

225. Liu, Q., Zhang, L., Sun, H., Geng, L., Li, Y., Tang, Y., Jia, P., Wang, Z., Dai, Q., Shen, T., et al. (2020). In Situ Observation of Sodium Dendrite Growth and Concurrent Mechanical Property Measurements Using an Environmental Transmission Electron Microscopy–Atomic Force Microscopy (ETEM-AFM) Platform. ACS Energy Lett. *5*, 2546–2559.

226. Huang, J., Guo, X., Du, X., Lin, X., Huang, J.-Q., Tan, H., Zhu, Y., and Zhang, B. (2019). Nanostructures of solid electrolyte interphases and their consequences for microsized Sn anodes in sodium ion batteries. Energy Environ. Sci. *12*, 1550–1557.

227. Wu, Y., and Liu, N. (2018). Visualizing Battery Reactions and Processes by Using In Situ and In Operando Microscopies. Chem *4*, 438–465.

228. Liu, D., Shadike, Z., Lin, R., Qian, K., Li, H., Li, K., Wang, S., Yu, Q., Liu, M., Ganapathy, S., et al. (2019). Review of Recent Development of In Situ/Operando Characterization Techniques for Lithium Battery Research. Adv. Mater. *31*, 1806620.

229. Yuan, Y., Amine, K., Lu, J., and Shahbazian-Yassar, R. (2017). Understanding materials challenges for rechargeable ion batteries with in situ transmission electron microscopy. Nat. Commun. *8*, 15806.

230. Tian, Y., Sun, Y., Hannah, D.C., Xiao, Y., Liu, H., Chapman, K.W., Bo, S.-H., and Ceder, G. (2019). Reactivity-Guided Interface Design in Na Metal Solid-State Batteries. Joule *3*, 1037–1050.

231. Hirsh, H.S., Sayahpour, B., Shen, A., Li, W., Lu, B., Zhao, E., Zhang, M., and Meng, Y.S. (2021). Role of electrolyte in stabilizing hard carbon as an anode for

rechargeable sodium-ion batteries with long cycle life. Energy Storage Mater. *42*, 78–87.

232. Gong, C., Pu, S.D., Zhang, S., Yuan, Y., Ning, Z., Yang, S., Gao, X., Chau, C., Li, Z., Liu, J., et al. (2023). The role of an elastic interphase in suppressing gas evolution and promoting uniform electroplating in sodium metal anodes. Energy Environ. Sci. *16*, 535–545.

233. Gao, Y., Du, X., Hou, Z., Shen, X., Mai, Y.-W., Tarascon, J.-M., and Zhang, B. (2021). Unraveling the mechanical origin of stable solid electrolyte interphase. Joule *5*, 1860–1872.

234. Li, Z., Huang, J., Yann Liaw, B., Metzler, V., and Zhang, J. (2014). A review of lithium deposition in lithium-ion and lithium metal secondary batteries. J. Power Sources *254*, 168–182.

235. Shin, J.-S., Han, C.-H., Jung, U.-H., Lee, S.-I., Kim, H.-J., and Kim, K. (2002). Effect of Li2CO3 additive on gas generation in lithium-ion batteries. J. Power Sources *109*, 47–52.

236. Lee, Y., Lee, J., Lee, J., Kim, K., Cha, A., Kang, S., Wi, T., Kang, S.J., Lee, H.-W., and Choi, N.-S. (2018). Fluoroethylene Carbonate-Based Electrolyte with 1 M Sodium Bis(fluorosulfonyl)imide Enables High-Performance Sodium Metal Electrodes. ACS Appl. Mater. Interfaces *10*, 15270–15280.

237. He, Y., Bai, P., Gao, S., and Xu, Y. (2018). Marriage of an Ether-Based Electrolyte with Hard Carbon Anodes Creates Superior Sodium-Ion Batteries with High Mass Loading. ACS Appl. Mater. Interfaces *10*, 41380–41388.

238. Zhu, Y.-E., Yang, L., Zhou, X., Li, F., Wei, J., and Zhou, Z. (2017). Boosting the rate capability of hard carbon with an ether-based electrolyte for sodium ion batteries. J. Mater. Chem. A *5*, 9528–9532.